

CERN-LHCC-2006-014  
CERN/LHCC 96-32-Add3  
14 April 2006

# ALICE

## **The Electromagnetic Calorimeter**

### **Addendum to the Technical Proposal**

Cover design by CERN Desktop Publishing Service.  
Cover: Closeup photograph of fiber bundles out of two EMCal towers.

Printed at CERN  
April 2006.

ISBN 92-9083-270-3  
ISBN 978-92-9083-270-6

# ALICE Collaboration

---

**Alessandria, Italy**, Facoltà di Scienze dell'Università and INFN:  
P. Cortese, G. Dellacasa, L. Ravayamello and M. Sitta.

**Aligarh, India**, Physics Department, Aligarh Muslim University:  
N. Ahmad, S. Ahmad, T. Ahmad, W. Bari, M. Irfan and M. Zafar.

**Amsterdam, The Netherlands**, National Institute for Nuclear and High Energy Physics (NIKHEF):  
M. Botje, P.G. Kuijer and R. Snellings.

**Athens, Greece**, University of Athens, Physics Department:  
A. Belogianni, P. Christakoglou<sup>1)</sup>, M. Fragkiadakis, P. Ganoti, A. Petridis, F. Roukoutakis<sup>1)</sup>,  
M. Spyropoulou-Stassinaki, C. Tagridis and M. Vassiliou.

**Austin, USA**, University of Texas<sup>†)</sup>:  
G.W. Hoffmann, C. Markert<sup>31)</sup>, R.L. Ray and J.J. Schambach.

**Bari, Italy**, Dipartimento di Fisica dell'Università and Sezione INFN:  
G.E. Bruno, M. Caselle, G. D'Erasmo, D. Di Bari, D. Elia, R.A. Fini, A. Gallas Torreira, B. Ghidini,  
E. Fiore, V. Lenti, V. Manzari, A. Mastroserio, F. Minafra, E. Nappi, F. Navach, A. Pantaleo, C. Pastore,  
V. Paticchio, D. Perrino, F. Posa, R. Santoro, I. Sgura and G. Volpe.

**Bari, Italy**, Politecnico and Sezione INFN:  
F. Corsi, D. De Venuto, U. Fratino, C. Marzocca and A. Tauro.

**Beijing, China**, China Institute of Atomic Energy:  
X. Li, S. Lu, Z. Lu, B. Sa, J. Yuan, J. Zhou and S. Zhou.

**Bergen, Norway**, Department of Physics and Technology, University of Bergen:  
J. Alme, S. Bablok, A. Klovning, J. Nystrand, B. Pommeresche, M. Richter, D. Röhrich, K. Ullaland  
and H. Yang<sup>2)</sup>.

**Bergen, Norway**, Bergen University College, Faculty of Engineering:  
H. Helstrup, K.F. Hetland, B. Kileng and K. Røed.

**Berkeley, USA**, Nuclear Science Division, Lawrence Berkeley National Laboratory<sup>†)</sup>:  
S.-L. Blyth, H. Gray, M.J. Horner, P. Jacobs, S. Klein, G. Odyniec, J. Putschke, J. Rasson, H.G. Ritter,  
I. Sakrejda, T.J.M. Symons and M. Van Leeuwen.

**Bhubaneswar, India**, Institute of Physics:  
A.K. Dash, S. Dash, D.P. Mahapatra, S.C. Phatak, R. Sahoo and P.K. Sahu.

**Birmingham, United Kingdom**, School of Physics and Space Research, University of Birmingham:  
L. Daniel, D. Evans, G.T. Jones, P. Jovanović, A. Jusko, J.B. Kinson, R. Platt, R. Lietava,  
J.D. Tapia Takaki and O. Villalobos Baillie.

**Bologna, Italy**, Dipartimento di Fisica dell'Università and Sezione INFN:

A. Alici, S. Antinori, P. Antonioli, S. Arcelli, G. Bari, M. Basile, G. Cara Romeo, L. Cifarelli, F. Cindolo, D. Falchieri, A. Gabrielli, E. Gandolfi, D. Hatzifotiadou, G. Laurenti, M.L. Luvisetto, A. Margotti, M. Masetti, R. Nania, F. Noferini, F. Palmonari, A. Pesci, R. Preghenella, G. Sartorelli, E. Scapparone, G. Scioli, G.P. Vacca, G. Venturi, M.C.S. Williams, C. Zampolli and A. Zichichi.

**Bratislava, Slovakia**, Comenius University, Faculty of Mathematics, Physics and Informatics:

V. Cerny, R. Janik, M. Pikna, P. Rosinsky, B. Sitar, P. Strmen and I. Szarka.

**Bucharest, Romania**, National Institute for Physics and Nuclear Engineering:

C. Aiftimieci, V. Catanescu, C.I. Legrand, M. Petrovici, A. Pop, C. Schiaua and V. Simion.

**Budapest, Hungary**, KFKI Research Institute for Particle and Nuclear Physics, Hungarian Academy of Sciences:

G. Barnaföldi, L. Boldizsár, E. Dénes, Z. Fodor, E. Futó, T. Kiss, P. Lévai, G. Pála and T. Tolyhi.

**Cagliari, Italy**, Dipartimento di Fisica dell'Università and Sezione INFN:

I. Atanassov, C. Cicalo, A. De Falco, M. Floris, A. Masoni, D. Mura, G. Puddu, J. Samarati, S. Serici, E. Siddi, G. Usai and H. Woehri.

**Cape Town, South Africa**, University of Cape Town:

J. Cleymans, G. de Vaux, R.W. Fearick, A. Szostak and Z.Z. Vilakazi.

**Catania, Italy**, Dipartimento di Fisica dell'Università and Sezione INFN:

A. Badalà, R. Barbera, F. Blanco, F. Fichera, F. Librizzi, G. Lo Re, D. Nicotra, A. Palmeri, G.S. Pappalardo, A. Pulvirenti, R. Rapicavoli, F. Riggi, G. Sacca and S. Urso.

**CERN, Switzerland**, European Organization for Nuclear Research:

G. Aglieri Rinella, G. Anelli, I. Augustin<sup>4)</sup>, A. Augustinus, J. Baechler, P.L. Barberis<sup>30)</sup>, J.A. Belikov<sup>5)</sup>, L. Betev, A. Boccardi, R. Brun, M. Burns, P. Buncic<sup>6)</sup>, I. Cali, R. Campagnolo, M. Campbell, F. Carena, W. Carena, F. Carminati, G. De Cataldo<sup>30)</sup>, S. Ceresa, S. Chapeland, C. Cheshkov, P. Chochula, P. Christiansen, A. Colla<sup>7)</sup>, J. Conrad, B.F. Correia Belbute, M. Davenport, J. de Groot, A. Di Mauro, R. Divià, C. Engster, S. Evrard, C.W. Fabjan, L. Feng, D. Flierl, F. Formenti, U. Fuchs, A. García López, A. Gheata, M. Gheata<sup>8)</sup>, C. González-Gutiérrez, R. Grosso<sup>7)</sup>, C. Grigoras, J.F. Grosse-Oetringhaus<sup>32)</sup>, R. Grosso<sup>7)</sup>, M. Gruwe, H.-A. Gustafsson<sup>9)</sup>, H. Hoedelmoser, P. Hristov, M. Ivanov, L. Jirden, C. Jorgensen, A. Junique, S. Kapusta<sup>10)</sup>, W. Kicking, W. Klempt, A. Kluge, F. Lackner, L. Leistam, J.P. Lo, M. López Noriega, C. Lourenço, I. Makhlyueva, J.C. Marin, P. Martinengo, D. Meunier-Picard, M. Meoni<sup>11)</sup>, M. Morel, A. Morsch, H. Muller, L. Musa, T.K. Nayak<sup>12)</sup>, P. Nilsson, F. Osmic, B. Pastirčák<sup>10)</sup>, D. Perini, V. Peskov, R. Pestotnik, A. Peters<sup>6)</sup>, V. Pinto Morais, S. Popescu, F. Rademakers, J.-P. Revol, P. Riedler, W. Riegler, P. Rosinsky, H. Rovik, K. Šafařík, T. Schioler, K. Schossmaier, J. Schukraft, Y. Schutz<sup>14)</sup>, P.A. Silva Loureiro, C. Soos<sup>15)</sup>, G. Stefanini, D. Swoboda, M. Tadel, H. Taureg, M. Tavlet, P. Tissot-Daguette, C. Torcato de Matos, H. Tydesjo, P. Vande Vyvre and J.-P. Vanuxem.

**Chandigarh, India**, Physics Department, Panjab University:

M.M. Aggarwal, A.K. Bhati, N. Kumar and L. Kumar.

**Clermont-Ferrand, France**, Laboratoire de Physique Corpusculaire (LPC), IN2P3-CNRS and Université Blaise Pascal:

A. Baldit, V. Barret, N. Bastid, G. Blanchard, J. Castor, P. Crochet, F. Daudon, A. Devaux, P. Dupieux, P. Force, S. Grigoryan<sup>16)</sup>, F. Guerin, R. Guernane, C. Insa, F. Jouve, J. Lecoq, F. Manso, P. Rosnet, L. Royer, P. Saturnini and G. Savinel.



**Columbus, USA**, Department of Physics, Ohio State University:  
T.J. Humanic, I.V. Kotov, M.A. Lisa, B.S. Nilsen and D. Truesdale.

**Columbus, USA**, Ohio Supercomputer Center:  
D. Johnson.

**Copenhagen, Denmark**, Niels Bohr Institute:  
I. Bearden, H. Bøggild, C.H. Christensen, J.J. Gaardhøje, K. Gulbrandsen, B.S. Nielsen and G. Renault.

**Cracow, Poland**, Henryk Niewodniczanski Institute of Nuclear Physics, High Energy Physics  
Department:  
J. Bartke, E. Gładysz-Dziaduś, E. Kornaś, M. Kowalski, A. Rybicki and A. Wróblewski<sup>17)</sup>.

**Darmstadt, Germany**, Gesellschaft für Schwerionenforschung (GSI):  
S. Altinpinar, A. Andronic, D. Antonczyk, R. Bailhache, A. Bercuci, E. Berdermann,  
P. Braun-Munzinger, O. Busch, M. Ciobanu<sup>18)</sup>, P. Foka, U. Frankenfeld, C. Garabatos, H. Gutbrod,  
C. Lippmann, P. Malzacher, A. Marín, S. Masciocchi, D. Miśkowiec, S. Radomski, C.J. Schmidt,  
H.R. Schmidt, K. Schwarz, R.S. Simon, D. Soyk, H. Stelzer, M. Stockmeier, G. Tziledakis, D. Vranic  
and J. Wiechula.

**Darmstadt, Germany**, Institut für Kernphysik, Technische Universität:  
U. Bonnes, I. Kraus and H. Oeschler.

**Davis, USA**, Department of Physics, University of California<sup>†)</sup>:  
D. Ferenc and E. Lorenz.

**Detroit, USA**, Department of Physics, Wayne State University<sup>†)</sup>:  
R. Bellwied, T.M. Cormier, M. Elnimr, A.I. Pavlinov, V.A. Petrov, C. Pruneau, J. Riso and  
S.A. Voloshin.

**East Lansing, USA**, National Superconducting Cyclotron Laboratory, Michigan State University<sup>†)</sup>:  
G.D. Westfall.

**Frankfurt, Germany**, Institut für Kernphysik, Johann Wolfgang Goethe Universität:  
H. Appelshäuser, C. Blume, T. Dietel, M. Gaździcki, M. Hartig, M. Kliemant, S. Kniese, T. Kollegger,  
F. Kramer, S. Lange, C. Loizides, M. Ploskon, R. Renfordt, W. Sommer, R. Stock and H. Ströbele.

**Frascati, Italy**, INFN Laboratori Nazionali di Frascati:  
N. Bianchi, G.P. Capitani, G. Conesa Balbastre, E. De Sanctis, P. Di Nezza, A. Fantoni, C. Hadjidakis,  
D. Hasch, V. Muccifora and F. Ronchetti.

**Gatchina, Russia**, St. Petersburg Nuclear Physics Institute:  
Ya. Berdnikov, V. Ivanov, A. Khanzadeev, N. Miftakhov, V. Nikulin, V. Polyakov, E. Rostchin,  
V. Samsonov, O. Tarasenkova, V. Tarakanov and M. Zhalov.

**Grenoble, France**, Laboratory for Subatomic Physics and Cosmology (LSPC)<sup>\*)</sup>:  
O. Bourrion, C. Furget, D. Grondin, S. Kox and J.-F. Muraz.

**Havana, Cuba**, Centro de Aplicaciones Tecnológicas y Desarrollo Nuclear (CEADEN):  
E. López Torres, A. Abrahantes Quintana and R. Díaz Valdes.

**Heidelberg, Germany**, Kirchhoff Institute for Physics:

T. Alt, V. Angelov, J. Cuveland, S. Kalcher, U. Kebschull, V. Lindenstruth, R. Panse, C. Reichling, R. Schneider, T. Steinbeck, J. Thäder and G. Tröger.

**Heidelberg, Germany**, Physikalisches Institut, Ruprecht-Karls Universität:

C. Adler, M. de Gaspari, D. Emschermann, P. Glässel, N. Herrmann, W. Ludolphs, J. Mercado, J. Milosevic, R. Monroy-Gamboa, K. Oyama, I. Rusanov, R. Schicker, K. Schweda, P. Shukla, H.K. Soltveit, R. Soualah, J. Stachel, G. Tsiledakis, B. Vulpescu, B. Windelband and S. Yurevich.

**Hiroshima, Japan**, Hiroshima University<sup>\*)</sup>:

K. Shigaki and T. Sugitate.

**Houston, USA**, Department of Physics, University of Houston<sup>†)</sup>:

A. Empl, B. Mayes and L. Pinsky.

**Jaipur, India**, Physics Department, University of Rajasthan:

R. Raniwala and S. Raniwala.

**Jammu, India**, Physics Department, Jammu University:

S.K. Badyal, R. Bala, A. Bhasin, A. Gupta, V.K. Gupta, S. Mahajan, L.K. Mangotra, B.V.K.S. Potukuchi and S.S. Sambyal.

**JINR, Russia**, Joint Institute for Nuclear Research:

P.G. Akichine, V.A. Arefiev, Ts. Baatar<sup>19)</sup>, B.V. Batiounia, V.F. Chepurinov, S.A. Chernenko, V.K. Dodokhov, O.V. Fateev, A.G. Fedunov, V.G. Kadychevsky, G. Kharadze<sup>21)</sup>, B. Khurelbaatar<sup>19)</sup>, E.K. Koshurnikov, V.L. Lioubochits, V.I. Lobanov, L.V. Malinina, Y.I. Minaev, M. Nioradze<sup>22)</sup>, P.V. Nomokonov, Y.A. Panebrattsev, V.N. Penev, V.G. Pismennaya, T.A. Pocheptsov, G.S. Shabratova, A.I. Shklovskaya, M.K. Suleimanov, Y. Tevzadze<sup>22)</sup>, R. Togoo<sup>19)</sup>, A.S. Vodopianov, V.I. Yurevich, Y.V. Zanevsky, S.A. Zaporojets and A.I. Zinchenko.

**Jyväskylä, Finland**, Department of Physics, University of Jyväskylä and Helsinki Institute of Physics:

J. Äystö, M. Bondila, V. Lyapin, M. Oinonen, T. Malkiewicz, V. Ruuskanen, H. Seppänen, W. Trzaska, J. Rak and S. Yamaletdinov.

**Kangnung, Republic of Korea**, Kangnung National University:

H.T. Jung, W. Jung, D.-W. Kim, H.N. Kim, J.S. Kim, K.S. Lee and S.-C. Lee.

**Karlsruhe, Germany**, Institut für Prozessdatenverarbeitung und Elektronik (IPE)<sup>\*)</sup>:

T. Blank and H. Gemmeke.

**Kent, USA**, Department of Physics, Kent State University<sup>†)</sup>:

D. Keane, S. Margetis and W. Zang.

**Kharkov, Ukraine**, National Scientific Centre, Kharkov Institute of Physics and Technology:

G.L. Bochek, A.N. Dovbnia, V.I. Kulibaba, N.I. Maslov, S.V. Naumov, V.D. Ovchinnik, S.M. Potin and A.F. Starodubtsev.

**Kharkov, Ukraine**, Scientific and Technological Research Institute of Instrument Engineering:

V.N. Borshchov, O. Chykalov, S.K. Kiprich, L. Klymova, O.M. Listratenko, N. Mykhaylova, M. Protsenko, O. Reznik and I.Tymchuk.

**Kiev, Ukraine**, Department of High Energy Density Physics, Bogolyubov Institute for Theoretical Physics, National Academy of Sciences of Ukraine:  
O. Borysov, Y. Martynov, S. Molodtsov, S. Svistunov, S. Senyukov, Y. Sinyukov, G. Zinovjev and M. Zynovyev.

**Knoxville, USA**, Department of Physics, University of Tennessee<sup>†</sup>):  
Y. Kwon, K.F. Read and S. Sorensen.

**Kolkata, India**, Saha Institute of Nuclear Physics:  
S. Bose, S. Chatterjee, S. Chattopadhyay, D. Das, I. Das, A.K. Dutt-Mazumder, S. Pal, L. Paul, P. Roy, A. Sanyal, S. Sarkar, S.K. Sen, B.C. Sinha and T. Sinha.

**Kolkata, India**, Variable Energy Cyclotron Centre:  
Z. Ahammed, P. Bhaskar, S. Chattopadhyay, D. Das, M.R. Dutta Majumdar, M.S. Ganti, P. Ghosh, B. Mohanty, M.M. Mondal, P.K. Netrakanti, S. Pal, S.K. Prasad, J. Saini, R.N. Singaraju, V. Singhal, B. Sinha and Y.P. Viyogi.

**Köln, Germany**, University of Applied Sciences Cologne, Communications Engineering<sup>\*</sup>):  
G. Hartung and T. Krawutschke.

**Košice, Slovakia**, Institute of Experimental Physics, Slovak Academy of Sciences and Faculty of Science, P.J. Šafárik University:  
J. Bán, M. Bombara, A. Dirner, M. Hnatič, I. Králik, A. Kravčáková, F. Kriváň, M. Krivda, G. Martinská, B. Pastirčák, L. Šándor, J. Urbán and J. Vrláková.

**Legnaro, Italy**, Laboratori Nazionali di Legnaro:  
M. Cinausero, A. Dainese, E. Fioretto, G. Prete, R.A. Ricci and L. Vannucci.

**Livermore, USA**, Physics Division, Lawrence Livermore National Laboratory<sup>†</sup>):  
A. Enokizono, M. Heffner, J. Klay, J. Newby and R.A. Soltz.

**Los Angeles, USA**, Department of Physics, University of California<sup>†</sup>):  
V. Ghazikhanian, H.Z. Huang, S. Trentalange and C. Whitten Jr.

**Lund, Sweden**, Division of Experimental High Energy Physics, University of Lund:  
A. Oskarsson, L. Osterman, I. Otterlund and E.A. Stenlund.

**Lyon, France**, Institut de Physique Nucléaire de Lyon (IPNL), IN2P3-CNRS and Université Claude Bernard Lyon-I:  
B. Cheynis, L. Ducroux, J.Y. Grossiord, A. Guichard, P. Pillot, B. Rapp and R. Tieulent.

**Mexico City and Mérida, Mexico**, Centro de Investigación y de Estudios Avanzados del IPN, Universidad Nacional Autónoma de México, Instituto de Ciencias Nucleares, Instituto de Física:  
J.R. Alfaro Molina, A. Anzo, A. Ayala, E. Belmont Moreno, E. Castaneda, J.G. Contreras, E. Cuautle, J.C. D'Olivo, I. Domínguez, L. Gonzalez, V. Grabski, G. Herrera Corral, H. Leon, M.I. Martínez, A. Martínez Dávalos, A. Menchaca-Rocha, L.M. Montaña Zetina, L. Nellen, G. Paić<sup>24</sup>), C. Perez, P. Podesta, A. Sandoval and A. Zepeda.

**Moscow, Russia**, Institute for Nuclear Research, Academy of Science:  
V.A. Feshchenko, M.B. Golubeva, V.G. Gorlychev, F.F. Guber, O.V. Karavichev, T.L. Karavicheva, E.V. Karpechev, A.B. Kurepin, A.I. Maevskaya, V.V. Marin, I.A. Pshenichnov, V.I. Razin, A.I. Reshetin, K.A. Shileev and N.S. Topil'skaia.

**Moscow, Russia**, Institute for Theoretical and Experimental Physics:

A.N. Akindinov, A.B. Kaidalov, S.M. Kiselev, E. Lyublev, D.B. Mal'kevich, M. Martemianov, A.N. Martemianov, A.A. Nedosekin, A.V. Smirnitsky, M.M. Tchoumakov, I.A. Vetlitsky, K.G. Voloshin and B.V. Zagreev.

**Moscow, Russia**, Russian Research Center Kurchatov Institute:

D. Aleksandrov, V. Antonenko, S. Beliaev, S. Fokine, M. Ippolitov, K. Karadjev, A. Kazantsev, I. Koutcheriaev, V. Lebedev, V.I. Manko, T. Moukhanova, A. Nianine, S. Nikolaev, S. Nikouline, O. Patarakine, D. Peressounko, I. Sibiriak, A. Vasiliev, A. Vinogradov and I. Yushmanov.

**Moscow, Russia**, Moscow Engineering Physics Institute:

V.A. Grigoriev, V.A. Kaplin, N. Kondratieva, A. Kurepin and V.A. Loginov.

**Mumbai, India**, Indian Institute of Technology<sup>\*)</sup>:

B.K. Nandi and R. Varma.

**Mumbai, India**, Bhabha Atomic Research Centre (BARC)<sup>\*)</sup>:

V.B. Chandratre and S.K. Kataria.

**Münster, Germany**, Institut für Kernphysik Westfälische Wilhelms-Universität:

C. Baumann, R. Glasow, H. Gottschlag, N. Heine, C. Klein-Bösing, K. Reygers, R. Santo, W. Verhoeven, J. Wessels and A. Wilk.

**Nantes, France**, Laboratoire de Physique Subatomique et des Technologies Associées (SUBATECH), École des Mines de Nantes, IN2P3-CNRS and Université de Nantes:

L. Aphecetche, R. Berny, G. Bourdaud, S. Bouvier, Z. Conesa-del-Valle, J.P. Cussonneau, H. Delagrangé, M. Dialinas, Ch. Finck, B. Erazmus, S. Gadrat, M. Germain, F. Lefèvre, L. Luquin, G. Martínez, Ch. Renard, C. Roy and A. Tournaire.

**New Haven, USA**, Yale University:

S. Baumgart, J. Bielcik, J. Bielcikova, H. Caines, A. Knospe, J.W. Harris, M. Heinz, M.A.C. Lamont, S. Salur, N. Smirnov, J. Spitzxi and R. Witt.

**Novosibirsk, Russia**, Budker Institute for Nuclear Physics:

A.R. Frolov and I.N. Pestov.

**Oak Ridge, USA**, Physics Division, Oak Ridge National Laboratory<sup>†)</sup>:

T.C. Awes, V. Cianciolo, Y.V. Efremenko, D. Silvermyr, P.W. Stankus and G.R. Young.

**Omaha, USA**, Creighton University:

M. Cherney, Y. Gorbunov and J. Seger.

**Orsay, France**, Institut de Physique Nucléaire (IPNO), IN2P3-CNRS and Université de Paris-Sud:

L. Bimbot, V. Chambert, A. Charpy, M.P. Comets, P. Courtat, S. Drouet, P. Edelbruck, B. Espagnon, I. Hřivnáčová, Y. Le Bornec, J. Peyré, J. Pouthas, S. Rousseau, C. Suire and N. Willis.

**Oslo, Norway**, Department of Physics, University of Oslo:

L. Bravina, G. Løvholden, A. Nyiri, B. Skaali and T.S. Tvetter.

**Padua, Italy**, Dipartimento di Fisica dell'Università and Sezione INFN:

F. Antinori, C. Bombonati, R. Dima, D. Fabris, J. Faivre, M. Lunardon, M. Morando, S. Moretto, A. Pepato, E. Quercigh, F. Scarlassara, G. Segato, R. Turrisi and G. Viesti.

**Pohang, Republic of Korea**, Pohang University of Science and Technology, Department of Physics and Pohang Accelerator Laboratory:

J. Choi.

**Prague, Czech Republic**, Institute of Physics, Academy of Science:

A. Beitlerova, J. Mareš, K. Polák and P. Závada.

**Prague, Czech Republic**, Czech Technical University, Faculty of Nuclear Sciences and Physical Engineering:

V. Petráček, M. Pachr and L. Škoda.

**Protvino, Russia**, Institute for High Energy Physics:

M.Yu. Bogolyubsky, G.V. Khaustov, Yu.V. Kharlov, N.G. Minaev, V.A. Onuchin, V.S. Petrov, B.V. Polichtchouk, S.A. Sadovsky, V.A. Senko, A.S. Soloviev, P.V. Stolpovsky and V.A. Victorov.

**Puebla, Mexico**, Benemérita Universidad Autónoma de Puebla:

A. Fernández Téllez, E. Gamez Flores, I. León -Monzon, R. López-Ramírez, A. Ortiz-Velázquez, C. Pagliarone<sup>25)</sup>, S. Román-López, G. Tejada-Muñoz, A. Vargas, S. Vergara and L. Villaseñor Cendejas.

**Řež u Prahy, Czech Republic**, Academy of Sciences of Czech Republic, Nuclear Physics Institute:

D. Adamová, S. Kushpil, V. Kushpil, A. Kugler, M. Šumbera and V. Wagner.

**Rome, Italy**, Dipartimento di Fisica dell'Università 'La Sapienza' and Sezione INFN:

S. Di Liberto, M.A. Mazzoni, F. Meddi and G.M. Urciuoli.

**Saclay, France**, Centre d'Études Nucléaires, DAPNIA:

A. Baldisseri, H. Borel, J. Castillo, J.-L. Charvet, J. Gosset, F. Orsini, H. Pereira and F.M. Staley.

**Salerno, Italy**, Dipartimento di Fisica 'E.R.Caianiello' dell'Università and Sezione INFN:

A. De Caro, D. De Gruttola, S. De Pasquale, A. Di Bartolomeo, M. Fusco Girard, G. Grella, C. Guarnaccia, M. Guida, S. Sellitto, R. Silvestri and T. Virgili.

**Sarov, Russia**, Russian Federal Nuclear Center (VNIIEF):

V. Basmanov, D. Budnikov, V. Demanov, V. Ianowski, R. Ilkaev, L. Ilkaeva, A. Khlebnikov, A. Kouryakin, E. Mikhailov, S. Nazarenko, V. Pavlov, S. Philchagin, A. Punin, V. Punin, S. Poutevskoi, A. Rybin, I. Selin, M. Smetanin, A. Telnov, S. Treskov, O. Vikhlyantsev, I. Vinogradov, A. Vyushin, N. Zavyalov, S. Zhelezov and A. Zhitnik.

**Seattle, USA**, Department of Physics, University of Washington<sup>†)</sup>:

H. Bichsel, J.G. Cramer and D. Prindle.

**Split, Croatia**, Technical University of Split, Faculty of Electrical Engineering, Mechanical Engineering and Naval Architecture (FESB):

S. Gotovac, E. Mudnic and L. Vidak.

**St. Petersburg, Russia**, V. Fock Institute for Physics of St. Petersburg State University :

A.G. Asryan, M.A. Braun, D.A. Derkach, G.A. Feofilov, S.N. Igolkin, A.S. Ivanov, R.S. Kolevatov, A.A. Kolojvari, V.P. Kondratiev, P.A. Naumenko, T.A. Toulina, F.F. Valiev, V.V. Vechernin, L.I. Vinogradov and A.K. Zarochentsev.

**Seoul, Republic of Korea**, Sejong University Department of Physics:

C.Y. Choi, D.S. Hwang, H.G. Kim and S. Kim.

**Strasbourg, France**, Institut de Recherches Subatomiques (IReS), IN2P3-CNRS and Université Louis Pasteur:

D. Bonnet, J.P. Coffin, M. Estienne, B. Hippolyte, C. Kuhn, J.R. Lutz, S. Plumeri, H. Ricaud and R. Vernet.

**Tokyo, Japan**, University of Tokyo,\*):

H. Hamagaki and K. Ozawa.

**Trieste, Italy**, Dipartimento di Fisica dell'Università and Sezione INFN:

V. Bonvicini, O. Borysov<sup>26)</sup>, L. Bosisio, M. Bregant, P. Camerini, E. Cattaruzza, G. Contin, E. Fragiaco, N. Grion, G. Margagliotti, S. Piano, I. Rachevskaya, A. Rachevski, R. Rui, F. Soramel<sup>29)</sup> and A. Vacchi.

**Turin, Italy**, Dipartimenti di Fisica dell'Università and Sezione INFN:

B. Alessandro, R. Arnaldi, S. Bagnasco, G. Batigne, S. Beolè, E. Bruna, P. Cerello, E. Chiavassa, O. Cobanoglu, S. Coli, E. Crescio, N. De Marco, P. De Remigis, A. Ferretti, M. Gagliardi, M. Gallio, L. Gaudichet, R. Gemme, G. Giraud, P. Giubellino, M. Idzik, S. Martoiu, A. Marzari Chiesa, M. Maserà, G. Mazza, P. Mereu, M. Monteno, A. Musso, D. Nouais, C. Oppedisano, A. Piccotti, F. Poggio, F. Prino, L. Riccati, A. Rivetti, E. Scomparin, S. Senyukov, L. Simonetti, D. Stocco, F. Tosello, L. Toscano, E. Vercellin, R. Wheadon and F. Yermia.

**Tsukuba, Japan**, University of Tsukuba,\*):

Y. Miake and S. Esumi.

**Utrecht, The Netherlands**, Subatomic Physics Department, Utrecht University and National Institute for Nuclear and High Energy Physics (NIKHEF):

A.P. De Haas, C. Ivan, R. Kamermans, A. Mischke, G. Nooren, C.J. Oskamp, Th. Peitzmann, E. Simili, O. Sokolov, A. Van Den Brink and N. Van Eijndhoven.

**Wako-shi, Japan**, RIKEN\*):

H. Enyo, K. Fujiwara, H. Kano and H. Onishi.

**Warsaw, Poland**, Soltan Institute for Nuclear Studies:

A. Deloff, T. Dobrowolski, K. Karpio, M. Malek, H. Malinowski, K. Redlich<sup>27)</sup>, T. Siemiarczuk, G. Stefanek<sup>28)</sup>, L. Tykarski and G. Wilk.

**Warsaw, Poland**, University of Technology, Institute of Physics:

Z. Chajecski, H. Gos, M. Janik, M. Jedynek, A. Kisiel, T.J. Pawlak, W.S. Peryt, J. Pluta, P. Skowronski, M. Slodkowski, P. Szuba and T. Traczyk.

**West Lafayette, USA**, Department of Physics, Purdue University<sup>†)</sup>:

R.P. Scharenberg, B. Srivastava and F.H. Wang.

**Worms, Germany**, University of Applied Sciences Worms, ZTT\*):

E.S. Conner and R. Keidel.

**Wuhan, China**, Institute of Particle Physics, Huazhong Normal University:

X. Cai, H.T. Ding, H. Liu, X.R. Wang, H.Y. Yang, Z.B. Yin and D.C. Zhou.

**Wuhan, China**, Huazhong Univ. of Science and Techn. Electronic and Inform. Engineering:

X. Cao, Q.X. Li, Y.Z. Liu, G. Su, L. Tan and G.X. Zhu.

**Yerevan, Armenia, Yerevan Physics Institute:**

M. Atayan, A. Grigoryan, H. Gulkanyan, A. Harutyunyan, A. Hayrapetyan, V. Kakoyan, M. Poghosyan, T. Poghosyan and G. Sargsyan.

**Zagreb, Croatia, Ruder Bošković Institute:**

T. Antić, K. Kadija and T. Susa.

- 
- \*<sup>)</sup> Associate member.
  - †<sup>)</sup> Applying to join the collaboration.
  - 1<sup>)</sup> Marie Curie fellow at Physics Department, CERN, Geneva, Switzerland.
  - 2<sup>)</sup> On leave from Institute of Particle Physics, Huazhong Normal University, Wuhan, China.
  - 3<sup>)</sup> On leave from Institute of Experimental Physics, Košice, Slovakia.
  - 4<sup>)</sup> Now at Gesellschaft für Schwerionenforschung (GSI), Darmstadt, Germany.
  - 5<sup>)</sup> On leave from JINR, Dubna, Russia.
  - 6<sup>)</sup> Supported by EGEE.
  - 7<sup>)</sup> On leave from INFN CNAF, Bologna, Italy.
  - 8<sup>)</sup> National Institute for Physics and Nuclear Engineering, Bucharest, Romania.
  - 9<sup>)</sup> On leave from Division of Experimental High Energy Physics, University of Lund, Lund, Sweden.
  - 10<sup>)</sup> On leave from Comenius University, Faculty of Mathematics, Physics and Informatics, Bratislava, Slovakia.
  - 11<sup>)</sup> Now at INFN, Sezione di Firenze, Firenze, Italy.
  - 12<sup>)</sup> On leave from Variable Energy Cyclotron Centre (VECC), Kolkata, India.
  - 13<sup>)</sup> On leave from INFN, Sezione di Torino, Turin, Italy.
  - 14<sup>)</sup> On leave from Laboratoire de Physique Subatomique et des Technologies Associées (SUBATECH), Ecole des Mines de Nantes, IN2P3-CNRS and Université de Nantes, Nantes, France.
  - 15<sup>)</sup> On leave from Budapest University, Budapest, Hungary.
  - 16<sup>)</sup> On leave from Yerevan Physics Institute, Yerevan, Armenia.
  - 17<sup>)</sup> Cracow Technical University, Cracow, Poland.
  - 18<sup>)</sup> On leave from National Institute for Physics and Nuclear Engineering, Bucharest, Romania.
  - 19<sup>)</sup> Institute of Physics and Technology, Mongolian Academy of Sciences, Ulaanbaatar, Mongolia.
  - 20<sup>)</sup> Institute of Space Sciences, Bucharest, Romania.
  - 21<sup>)</sup> Institute of Physics, Georgian Academy of Sciences, Tbilisi, Georgia.
  - 22<sup>)</sup> High Energy Physics Institute, Tbilisi State University, Tbilisi, Georgia.
  - 23<sup>)</sup> Research Centre for Applied Nuclear Physics (RCANP), Dubna, Russia.
  - 24<sup>)</sup> Department of Physics, Ohio State University, Columbus, USA.
  - 25<sup>)</sup> On leave from Università degli Studi di Cassino and INFN, Pisa, Italy.
  - 26<sup>)</sup> On leave from Department of High Density Physics, Kiev, Ukraine.
  - 27<sup>)</sup> Institute of Theoretical Physics, University of Wrocław, Wrocław, Poland and Physics Department, CERN, Geneva, Switzerland.
  - 28<sup>)</sup> Institute of Physics, Pedagogical University, Kielce, Poland.
  - 29<sup>)</sup> Udine, Italy, Dipartimento di Fisica dell'Università and Gruppo Collegato INFN
  - 30<sup>)</sup> On leave from Bari, Italy, Dipartimento di Fisica dell'Università and Sezione INFN.
  - 31<sup>)</sup> Presently at Kent, USA, Kent State University.
  - 32<sup>)</sup> On leave from Münster, Germany, Institut für Kernphysik Westfälische Wilhelms-Universität.

## **Acknowledgements**

The Collaboration wishes to thank all the administrative and technical staff involved during the preparation of the EMCal Addendum to the ALICE TP and in particular: the ALICE secretariat, M. Connor, U. Genoud, and C. Herve; the CERN Desktop Publishing Service, in particular S. Leech O'Neale and C. Vanoli; and the CERN printshop.



# Contents

---

|          |   |           |
|----------|---|-----------|
| <b>1</b> | <b>Introduction</b>   | <b>1</b>  |
| 1.1      | Physics Motivation . . . . .                                    | 1         |
| 1.1.1    | Jet Quenching in Nuclear Collisions . . . . .                   | 1         |
| 1.1.2    | The ALICE Electromagnetic Calorimeter . . . . .                 | 3         |
| <b>2</b> | <b>Detector Design</b>  | <b>7</b>  |
| 2.1      | Design Overview . . . . .                                       | 7         |
| 2.2      | Module Design . . . . .   | 8         |
| 2.2.1    | Sampling Fraction . . . . .                                     | 9         |
| 2.2.2    | Optical System and Photo Sensors . . . . .                      | 11        |
| 2.3      | Module Integration to Strip Modules and Super Modules . . . . . | 14        |
| 2.4      | Mechanical Analysis . . . . .                                   | 16        |
| 2.4.1    | Super Module Crate . . . . .                                    | 17        |
| 2.4.2    | Strip Module . . . . .  | 17        |
| <b>3</b> | <b>Electronics</b>  | <b>19</b> |
| 3.1      | Overall Electronics Architecture . . . . .                      | 19        |
| 3.1.1    | APD and Preamplifier . . . . .                                  | 19        |
| 3.1.2    | Front End Card: Shaper and Digitization . . . . .               | 20        |
| 3.1.3    | Trigger Input . . . . .   | 21        |
| 3.1.4    | Readout and Control . . . . .                                   | 21        |
| 3.1.5    | Mechanical . . . . .  | 21        |
| 3.2      | EMCal Specific Readout Considerations . . . . .                 | 22        |
| 3.2.1    | APD and Preamplifier . . . . .                                  | 22        |
| 3.2.2    | Dynamic Range . . . . .   | 22        |
| 3.2.3    | Light Yield . . . . .   | 22        |
| 3.2.4    | Shaper Time Constant Optimization . . . . .                     | 23        |
| 3.2.5    | Late Neutron Background . . . . .                               | 24        |
| 3.2.6    | EMCal Energy Resolution Contributions . . . . .                 | 24        |
| 3.3      | The FEE Shaper . . . . .  | 25        |
| 3.4      | Installation of EMCal Read Out . . . . .                        | 27        |
| <b>4</b> | <b>Data Acquisition and Online</b>                              | <b>29</b> |
| 4.1      | Requirements . . . . .  | 29        |
| 4.2      | DAQ Architecture Overview . . . . .                             | 29        |
| 4.3      | DAQ-HLT Interface . . . . .                                     | 30        |
| 4.4      | Data Volume and Bandwidth . . . . .                             | 31        |
| 4.5      | EMCal Detector Control . . . . .                                | 32        |
| <b>5</b> | <b>Detector Calibration and Monitoring</b>                      | <b>35</b> |
| 5.1      | Requirements . . . . .  | 35        |
| 5.2      | LED Calibration System . . . . .                                | 35        |
| 5.3      | APD pre-Calibration . . . . .                                   | 36        |
| 5.4      | Cosmic Ray Calibration . . . . .                                | 36        |
| 5.5      | Gain Monitoring During Runs . . . . .                           | 36        |
| 5.6      | In-beam MIP, Electron, and $\pi^0$ Calibrations . . . . .       | 37        |

|          |  |           |
|----------|--|-----------|
| <b>6</b> | <b>Test Beam Activities and Results</b>                    | <b>39</b> |
| 6.1      | Test Beam Measurements at FNAL . . . . .                   | 39        |
| 6.1.1    | Goals and Setup . . . . .                                  | 39        |
| 6.1.2    | Measurements and Analysis . . . . .                        | 40        |
| 6.1.3    | LED Calibration Results . . . . .                          | 41        |
| 6.1.4    | Light Yield . . . . .                                      | 42        |
| 6.1.5    | Beam Results . . . . .                                     | 44        |
| <b>7</b> | <b>Physics Performance</b>                                 | <b>49</b> |
| 7.1      | EMCAL Trigger . . . . .                                    | 49        |
| 7.1.1    | Heavy-Ion Jet Trigger Requirements . . . . .               | 50        |
| 7.1.2    | Trigger Summary . . . . .                                  | 51        |
| 7.2      | Material Distribution . . . . .                            | 52        |
| 7.3      | Jet Reconstruction . . . . .                               | 52        |
| 7.3.1    | Jet Background Reduction . . . . .                         | 53        |
| 7.3.2    | Jet Energy Resolution . . . . .                            | 54        |
| 7.3.3    | Jet Measurement Biases . . . . .                           | 56        |
| 7.4      | $\gamma/\pi^0$ Discrimination and Direct Photons . . . . . | 58        |
| 7.5      | Heavy Quark Jets . . . . .                                 | 60        |
| <b>8</b> | <b>Integration and Implementation</b>                      | <b>61</b> |
| 8.1      | EMCal Support Structure - General . . . . .                | 61        |
| 8.2      | CalFrame Design Constraints . . . . .                      | 62        |
| 8.3      | CalFrame Structural Analysis . . . . .                     | 63        |
| 8.4      | CalFrame Integration and Installation . . . . .            | 65        |
| 8.4.1    | CalFrame Assembly . . . . .                                | 65        |
| 8.4.2    | Super Module Rails . . . . .                               | 65        |
| 8.4.3    | Super Module Installation Test . . . . .                   | 66        |
| 8.4.4    | CalFrame Load Test . . . . .                               | 66        |
| 8.5      | CalFrame Installation into ALICE . . . . .                 | 66        |
| 8.6      | CalFrame and Super Module Alignment . . . . .              | 67        |
| 8.7      | Services, Access, and Maintenance . . . . .                | 67        |
| 8.7.1    | Services . . . . .   | 67        |
| 8.7.2    | Access and Maintenance . . . . .                           | 67        |
| 8.8      | Safety Considerations. . . . .                             | 68        |
| <b>9</b> | <b>Planning and Organisation</b>                           | <b>69</b> |
| 9.1      | Schedule . . . . .   | 69        |
| 9.2      | Cost Estimate . . . . .                                    | 69        |
| 9.3      | Responsibilities . . . . .                                 | 69        |
|          | <b>References</b>  | <b>71</b> |

# 1 Introduction

---

## 1.1 Physics Motivation

ALICE (A Large Ion Collider Experiment) at the LHC contains a wide array of detector systems for measuring hadrons, leptons, and photons. ALICE is designed to carry out comprehensive measurements of high energy nucleus–nucleus collisions, in order to study QCD matter under extreme conditions and to study the phase transition between confined matter and the Quark-Gluon Plasma (QGP). Discussion of the full ALICE physics program can be found in [1, 2].

The interaction and energy loss of high energy partons in matter provides a sensitive tomographic probe of the medium generated in high energy nuclear collisions (“jet quenching”) [3–6]. Jet quenching measurements have played a key role at the Relativistic Heavy Ion Collider (RHIC) [7–10] and will be central to the study of nuclear collisions at the LHC.

This addendum to the ALICE Technical Proposal describes a large acceptance Electromagnetic Calorimeter (EMCal) that will be installed in the ALICE central detector. The EMCal enhances ALICE’s capabilities for jet quenching measurements. The addition of the EMCal enables triggering on high energy jets, reduces significantly the measurement bias for jet quenching studies, improves jet energy resolution, and augments existing ALICE capabilities to measure high momentum photons and electrons. Combined with ALICE’s excellent capabilities to track and identify particles from very low  $p_t$  to high  $p_t$  the EMCal enables an extensive study of jet quenching at the LHC.

### 1.1.1 Jet Quenching in Nuclear Collisions

Hard (high  $Q^2$ ) scatterings occur in the initial stage of a high energy nucleus–nucleus collision, producing high  $E_T$  partons that must traverse the bulk matter generated in the collision before fragmenting in vacuum into a jet of hadrons. The scattered partons interact with the matter, losing energy through both radiative [3–5] and elastic channels [11–13], with the magnitude of the energy loss depending strongly on the density of the medium. The energy loss effectively softens the fragmentation of the jet, resulting in suppression of high  $p_t$  hadrons and enhancement of the soft jet multiplicity. The jet structure may in addition be broadened, and its shape may be deformed by interaction with the flowing matter. Measurements of jet quenching effects have the potential to probe the medium at the hottest, densest stage of the collision.

However, jet measurements in high energy nucleus–nucleus collisions must contend with the large background of soft hadrons in the underlying event. Jet measurements in nuclear collisions at RHIC have therefore concentrated until now on high  $p_t$  hadrons and their correlations. Fig. 1.1, left panel, shows the large suppression of the high  $p_t$  inclusive hadron yield in central 200 GeV Au-Au collisions, together with the lack of similar suppression for direct photons [14]. This contrast, as well as comparison to hadron production in d–Au collisions [15–18], shows that the suppression results from final state interaction of high energy partons with dense matter generated in the collision. The curve in the figure is the result of a radiative energy loss calculation in the few-scattering GLV approximation, which reproduces the measured suppression for initial gluon density  $dN^g/dy \sim 1100$ , about 30 times the density of cold matter [19]. The figure suggests that large  $p_t > 6$  GeV/ $c$  is required to separate QCD radiative effects from non-perturbative phenomena. Measurements of particle-identified yields have also shown a large enhancement in the yield of baryons relative to mesons in the intermediate  $p_t$  region  $\sim 2 - 5$  GeV/ $c$  at RHIC [20, 21]. This has been interpreted in a parton coalescence picture, indicating an interplay between the fragmentation of hard scattered partons and the hadronization of the bulk medium [22–24].

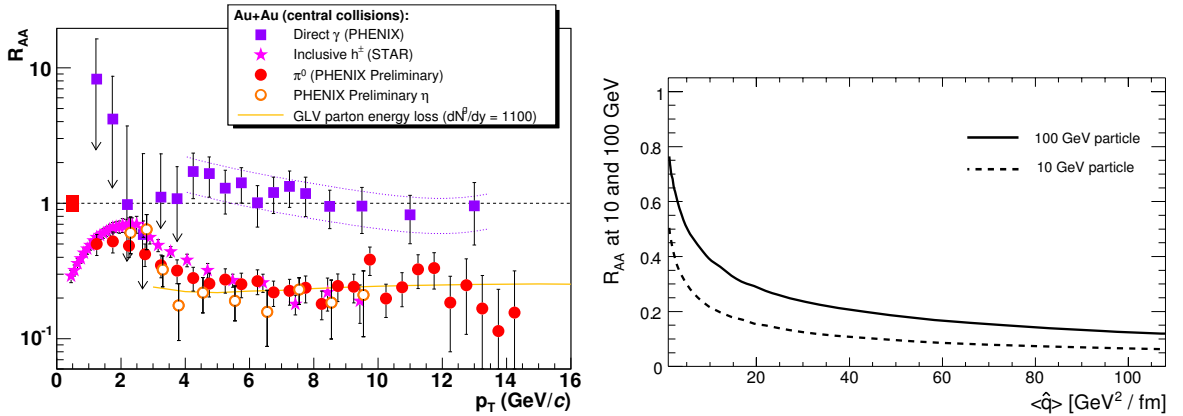


**Figure 1.1:** Inclusive hadron suppression at RHIC. Left: Hadron and direct photon yields in central 200 GeV Au-Au collisions normalized by p-p collision yields (figure from [25]). Right: hadron suppression as a function of transport coefficient  $\hat{q}$  [26].

Fig. 1.1, right panel, shows an alternative calculation of inclusive hadron suppression based on a multiple soft collision approximation to radiative energy loss [26, 27]. In this approach the medium is parametrized by a transport coefficient  $\hat{q} = \mu^2/\lambda$ , where  $\mu$  is the typical momentum transfer and  $\lambda$  is the gluon mean free path [28]. The transport coefficient is related to the energy density  $\epsilon$  of the medium via  $\hat{q} = c\epsilon^{3/4}$ , with  $c \sim 2 - 10$  [28]. Comparison of data in the left panel to the curve for 10 GeV particles requires  $\hat{q} \sim 10 \text{ GeV}^2/\text{fm}$ . However, the inclusive suppression is seen to have little sensitivity to  $\hat{q}$  over a very large range: for a sufficiently opaque medium, the inclusive yield is dominated by jets suffering relatively little energy loss, which are those jets generated at the periphery of the collision zone and headed outwards [28–30]. This bias fundamentally limits the sensitivity of inclusive hadron measurements as a probe of the medium.

Expectations for inclusive hadron suppression at the LHC can also be derived from the figure by scaling  $\hat{q}$  with the expected increase in initial gluon density from RHIC to the LHC, giving  $\hat{q}_{LHC} \sim 70 \text{ GeV}^2/\text{fm}$  [28]. A large variation in suppression is not predicted, despite the large variation in initial density. Comparison of the suppression for 10 and 100 GeV particles shows that a large range in  $p_t$  is needed to study the logarithmic QCD evolution, which is only possible at the LHC. Overall, inclusive hadron suppression has only weak sensitivity to properties of the medium, and much more information can be gleaned from detailed study of jet structure.

Additional evidence for jet quenching is seen in Fig. 1.2, which shows RHIC measurements of the azimuthal distribution of high  $p_t$  hadron pairs [18]. The back-to-back correlation expected from di-jets is seen in p-p and d-Au collisions, while the di-jet correlation is strongly suppressed in central Au-Au collisions. In this measurement the “trigger” hadron likewise has a surface bias, meaning that the jet recoiling against the trigger is directed towards the dense core of the collision zone. The high  $p_t$  fragments of the recoiling jet are seen to be strongly suppressed, also indicating substantial partonic energy loss in the medium. Its energy and momentum must be conserved, however, and indeed an enhanced correlation of low  $p_t$  hadrons is seen for the recoil in central Au-Au collisions [31], with features suggesting that the energy lost to the medium has to a large extent been equilibrated.

These measurements show clear evidence for jet quenching, but the kinematic reach at RHIC is limited. Full reconstruction of the relatively low energy jets accessible at RHIC is difficult, due to poor signal/background. Jet studies at RHIC therefore rely on leading hadron measurements, with the accompanying fragmentation and geometric biases.

Nuclear collisions at the LHC will enable qualitatively new measurements of jet quenching. The factor 30 increase in  $\sqrt{s_{NN}}$  relative to RHIC corresponds to a huge increase in kinematic and statistical

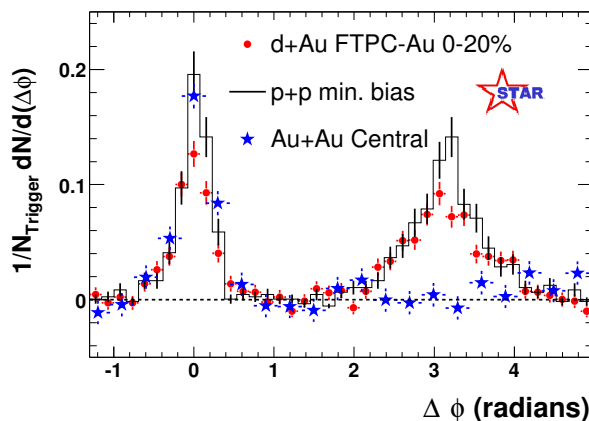


**Figure 1.2:** Back-to-back high  $p_t$  hadron pairs at RHIC [18].

reach for hard probes, and new measurement channels become available. Most importantly, there is copious production of high energy jets that are clearly distinguishable over background, and event-wise jet reconstruction with reasonable energy resolution becomes possible. Recovery of a large fraction of the jet energy will reduce sensitivity to the specific patterns of fragmentation, avoiding the strong biases of leading particle analyses. The resulting jet sample will give a much more detailed and complete view of partonic energy loss and the medium-induced modifications of jet fragmentation.

Guidance for the  $p_t$  scale of hadron production from high  $E_T$  jets arising from medium-induced radiation can be obtained from a recent calculation which incorporates medium effects into the Modified Leading Logarithmic Approximation (MLLA) [32]. Fig. 1.3, left panel, shows the hadron multiplicity distribution plotted as a function of the scaling variable  $\xi = \log(1/x)$ , with  $x = (p_t^{\text{hadron}}/E_T^{\text{jet}})$ . Large effects are seen in both the low  $p_t$  and the high  $p_t$  regions, with suppression of hard fragments (low  $\xi$ ) and a marked enhancement for the softest fragments (high  $\xi$ ). The medium-induced excess for jets with  $E_T \sim 100$  GeV is predicted to be large for  $p_t \sim 1\text{--}5$  GeV/ $c$ , matching well the unique ALICE momentum reconstruction and PID capabilities.

Partonic energy loss will be reflected in the modification of jet observables such as jet shapes and multiplicity distributions. Calculations suggest that the broadening of the jet multiplicity distribution provides a sensitive probe of the matter [33]. Fig. 1.3, right panel, shows the gluon multiplicity distribution within a jet cone  $R = 0.3$  as a function of momentum  $k_t$  perpendicular to the jet direction. The distribution from fragmentation in vacuum is shown, together with its broadening due to interactions in the medium. A significant medium-induced enhancement is seen at  $k_t \sim \text{few GeV}/c$ , calculated both in the “single hard” and “multiple soft” collision approximations for radiative energy loss,  $\omega_c = \frac{1}{2}\hat{q}L^2$ , where  $L$  is the path length in medium.  $\omega_c$  is the effective cutoff of the radiated spectrum and is proportional to the total energy loss  $\Delta E \sim \alpha_s \omega_c$ .

Potentially the most detailed investigation of jet quenching utilizes the coincidence of a jet recoiling from a direct photon. The colourless photon does not interact with the medium, providing a measurement of the recoiling jet energy [34]. The fragmentation function can then be studied in detail on an inclusive basis using charged particle tracking.

### 1.1.2 The ALICE Electromagnetic Calorimeter

ALICE is designed for measurements in the high multiplicity environment of heavy ion collisions and is well suited for jet quenching studies. It has excellent momentum resolution for charged particles from 100 MeV/ $c$  to 100 GeV/ $c$ , covering nearly the full range of fragment momentum for the highest energy jets accessible in heavy ion collisions. ALICE has a wide array of particle identification capabilities

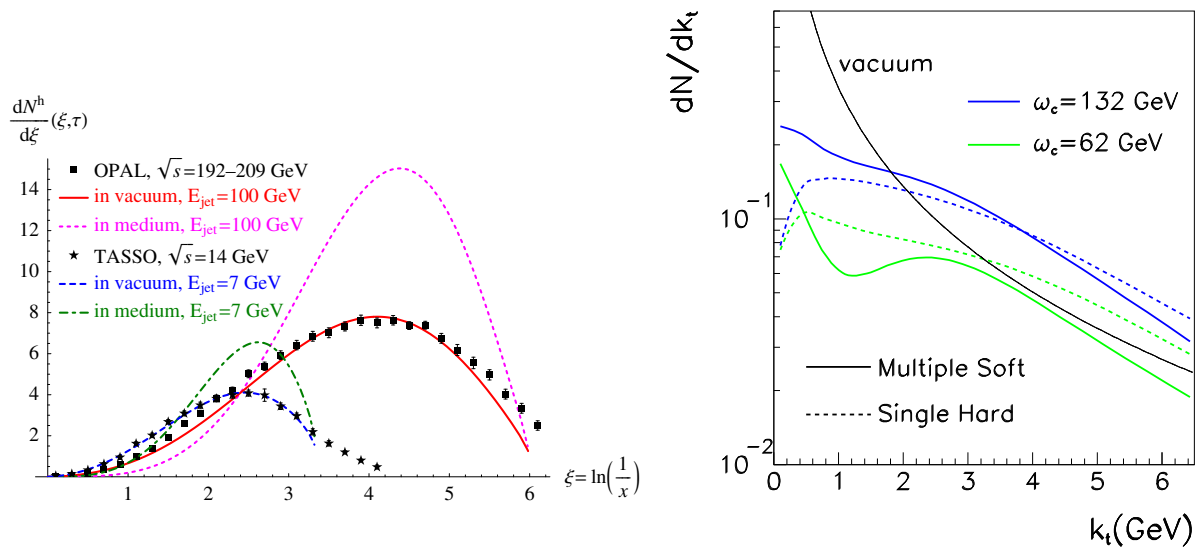


**Figure 1.3:** Left: MLLA calculations of the single inclusive hadron distribution as function of  $\xi=\log(1/x)$  for vacuum fragmentation compared to  $e^+e^-$  data and for medium-modified jet.  $\xi=4$  corresponds to  $p_t^{hadron} \sim 2$  GeV for  $E^{jet} = 100$  GeV. Right: Gluon multiplicity distribution in a jet cone of radius  $R = 0.3$  in vacuum and in the medium.

which, as demonstrated at RHIC, will be crucial to understand the mechanisms of particle production from jet fragmentation and hadronization of the bulk medium.

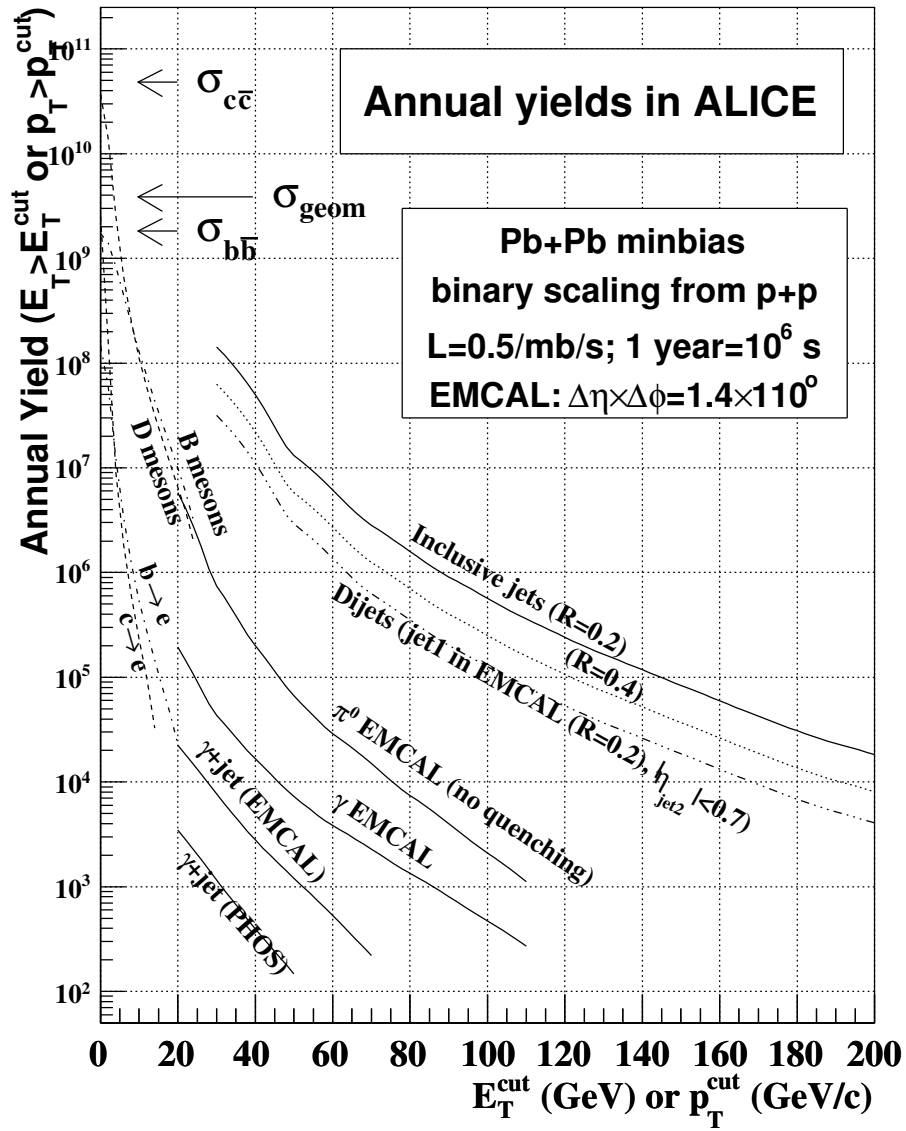
The EMCal will complete ALICE's capabilities to measure jet quenching. The most important features of the EMCal are an efficient and unbiased fast trigger (Level 0/1) for high energy jets, and measurement of the neutral portion of jet energy. Jet measurements based solely on charged particle reconstruction are subject to large measurement biases. This bias puts severe limitations on jet quenching studies, since it is precisely the modification of jet structure that is the observable. The addition of the EMCal allows measurement of a large fraction of jet energy, thereby reducing the sensitivity of jet reconstruction to specific jet structure and enabling a comprehensive study of jet quenching. The EMCal will also improve jet energy resolution, and enhance ALICE capabilities to measure high  $p_t$  photons, neutral hadrons, and electrons.

Fig. 1.4 shows the annual yield for various hard processes in the EMCal acceptance, for minimum bias Pb–Pb collisions at nominal luminosity<sup>1</sup>. The EMCal kinematic reach for inclusive jets extends beyond 200 GeV, while for di-jets with a trigger jet in the EMCal and the recoiling jet in the TPC acceptance it is about 170 GeV. The  $\gamma$ -jet rate is statistically robust for  $p_t \leq 40$  GeV/ $c$ , while the yield for inclusive electrons from semi-leptonic decays of b and c extends to  $p_t \sim 25$  GeV/ $c$ . Study of heavy quark jet production is of interest because the energy loss is expected to differ from that of light quark and gluon jets.

ALEPH [35] and STAR [36] have shown that jet measurements based on EM calorimetry and charged particle tracking have similar energy resolution to EM and hadronic calorimetry. As will be detailed in Section 7.3, charged particle tracking is in fact superior to hadronic calorimetry for suppressing backgrounds to jet measurements in the high multiplicity environment of heavy ion collisions. The EMCal is therefore an important addition to ALICE for jet quenching studies.

Full exploitation of jets as a probe of QCD matter at the LHC requires both broad kinematic reach of jet energy and detailed measurement of jet structure, from the hardest hadronic fragments to very

<sup>1</sup>Due to the scaling of hard process cross sections and LHC luminosity with system size, similar annual yields are also expected for lighter collision systems.



**Figure 1.4:** Annual hard process yields expected in the EMCAL acceptance for minimum bias Pb–Pb collisions at 5.5 TeV.

soft fragments. Much of the interesting physics may indeed be carried by low  $p_t$  hadrons, which have the greatest sensitivity to the jet interaction with the medium. In light of RHIC measurements [20, 21], particle identification is expected to be critical in elucidating the physics of jet quenching. The EMCal acceptance, triggering and measurement capabilities, combined with the excellent tracking and particle identification capabilities of ALICE, enable the most extensive measurements of jet quenching at the LHC.



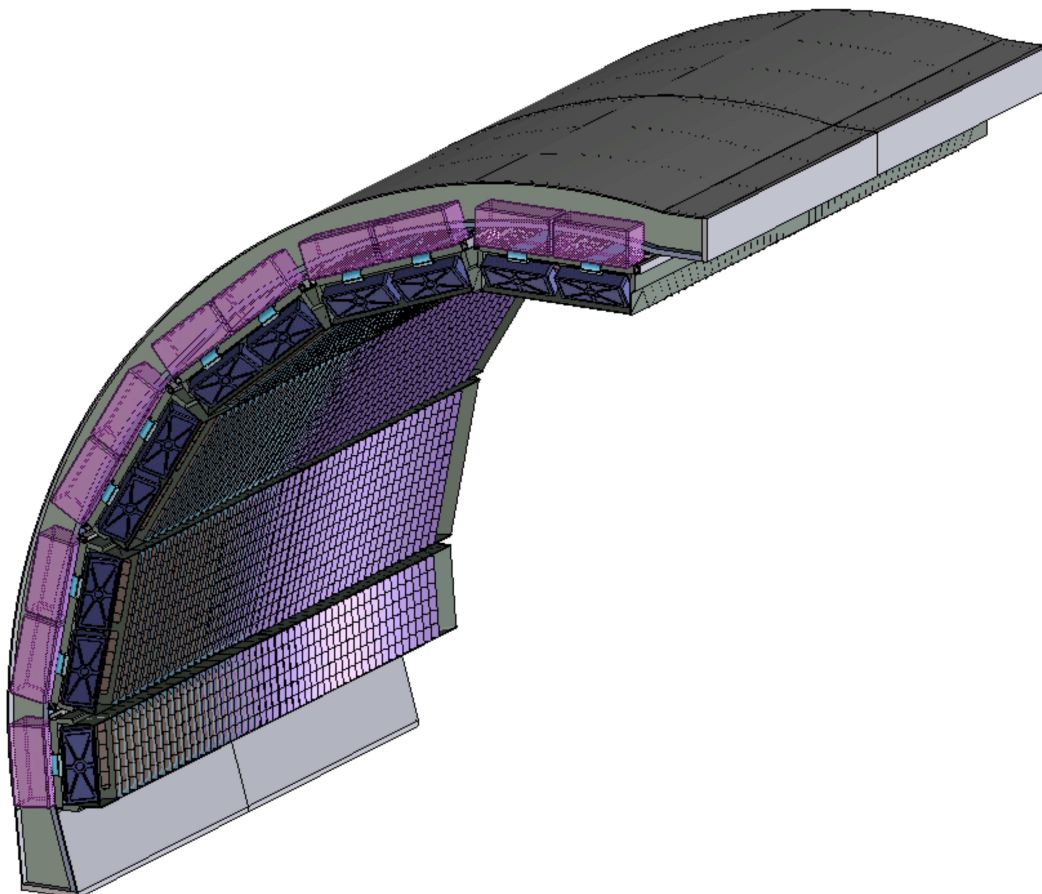
## 2 Detector Design

---

### 2.1 Design Overview

The overall design of the EMCal is heavily influenced by its integration within the ALICE [1] magnet. The EMCal is to be located inside the large room temperature solenoidal magnet of ALICE within a cylindrical integration volume approximately 112 cm deep in the radial direction sandwiched between the ALICE spaceframe and the ALICE magnet coils. Due to the installation of the PHOS carriage below the ALICE TPC and the HMPID above the ALICE TPC, the EMCal is limited to a region of about 110 degrees in azimuth above the TPC adjacent to the HMPID. As discussed in Section 1, this EMCal acceptance is well matched to ALICE physics goals.

The conceptual design of the electromagnetic calorimeter for the ALICE experiment is based on the Shashlik technology as implemented in the PHENIX experiment [2] at RHIC, HERA-B at DESY or LHCb [3] at CERN. The scope and basic design parameters of the proposed calorimeter have been chosen to match the physics performance requirements of the high  $p_t$  physics program.



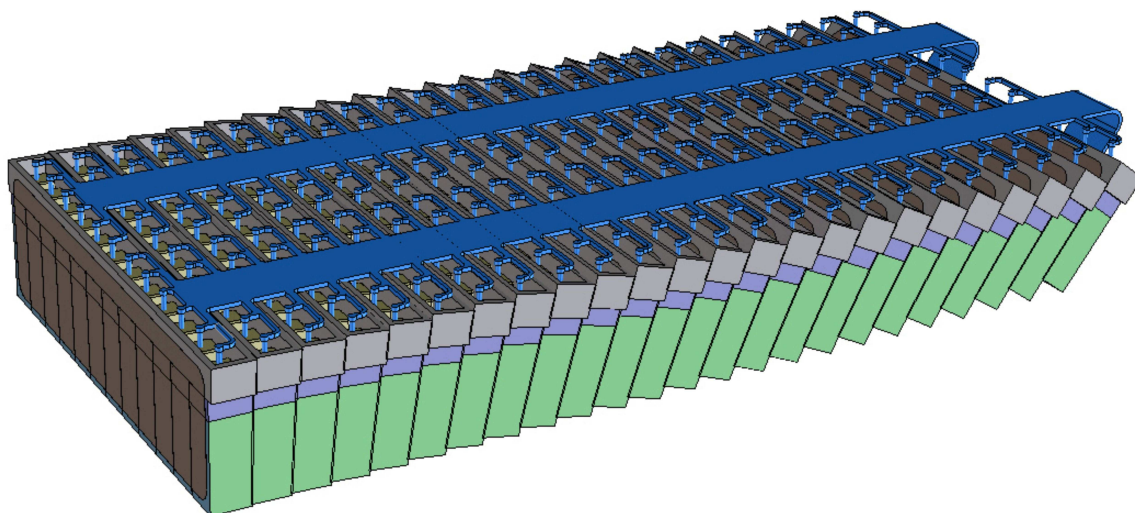
**Figure 2.1:** The array of super modules shown in the installed position on their support structure.

Fig. 2.1 shows the EMCal super modules mounted in the installed position on their support structure. A continuous arch of super modules, each spanning  $\sim 20$  degrees in azimuth, is indicated. The EMCal is positioned to provide partial back-to-back coverage with the ALICE Photon Spectrometer (PHOS)

calorimeter. Small azimuthal gaps ( $\sim 3.0$  cm) are provided between super modules to facilitate installation and alignment. These gaps are positioned in line with the TPC sector boundaries. Along these sector boundaries, there is substantial additional structural material required for the support of the TPC and other ALICE detectors that would significantly degrade any electromagnetic measurements made in these gaps.

The chosen technology is a layered Pb-scintillator sampling calorimeter with a longitudinal pitch of 1.44 mm Pb and 1.76 mm scintillator<sup>1</sup> with longitudinal wavelength shifting fibre light collection (Shashlik). The full detector spans  $\eta = -0.7$  to  $\eta = 0.7$  with an azimuthal acceptance of  $\Delta\phi = 110^\circ$ . The detector is segmented into 12672 towers, each of which is approximately projective in  $\eta$  and  $\phi$  to the interaction vertex.

The towers are grouped into super modules of two types: full size which span  $\Delta\eta = 0.7$  and  $\Delta\phi = 20^\circ$ , and half size which span  $\Delta\eta = 0.7$  and  $\Delta\phi = 10^\circ$ . There are 10 full size and 2 half size super modules in the full detector acceptance (Fig. 2.1). The super module is the basic structural units of the calorimeter. These are the units handled as the detector is moved below ground and rigged during installation. Fig. 2.2 shows a super module with its external mechanical structure stripped away to illustrate the stacking of modules within the super module.



**Figure 2.2:** ALICE EMCAL super module concept.

This figure shows a full size super module with  $12 \times 24$  modules configured as 24 strip modules of 12 modules each. The supporting mechanical structure of the super module has been removed so that the strip module stacking into a nearly projective geometry can be seen. The electronics integration pathways are illustrated.

Each full size super module is assembled from  $12 \times 24 = 288$  modules arranged in 24 strip modules of  $12 \times 1$  modules each. Each module has a rectangular cross section in the  $\phi$  direction and a trapezoidal cross section in the  $\eta$  direction with a full taper of  $1.5^\circ$ . The resultant assembly of stacked strip modules is approximately projective with an average angle of incidence of less than  $2^\circ$  in  $\eta$  and less than  $5^\circ$  in  $\phi$ . A single module and an assembled strip module is indicated schematically in Fig. 2.3

## 2.2 Module Design

The smallest building block of the calorimeter is the individual module illustrated in Fig. 2.3. Each individual module contains  $2 \times 2 = 4$  towers built up from 77 alternating layers of 1.44 mm Pb (1%

<sup>1</sup>To best account for materials in the space immediately before the calorimeter, the first layer of the detector is scintillator.

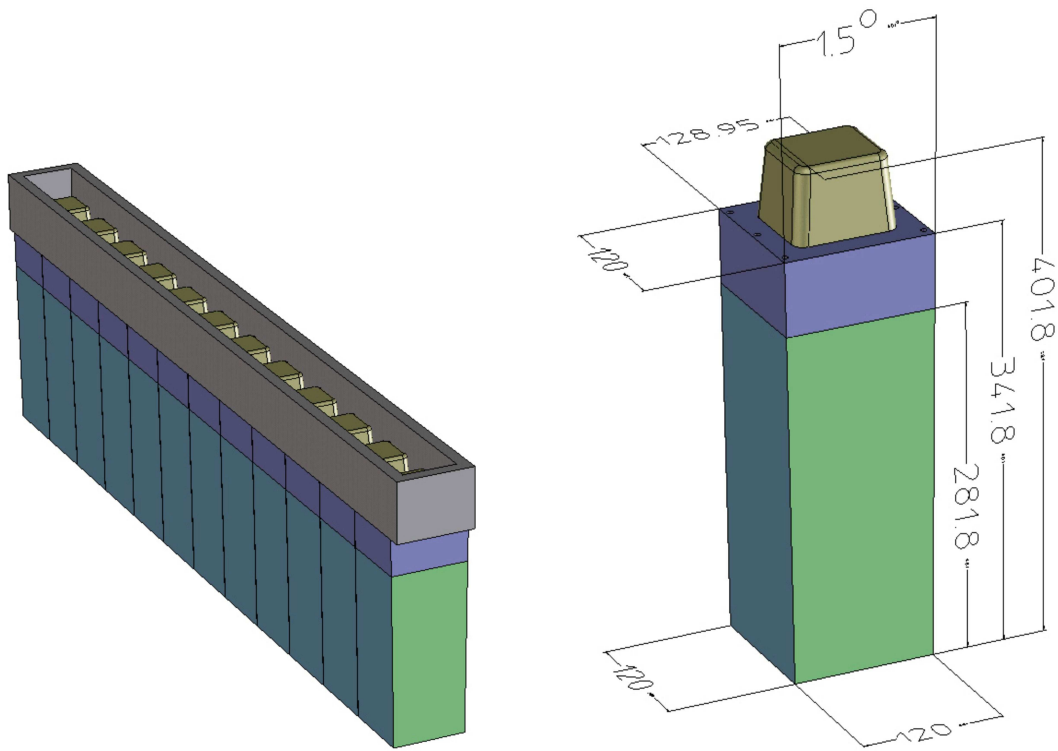


**Figure 2.3:** A single 1.5° taper module (right hand side) with the dimensions of the prototype shown in mm. The left hand figure shows a single strip module comprised of 12 EMCal modules integrated onto a single strong back.

Antimony Pb) and 1.76 mm polystyrene, injection moulded scintillator. White, acid free, bond paper serves as a diffuse reflector on the scintillator surfaces while the scintillator edges are treated with TiO<sub>2</sub> loaded reflector to provide tower to tower optical isolation and improve the transverse optical uniformity within a single tower.

The Pb-scintillator stack in a module is secured in place by the static friction between individual layers under the load of an internal pressure of  $\sim 1.3 \text{ kg/cm}^2$ . The module is closed by a skin of  $100 \mu\text{m}$  thick stainless steel welded on all four transverse surfaces to corresponding front and rear stainless steel plates. This thin stainless skin is the only inert material between the active tower volumes. The internal pressure in the module is stabilized against thermal effects, mechanical relaxation and long term flow of the Pb and/or polystyrene by a customized array of 5 non-linear spring<sup>2</sup> sets per module. In this way, each module is a self supporting unit with a stable mechanical lifetime of more than 20 years when held from its back surface in any orientation as when mounted in a strip module. Fig. 2.4 shows a cut away view of the back end of a single module illustrating the internal components used to sustain the module compression and a segment of the strip module strong back.

All modules in the calorimeter are mechanically and dimensionally identical. The front face dimensions of the towers are  $\sim 6 \times 6 \text{ cm}^2$  resulting in individual tower acceptance of  $\Delta\eta \times \Delta\phi \sim 0.014 \times 0.014$  at  $\eta=0$ .

### 2.2.1 Sampling Fraction

The present conceptual design incorporates a moderate detector average active volume density of  $\sim 5.68 \text{ g/cm}^3$  which results from a  $\sim 1 : 1.22$  Pb to scintillator ratio by volume. This results in a compact detector consistent with the EMCal integration volume at the chosen detector thickness of  $\sim 20.1$  radiation

<sup>2</sup>Bellville Washers, Rolex Inc.

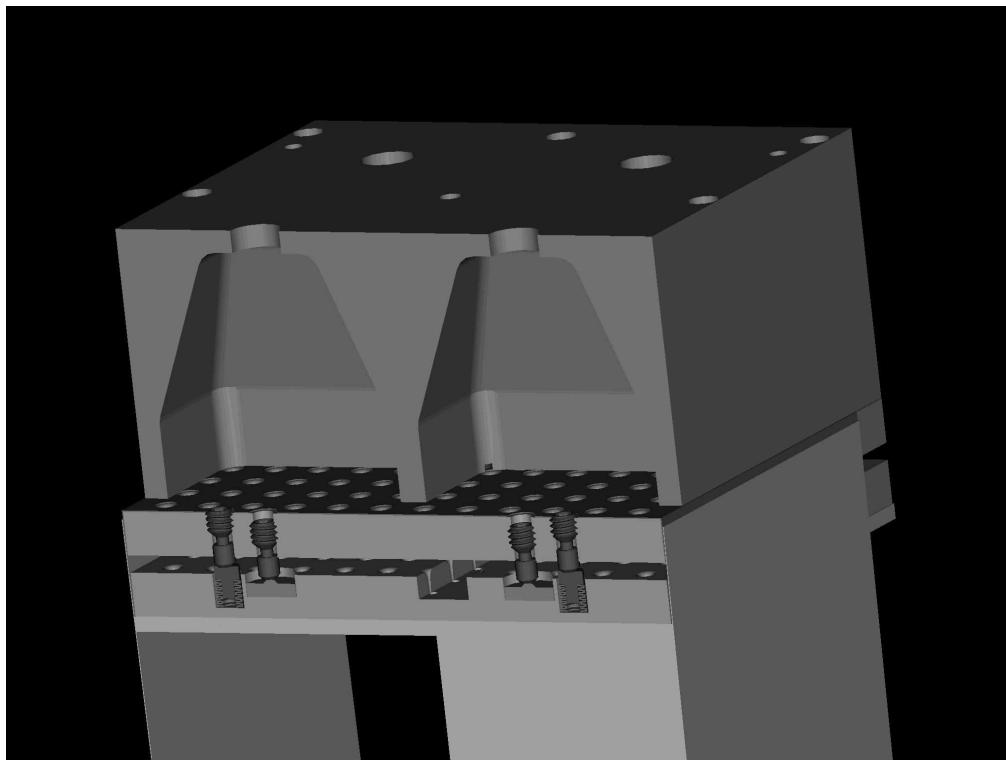


**Figure 2.4:** Cut away view of the back end of a single module showing the components that maintain the module's compression. A segment of the strip module strong back is also shown.

lengths ( $\sim 20.1 X_0$ ). In simulations, this number of radiation lengths gives a maximum deviation from linearity (due mainly to shower leakage) of  $\sim 5\%$  for the mean energy response in the range up to 100 GeV photons which is deemed acceptable.

The energy resolution of an electromagnetic calorimeter can be parameterized as

$$\sigma/E = a/\sqrt{E} \oplus b \oplus c/E, \quad (2.1)$$

where the first term characterized by the parameter  $a$  arises from stochastic fluctuations due to intrinsic detector effects such as energy deposit, energy sampling, light collection, etc. The constant term,  $b$ , arises from systematic effects, such as shower leakage, detector non-uniformity or channel-by-channel calibration errors. The third term,  $c$ , arises from electronic noise summed over the towers of the cluster used to reconstruct the electromagnetic shower. The three resolution contributions add together in quadrature as indicated in Eq. 2.1. Over the lower half of the energy range of interest in ALICE, the stochastic term dominates with the constant term increasing in significance at the highest energies.

The energy resolution for a given sampling frequency in a sampling electromagnetic calorimeter varies with the sampling frequency approximately as  $\sigma/E \sim \sqrt{d_{sc}/f_s}$  where  $d_{sc}$  is the scintillator thickness in mm and  $f_s$  is the sampling fraction for minimum ionizing particles. For optimum resolution in a given physical space and total radiation lengths, there is thus a desire to have the highest possible sampling frequency. Practical considerations, including the total assembly labour, suggest reducing the total number of Pb/scintillator layers thus decreasing the sampling frequency. Using the 1:1.22 Pb to scintillator ratio described above as a compromise - a sampling geometry of Pb(1.44 mm)/Scint(1.76 mm) - detailed GEANT3 simulations yield  $a/\sqrt{E} \oplus b\%$  with the fit results  $a = (6.90 \pm 0.09)\%$  and  $b = (1.44 \pm 0.03)\%$  over the range  $p_t = 5$  to 100 GeV/c. The simulation results are shown in Fig. 2.5. These results are based on energy deposition only and at the moment do not include photon transport

efficiencies or the electronic noise contribution. Some increase in the constant  $a$  is expected from photon transport and related effects. This has been studied in test beam measurements of an early prototype of this detector with a lower sampling frequency - Pb(1.6 mm)/Scint(1.6 mm) also shown in Fig. 2.5 - and preliminary results are consistent with a small increase in  $a$  as shown in Section 6. This will receive further study in forthcoming test beams with precisely the detector geometry described in this proposal. The value of the constant term  $b$  is dominated by shower leakage in these calculations. Other systematic effects which arise during detector fabrication and from the tower-by-tower calibration uncertainties will increase  $b$ . The latter effect is itself of the order of 1% typically. The ongoing program of test beam measurements is described in Section 6.

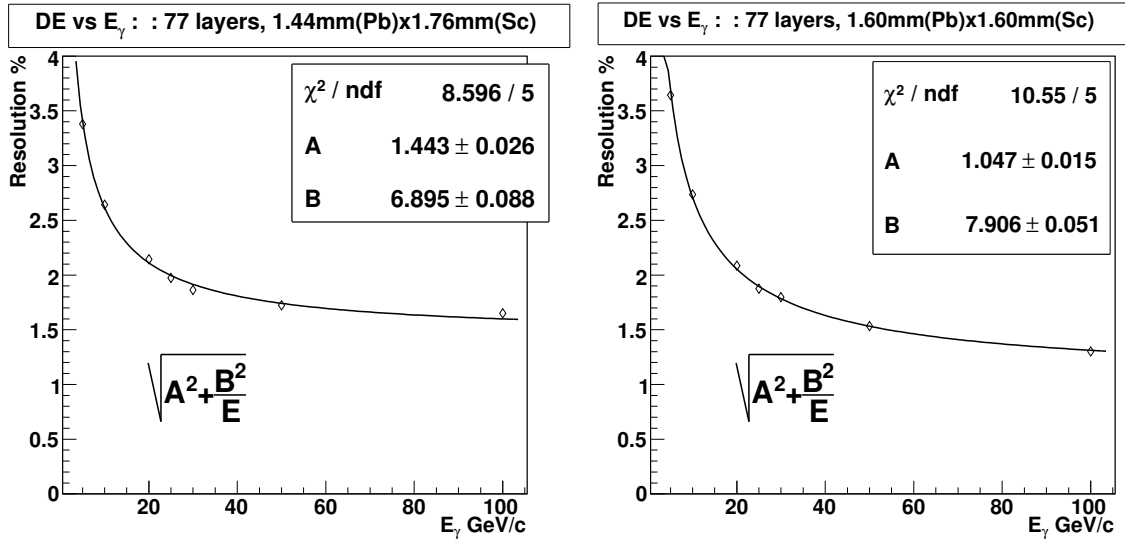


**Figure 2.5:** GEANT3 simulations of the EMCAL module resolution. Left: Proposed production module. Right: Prototype test module.

The impact of detector energy resolution on the proposed physics program has been studied. While, given the nature of the proposed physics, there is no sharp cutoff, an energy resolution for isolated electromagnetic clusters on the order of  $\sim 12\%/\sqrt{E} \oplus 2\%$  is found to be sufficient. Based on simulations and test beam results, it is expected that the EMCAL performance requirements are readily met in the relevant  $p_t$  range by the proposed sampling choice. This is discussed further in connection with first test beam results in Section 6.

The physical characteristics of the EMCAL are summarized in Table 2.1.

### 2.2.2 Optical System and Photo Sensors

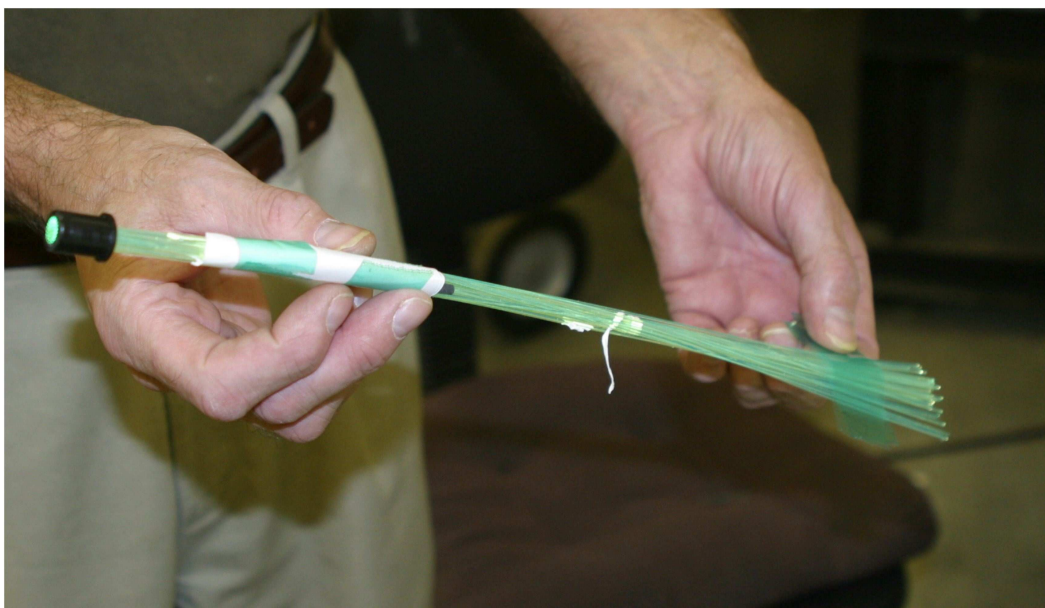
Scintillation photons produced in each tower are captured by an array of 36 Kuraray Y-11, double clad, wavelength shifting (WLS) fibres that run longitudinally through the Pb/scintillator stack. Each fibre terminates in an aluminized mirror at the front face end of the module and is integrated into a polished, circular group of 36 at the photo sensor end at the back of the module. Because the tower transverse shape deviates slightly from square as a function of longitudinal depth, we choose a fibre pattern which has exactly the same aspect ratio as the mechanical tower shape at a depth close to shower maximum. This has the effect of making the fibre pattern uniform across tower boundaries when weighted by the shower energy deposition. The properties of the selected fibres are given in Table 2.2.

The fibre bundles are pre-fabricated and inserted into the towers after the module mechanical assembly is completed. A prototype fibre bundle is shown in Fig. 2.6. The 36 individual fibres are packed into a circular array 6.8 mm in diameter and held in place inside a custom injection moulded grommet by Bicon BC-600 optical cement. An optical quality finish is applied to the assembled bundle using

**Table 2.1:** The EMCal Physical Parameters.

| Quantity                         | Value  |
|----------------------------------|--|
| Tower Size (at $\eta=0$ )        | $\sim 6.0 \times \sim 6.0 \times 24.6 \text{ cm}^3$ (active) |
| Tower Size                       | $\Delta\phi \times \Delta\eta = 0.0143 \times 0.0143$        |
| Sampling Ratio                   | 1.44 mm Pb / 1.76 mm Scintillator                            |
| Number of Layers                 | 77   |
| Effective Radiation Length $X_0$ | 12.3 mm  |
| Effective Moliere Radius $R_M$   | 3.20 cm  |
| Effective Density                | 5.68 g/cm <sup>3</sup>                                       |
| Sampling Fraction                | 10.5   |
| Number of Radiation Lengths      | 20.1   |
| Number of Towers                 | 12,672   |
| Number of Modules                | 3168   |
| Number of Super Modules          | 10 full size, 2 half size                                    |
| Weight of Super Module           | $\sim 7.7$ metric tons (full size)                           |
| Total Coverage                   | $\Delta\phi = 110^\circ, -0.7 < \eta < 0.7$                  |

a diamond polishing machine. At the other end of the bundle, individual fibres are similarly polished and mirrored with a sputtered coat of aluminum and a sputtered overcoat of  $\text{Al}_2\text{O}_3$  for protection of the mirror.

**Figure 2.6:** A prototype EMCal fibre bundle of 36 fibres.

A number of optical studies have been completed to assess the light transmission through individual fibres and the efficacy of the mirror applied to the fibre end at the front face of the calorimeter. In these tests, a single optical fibre connected to a UV LED light source was used to inject light of fixed amplitude at varying positions along the fibre. Tests were made with and without mirroring applied to the polished fibre end and transmitted light was recorded with an Avalanche Photo Diode (APD) photosensor as a function of position of the light injection point. Typical results are shown in Fig. 2.7. In this figure, the APD sits at zero distance and the front face of the calorimeter, in a full detector assembly, would sit at the



distance of approximately 33 cm. The lower curve shows the light transmission efficiency in arbitrary units as a function of distance from the APD for a fibre without mirrored end. The upper curve shows the effect of including mirroring on the fibre end. The response is considerably flatter with an overall increase in efficiency in the range of about 25% in the vicinity of shower maximum (i.e. the location of the highest energy deposition for an electromagnetic shower). Shower maximum occurs at about 26 cm on the distance scale of Fig. 2.7. This number accounts for material immediately in front of the detector; which ranges between 0.4 and 0.8 radiation lengths, and assumes 5.5 - 6.0 radiation lengths for shower maximum for 10 GeV photons. At this depth in the detector, the mirrored fibre response is very uniform and contributes nothing significant to the non-linearity of the detector as a whole.

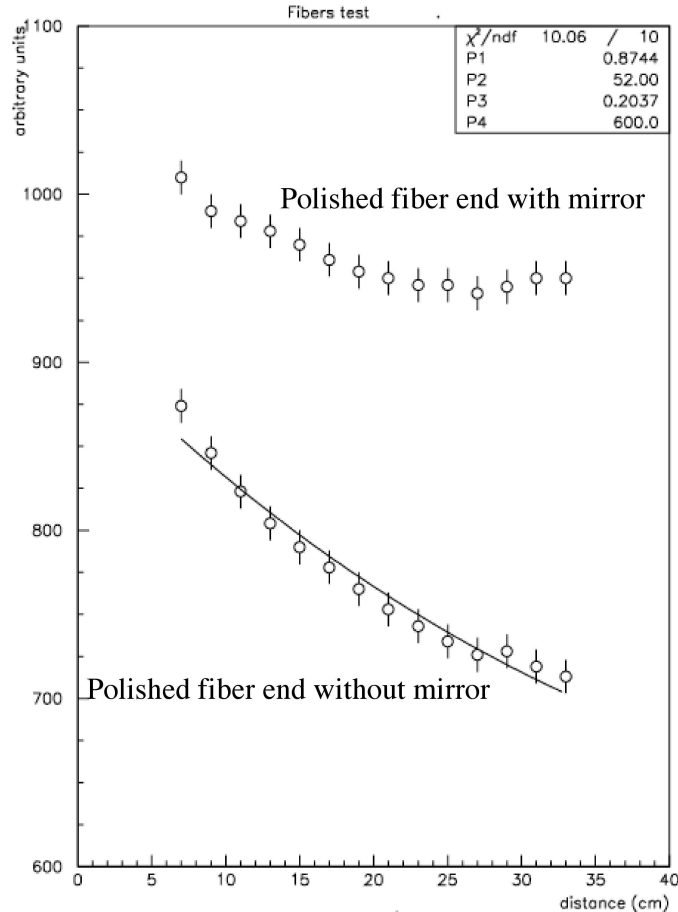


**Figure 2.7:** Comparison of light transmission efficiency versus distance of propagation for Kuraray Y-11 fibres with and without aluminized mirrored ends.

Other factors which can significantly impact the electromagnetic performance of the calorimeter, include scintillator edge treatment and the density of the wavelength shifting fibre readout pattern and the material chosen for the interlayer diffuse reflector. For scintillator edge treatment and fibre density, we were able to take advantage of the extensive studies made by the LHCb collaboration for their ECAL [3]. Given that we use the same scintillator with virtually identical towers size to the LHCb "middle modules", we were able to adopt their procedures for scintillator edge treatment and fibre density after a series of relatively simple checks. In particular, we have adopted a diffuse reflector edge treatment such as that obtained with Bicon Titanium Dioxide loaded white paint (BC622A) and a total fibre density of about one fibre per  $\text{cm}^2$ . In the case of the interlayer diffuse reflector, we have to deviate from LHCb and use a white, acid free, bond paper in place of the Teflon based commercial TYVEK. While TYVEK produces slightly better surface reflectivity, its coefficient of friction is too low to permit its use in this design where the module's mechanical stability depends somewhat on the interlayer friction. The white

paper used in the EMCal prototypes has been previously studied for aging effects in connection with the STAR calorimeter project [4].

**Table 2.2:** Characteristics of the selected wavelength shifting fibres.

| Quantity                      | Value           |
|-------------------------------|-----------------|
| WLS Fibre                     | Y-11 (200) M-DC |
| Manufacturer                  | Kuraray         |
| WLS Fluor                     | K27 200 mg      |
| Absorbtion Peak               | 430 nm          |
| Emission Peak                 | 476 nm          |
| Decay Time                    | 7 ns            |
| Core material                 | PS              |
| Refractive Index              | 1.59            |
| Inner Cladding                | PMMA            |
| Refractive Index              | 1.49            |
| Outer Cladding                | FP              |
| Refractive Index              | 1.42            |
| Long Fibre Attenuation Length | 3.5 m           |
| Fibre Diameter                | 1.0 mm          |

The 6.8 mm diameter fibre bundle from a given tower connects to the APD through a short light guide/diffuser with a square cross section of 7 mm  $\times$  7 mm that tapers slowly down to 4.5 mm  $\times$  4.5 mm as it mates (glued) to the 5 mm  $\times$  5 mm active area of the photo sensor.

Fig. 2.8 shows 4 pre-fabricated fibre bundles inserted into the towers of a single prototype module. In this picture all of the module rear enclosing and structural elements are omitted so the convergence of the wavelength shifting fibres may be seen as they converge to the light guide (inside the black plastic tube) and finally to mate with the APD and charge sensitive preamplifier. The APD and preamplifier are discussed at length in Section 3. Here we will mention briefly their optical characteristics. The selected photo sensor is the Hamamatsu S8664-55 Avalanche Photo Diode. This photodiode has a peak spectral response at a wavelength of 585 nm compared to an emission peak of 476 nm for the Y-11 fibres. However, both the spectral response and the quantum efficiency of the APD are quite broad with the latter dropping from the maximum by only  $\sim 5\%$  at the WLS fibre emission peak. At this wavelength, the manufacturer's specification gives a quantum efficiency of 80%.

### 2.3 Module Integration to Strip Modules and Super Modules

As described above, the super module is the basic building block of the calorimeter. Starting with 288 individual modules which are rather compact and heavy, the main engineering task is to create a super module structure which is rigid, with small deflections in any orientation yet does not require extensive, heavy external stiffening components that would reduce the volume available for the active detector. The solution adopted for the ALICE EMCal is to develop a super module "crate" which functions not as a box for the individual modules but rather an integrated structure in which the individual elements contribute to the overall stiffness. The super module crate is effectively a large I-beam in which the flanges are the long sides of the crate and the 24 rows of strip modules together form the web. This configuration gives to the super module good stiffness for both the 9 o'clock and 10 o'clock locations. For the 12 o'clock location, the I-beam structure of the super module is augmented by a 1 mm thick stainless steel forward sheet (traction loaded), which controls the bending moment tending to "open" the crate main sides, and helps to limit deflection of strip modules.





**Figure 2.8:** Fibre bundles with attached APD and preamplifier of four towers of an EMCal module.

The super module crate concept is illustrated in Figs. 2.9 and 2.10. For the purpose of clarity in these illustrations, only 6 of the 24 strip modules are included. Ridges are provided on the interior surfaces of the crate to allow precision alignment of the strip modules at the correct angle.

The stiffness given by this I-beam concept allows the use of non-magnetic light alloys for main parts of the super module crate. Unlike austenitic stainless steels, light alloys are easy to machine, helping to limit both cost and weight. Parts of the super module crate will be made mainly from laminated 2024 aluminum alloy plates. The two main sides (flanges of the I-beam) of the crate will be assembled from 2 plates, 25 mm and 25 mm thick, bolted together and arranged so as to approximately follow the taper of the 20 degree sector boundary.

Each of the 24 rows of a super module contain 12 modules as described in Section 2.4. Each of the modules is attached to a transverse beam by 3–4 mm diameter stainless steel screws. The 12 modules and the transverse beam form a strip module.

The strip module is roughly 1440 mm long, 120 mm wide, 410 mm thick. The total weight of the strip module is approximately 300 kg and like module, it is a self supporting unit. The transverse beam, which is the structural part of the strip module, is made from cast aluminum alloy with individual cavities along its length where the fibres emerging from towers are allowed to converge. The casting process is well suited to forming these cavities and the overall structure, saving considerable raw material and machining time. Fig. 2.11 shows the overall layout and dimensions of a strip module.

In addition to functioning as a convenient structural unit which offers no interference with the active volume of the detector and forming the web of the I-beam structure of the super module, the transverse beam of the strip module provides protection for the fibres, a structural mount for the light guide, APD and charge sensitive preamplifier and a light tight enclosure for these elements.

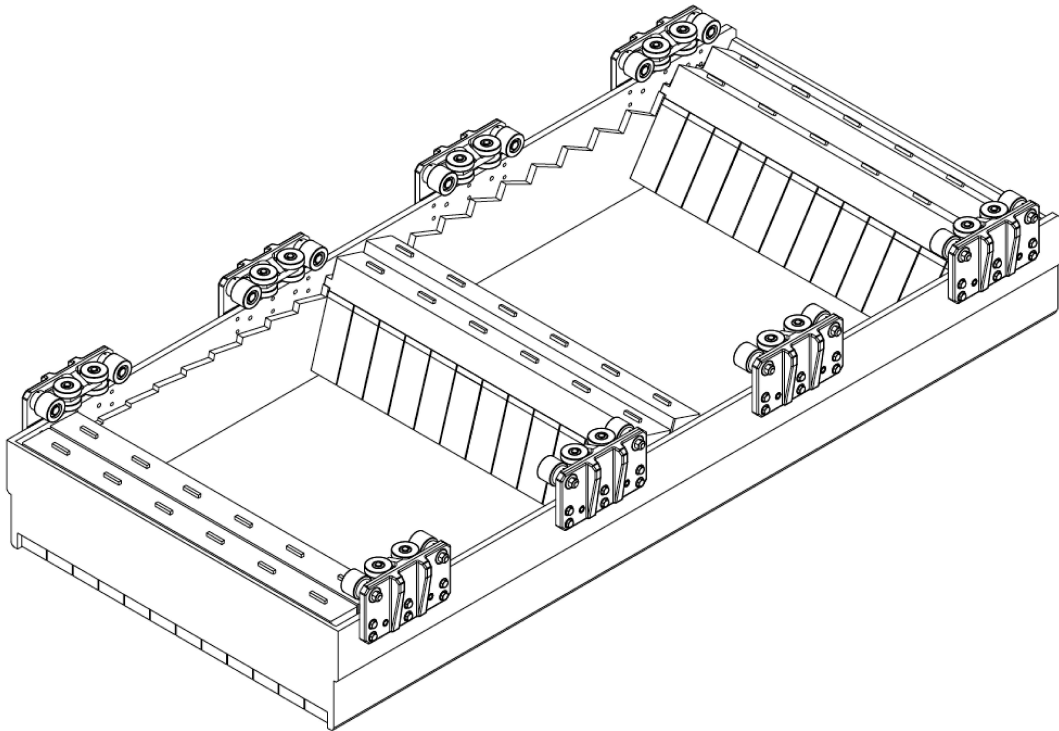


**Figure 2.9:** Conceptual layout of the super module crate. Only six of the 24 strip modules are inserted in this figure for clarity - two near the zero rapidity end, two near the center and two near the high rapidity end.

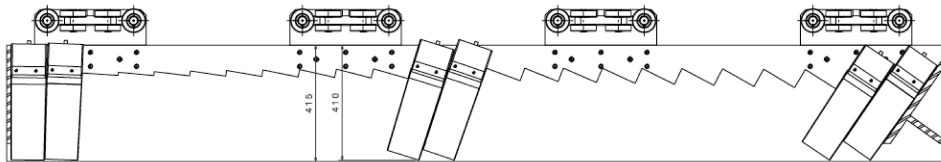


**Figure 2.10:** A side view of the super module crate showing the function of the ridges used to align the strip modules. Only six strip modules are shown here for clarity.

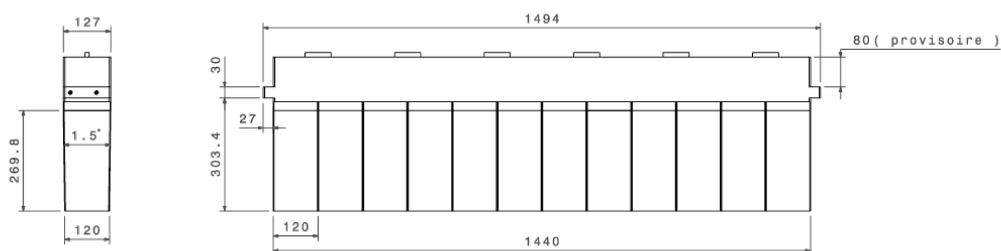


**Figure 2.11:** Strip module layout showing dimensions and the 1.5 degree taper.

## 2.4 Mechanical Analysis

Analysis of the strip modules and super modules was performed with the CATIA application for 3D modeling and Samcef Field for Finite Element analysis (FEA). All calculations were performed for a

super module mass of approximately 9950 kg. This super module mass results in a total weight for the EMCAL detector of 110 tons and corresponds to a detector with an active depth of 22 radiation lengths. This total weight is close to the upper limit still providing a sufficient safety factor for support surfaces in the ALICE magnet. The detector considered in this proposal actually has an active depth of 20 radiation lengths and has approximately 10% less mass than the detector modeled in the analysis. This 10% may be viewed as an extra safety factor or may be regarded as a margin to permit some increase in the active detector depth should future simulations of physics performance suggest that this is required.

#### **2.4.1 Super Module Crate**

FEA calculations show, for a load of 100 kN, a maximum stress of roughly 20 Mpa at 12 o'clock location and 120 Mpa at 9 o'clock location. These points of maximum stresses occur close to the super module mounting points at the carriages (Figs. 2.9 and 2.10). This level of stress is acceptable for the 2024 aluminum alloy which performs to a 290 Mpa yield strength. The crate features a deformation of 0.8–1.0 mm at the 9 o'clock location.

#### **2.4.2 Strip Module**

Calculations show that the cast strip module will have a maximum stress less than 15 Mpa while 42000 cast aluminum alloy performs to a yield strength of 180 Mpa. The maximum deflection of a strip module is foreseen at 0.7–0.9 mm, for the 12 o'clock location.



### 3 Electronics

Since the light yield per unit of energy deposit in the EMCal is similar to that of the PHOS [1, 2] (PHoton Spectrometer) detector of ALICE, and since the electronic noise performance requirements of the EMCal are less stringent than those of PHOS due to the larger intrinsic energy resolution of the EMCal, the PHOS readout electronics have been adopted for the EMCal readout, with only minor modification. The PHOS electronics readout is summarized in the next section and differences with the PHOS FEE are described in Section 3.2.

#### 3.1 Overall Electronics Architecture

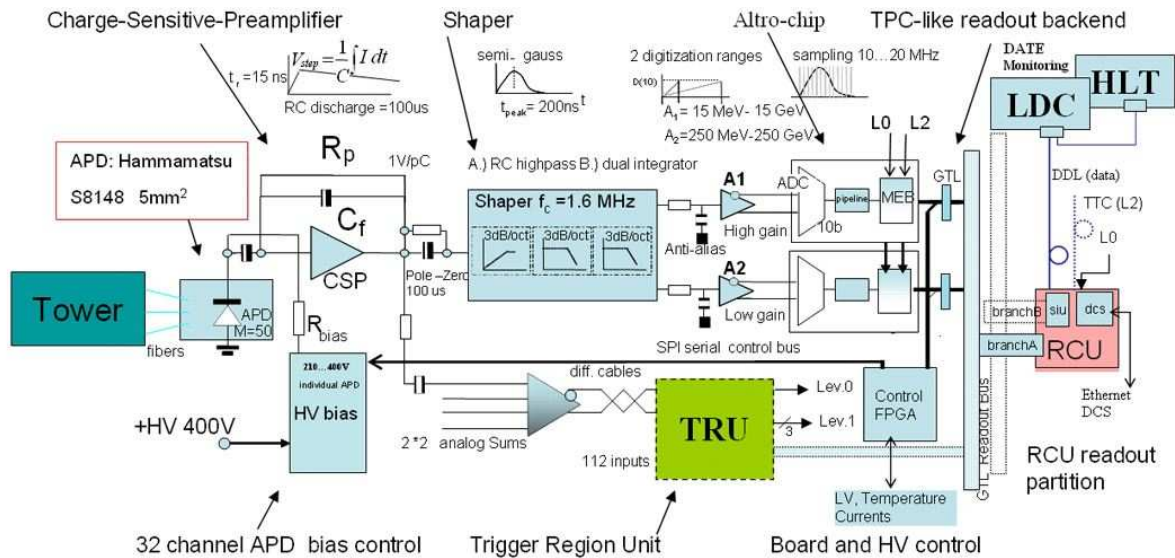


**Figure 3.1:** EMCal Readout electronics overview.

The PHOS is a highly granular  $\text{PbWO}_4$  calorimeter comprising 17920 crystals when fully implemented in 5 groups of 3584 crystals. The crystals are kept in a cold zone at  $-25^\circ\text{C}$  and separated by an isolation layer from a warm volume immediately behind (radially) the crystals that encloses the electronics. A schematic overview of the PHOS Front End Electronics (FEE) [3] as used for the EMCal is shown in Fig. 3.1. The interface of the FEE with the ALICE Data Acquisition and with the Trigger and High-Level Trigger are described in further detail in Section 4.

##### 3.1.1 APD and Preamplifier

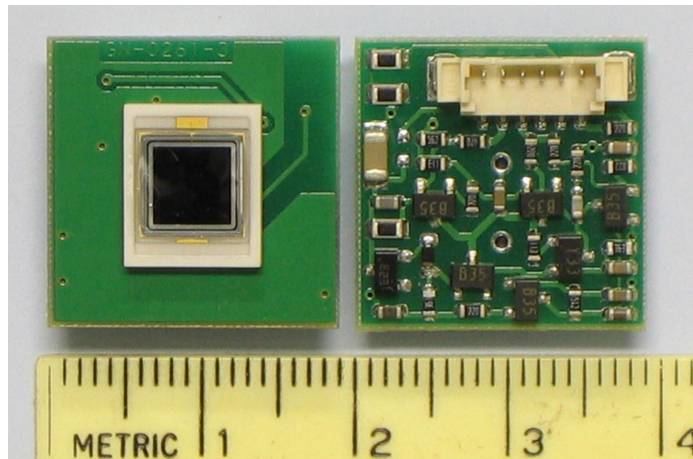
A  $5 \times 5 \text{ mm}^2$  active area Avalanche Photo Diode (APD S8148) is glued to each PHOS crystal. This APD was the result of a large R&D activity carried out by the CMS collaboration and Hamamatsu Photonics to arrive at the development of the APD S8664-55 (or S8148) [4, 5]. This is a large area Avalanche PhotoDiode with high quantum efficiency, low dark current and very good stability and reliability. The main characteristics of this detector are listed in Table 3.1. In particular extensive studies have been done to insure the radiation hardness of this device [6].

The APD is connected directly to the back of a Charge Sensitive Preamplifier (CSP) with about 1 V/pC sensitivity and a maximum range of about 5 pC. The APD and CSP are shown in Fig. 3.2. The

**Table 3.1:** Characteristics of the S8664-55 (S18148) Avalanche PhotoDiode.

|                           |                           |
|---------------------------|---------------------------|
| Active Area               | $5 \times 5 \text{ mm}^2$ |
| Capacitance               | 90 pF                     |
| Wavelength min.           | $\sim 320 \text{ nm}$     |
| Wavelength max.           | $\sim 1000 \text{ nm}$    |
| Peak wavelength           | 600 nm                    |
| Quantum efficiency        | $\sim 80\%$ at 476 nm     |
| $1/M \times dM/dT$ (M=50) | $\sim 2.2\%$              |
| $1/M \times dM/dV$ (M=50) | $\sim 3.3\%$              |

APDs are operated at moderate gain for low noise and high gain stability in order to maximize energy and timing resolution. With a nominal APD gain of  $M=50$ , about 220 electrons are generated in the APD per MeV of energy deposited by showering electromagnetic particles ( $4.4e^-/\text{MeV}$  at  $M=1$ ).

**Figure 3.2:** The Avalanche PhotoDiode (left) mounted on the back of the Charge Sensitive Preamplifier (right) used by PHOS and EMCAL.

### 3.1.2 Front End Card: Shaper and Digitization

The CSP converts the charge signal over a 1 pF capacitor into a voltage step that is formed by the CR-2RC shaper of the FEE into a semi-Gaussian pulse-shape. The FEE cards contain 32 remotely controlled precision High Voltage (HV) bias regulators [7], 64 shapers and digitizers, a board controller, a USB processor, and a power regulation system which prevents noise coupling between digital or High Voltage sections and the analogue signal section. The APD bias voltages can be set individually to a precision of 0.2 Volt/bit. Each shaper channel is split via a low noise gain buffer into high and low gain shapers for a total dynamic range of 14 bits using two 10-bit digitizers. Four ALTRO (ALICE TPC ReadOut) [8] digitizer chips are required, each containing 16 10-bit flash ADCs and internal multi-event-buffers, for a total of 32 high-gain and 32 low-gain channels per FEE card. The choice of the ALTRO chip, combined with a board controller FPGA, allows the PHOS and EMCAL to re-use the readout backend protocol of the ALICE TPC via an external Readout Control Unit (RCU) [9].

The FEE has an effective 14-bit dynamic range over the interval 5 MeV to 100 GeV for the PHOS, which has a measured energy resolution of 2% at 2 GeV. The ADC samples the waveform at 10 MHz (programmable). An additional design goal for PHOS was timing resolution of about 1 ns at 2 GeV in order to reject low energy neutrons and anti-neutrons. The competing requirements of low noise (narrow

bandpass) and good timing resolution (wide bandpass) have necessitated extensive tests of alternative PHOS shaper designs, with shaping times varying between 1 and 4  $\mu$ s. As discussed below, the EMCal requirements dictate a shorter shaping time of about 100 ns. These shaping time modifications only require changes in discrete component values of the shaper and do not affect the layout of the FEE board.

### 3.1.3 Trigger Input

Each 32 channel FEE card forms 8 analogue charge sums of  $2 \times 2$  adjacent towers to provide fast Level-0 and deadtime-less Level-1 photon shower triggers. The fast-OR signals are extracted from the input of the shaper, passed through a simple 100 ns RC-shaper, and sent via short differential cables of equal length to the Trigger Region Unit cards (TRU) [10]. One TRU card receives 112 (PHOS) or 96 (EMCal) analogue sums from the 14 (PHOS) or 12 (EMCal) FEE cards on its common GTL bus (TRU domain). The TRU digitizes the sums using an ALTRO chip and inputs the full space and time image of all channels it accesses into a single FPGA. The FPGA trigger algorithm applies  $4 \times 4$  sliding window algorithms for successive Level-0 and Level-1 trigger generation, with programmable thresholds for simultaneous low, mid, and high energy trigger outputs at a decision rate of 40 MHz.

### 3.1.4 Readout and Control

Each TRU domain (384 towers for EMCal) is read out by a custom 200 MByte/s GTL+ bus under mastership of an external RCU card. Each external RCU card masters up to two TRU domains via a separate custom GTL bus and transmits the FEE data to the Local Data Concentrator of the DAQ via an ALICE-standard Detector Data Link (DDL) [11].

Control and monitoring access to the FEE card resources is implemented in programmable firmware logic on the FEE cards. This slave logic allows RCU address-mapped access to both the control and data sections of the FEE cards. The address space includes ALTRO-chip internal registers, APD bias control registers, and registers for voltages, currents, and temperatures. A USB port allows an external USB master (such as a PC) to emulate the RCU for production testing, local servicing, and for updating of the Flash Prom.

### 3.1.5 Mechanical

Mechanically, the PHOS is built up of  $1 \times 8$  rows of crystals called a PHOS strip-unit. Each strip-unit connects to a Transition printed circuit card or T-card that connects via a short 37-pin flat ribbon cable to an Intermediate Printed Circuit Board (IPCB). A pair of IPCBs (upper and lower) form the backbone of the FEE crate structure. Each FEE card connects to a connector on the upper and on the lower IPCB with two strip unit ribbon cables attached to the IPCB and routed to one FEE input connector. Thus a single FEE, and associated trigger sums, are configured to readout a group of 2 by 16 PHOS crystals. The associated TRU region then corresponds to a group of 28 by 16 PHOS crystals. Essential functions of the T-card and IPCB card are to multiplex the LV, HV bias, and signal lines between the FEE output and the individual preamplifier connections.

The power dissipation per channel of embeded FEE/TRU electronics is 380 mW/channel. The preamplifier power dissipation is 53mW per channel.

The first prototypes of the PHOS FEE electronics (version 1.0) were produced in fall 2004 with second prototypes (version 1.1) produced in spring 2005. A photograph of the FEE card is shown in Fig. 3.3. The production of 130 PHOS FEE cards (sufficient to read out one PHOS module of 3584 crystals) occurred in December 2005.



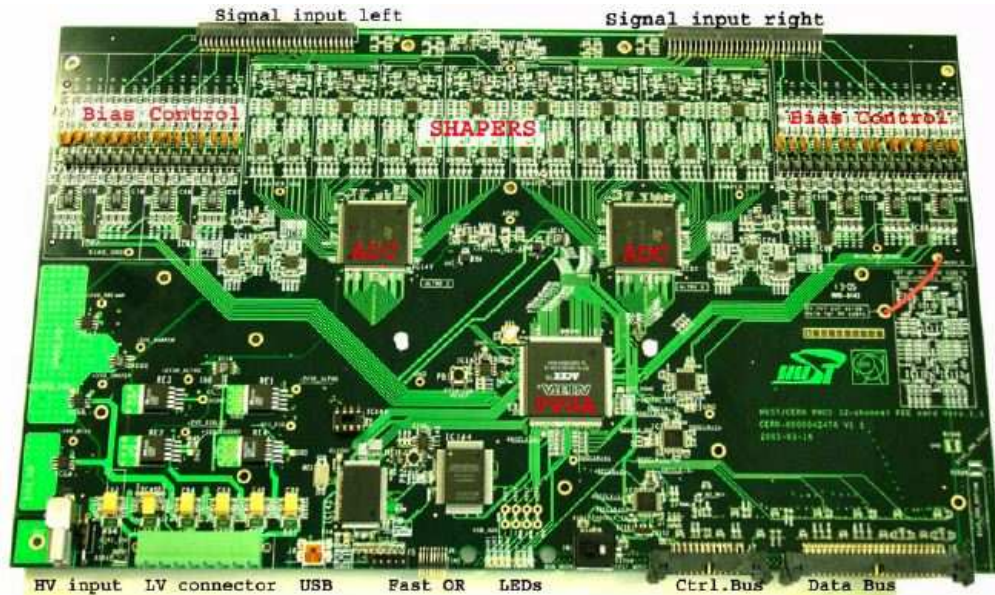


**Figure 3.3:** Photograph of the 32 channel PHOS/EMCal FEE card.

## 3.2 EMCal Specific Readout Considerations

### 3.2.1 APD and Preamplifier

The PHOS decision to use the Hamamatsu S8664-55 APD was made largely because, at the time, it was essentially the only commercially available large area APD. It was developed by Hamamatsu in collaboration with the CMS experiment. While a number of new APD products are now commercially available, and some of these products might be suitable replacements for the Hamamatsu S8664-55 APD, there is no expected performance benefit for the EMCal due to the dominance of the intrinsic resolution contribution, and potential cost savings would most likely be offset by the need to develop a new preamplifier and/or bias control in the case that the required bias exceeded the 400 V maximum of the PHOS FEE. For these reasons it has been decided to use the same APD and preamplifier as used by PHOS (see Fig. 3.2).

The only significant difference with the PHOS readout then is the difference in the FEE amplifier due to the chosen dynamic range, the EMCal light yield, and the amplifier shaping time.

### 3.2.2 Dynamic Range

Based on the expected annual yield of photons and  $\pi^0$  at high  $p_t$  (Fig. 1.4 of Section 1), the full scale energy range for an EMCal tower is chosen to be 250 GeV as compared to 80 GeV for PHOS, well beyond the expected maximum photon or  $\pi^0$  energy. Setting the EMCal full-scale energy range to 250 GeV sets the Least Significant Bit (LSB) on the low gain range to 250 MeV (10-bits) with the corresponding maximum energy on the high gain range at 16 GeV ( $\times 16$ ) and least significant bit at 16 MeV.

### 3.2.3 Light Yield

Another important parameter of the EMCal readout is the light output to the APD per MeV of energy deposit in a tower. The PHOS produces 4.4 photo-electrons/MeV from the APD with gain  $M=1$ . The initial estimate for the EMCal from measurements with early prototype lead/scintillator assemblies with photomultiplier readout using cosmic ray muons gave a initial estimate of 2.5 photo-electrons/MeV for APD readout at gain  $M=1$ . The shaper gains discussed below and used in the test beam measurements



were based on this result and the assumption of an operational APD gain of  $M=50$ . As discussed in Section 6, initial analysis of the test beam results indicates an EMCal light yield of 4.4 photo-electrons/MeV, i.e. the same as PHOS.

### 3.2.4 Shaper Time Constant Optimization

A substantial effort was made for PHOS to investigate alternative shaper designs and shaping times. In the case of PHOS, a primary consideration is optimum performance for measurement of low energy photons, in the region around 1 GeV, of interest for observation of thermal photon radiation from Quark Gluon Plasma. With the good intrinsic resolution of  $\text{PbWO}_4$ , care must be taken to minimize the electronics contribution to the noise. This can be done by a judicious choice of the shaping time of the amplifier.

A general noise model of an amplifier reflects all noise sources to the input and represents them in an equivalent representation as Equivalent Noise Charge (ENC) which includes both the amplifier and the detector noise. There are in general 4 noise components:

- Current (or Parallel) noise: Shottky ( $2qI_D$ ) + Shunt resistor thermal + equivalent input current
- Voltage (or Series) noise:  $4kTR_S$  thermal + Johnson noise at amplifier input
- $1/f$  noise
- Pileup noise (negligible for EMCal).

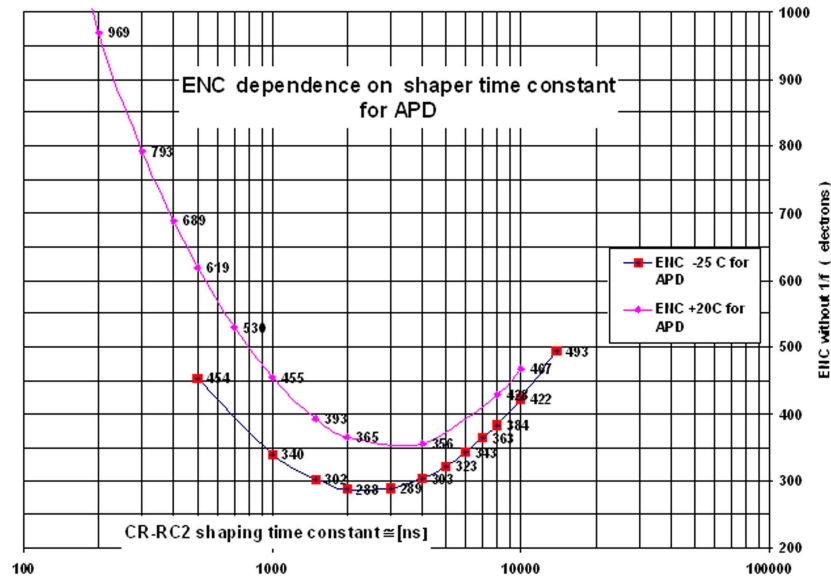


**Figure 3.4:** Electronic noise as a function of shaping time for PHOS at  $-25^\circ\text{C}$  and EMCal at  $+20^\circ\text{C}$ .

The noise performance of the APD+preamplifier is shown in Fig. 3.4 [3]. These results are for a detector capacitance of  $C_D = C_{APD} + C_{in} = 90 + 10 = 100$  pF as for the Hamamatsu S8664-55 APD. These results indicated an electronic noise minimum of about  $300e^-$  for a shaping time of about  $2 \mu\text{s}$ . The competing consideration of a reasonably good timing measurement motivated a final choice of  $1 \mu\text{s}$  shaping time for PHOS.

Several considerations motivate a much shorter shaping time for the EMCal. First, simulations of central Pb–Pb collisions with HIJING+AliRoot [13] (the ALICE implementation in GEANT3) indicate

that the EMCal will be affected by a large slow neutron contribution that has a tail extending for hundreds of ns after the collision. Second, the number of ALTRO samples recorded is dictated by the total shaped pulse width. With the approximately ten times coarser EMCal granularity, the occupancies will be correspondingly higher in EMCal than PHOS. With the goal to keep the total data volume per RCU similar to PHOS the number of EMCal samples should be reduced to keep the product of (occupancy) $\times$ (No. samples) similar. This would argue for a shaping time of about 100 ns. With 100 ns shaping time the voltage noise would dominate such that one would expect a total electronics noise contribution of about  $1500 e^-$  for the PHOS APD+preamplifier+shaper with 100 ns shaper time. This would correspond to an electronics noise contribution of about 12 MeV per EMCal tower. Due to the larger intrinsic energy resolution term of EMCal compared to PHOS (8.5% vs 3.6%) the importance of the electronics noise contribution is much less significant.

### 3.2.5 Late Neutron Background

Simulations of the EMCal response for central Pb–Pb collisions with HIJING+AliRoot have shown that there is a large background energy deposit predominantly from late neutrons produced in secondary interactions in the surrounding materials of the ALICE experiment [12]. The muon absorber is one of the major sources of this background. As shown in Fig. 3.5 the background has a long tail with arrival times extending for several hundreds of ns after the collision. (Note that this background is generated by the primary central Pb–Pb collision, and hence it is a centrality dependent effect, expected to scale with the multiplicity of produced particles). The result indicates that as short a shaping time as feasible should be used in order to minimize this background contribution to the energy measurement. Without any timing cut, the average background energy deposit is 36 MeV per tower, i.e. several times greater than the expected electronics noise contribution per tower with 100 ns shaping time.

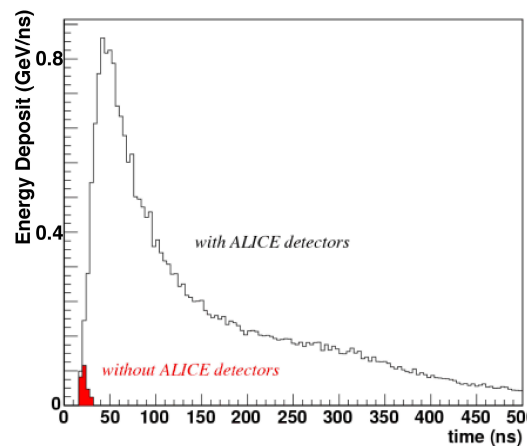


**Figure 3.5:** Rate of total energy deposit in the EMCal vs arrival time for central Pb–Pb collisions. Results are shown for arrival times greater than 30 ns with and without the other ALICE detectors. The background energy deposit is primarily from late neutron hits and comprises about a third of the total energy deposit.

### 3.2.6 EMCal Energy Resolution Contributions

The relative contributions to the total EMCal energy resolution are shown in Fig. 3.6. The assumptions have been discussed above and relevant parameters are compared to PHOS and summarized in Table 3.2. The intrinsic energy resolution has been assumed to be  $6.9\%/\sqrt{E} \oplus 1.4\%$ , based on GEANT3 simulations for the production module (see Section 2.2.1). The digitization resolution has been assumed to be determined by a maximum energy scale set to 250 GeV with 10-bits of digitization resolution and dual

gain ranges separated by a factor of 16. The constant energy contribution due to calibration errors has been assumed to be 1%. Finally, the electronics noise contribution has been conservatively assumed to be  $\sigma_{ENC} = 2000 e^-$  for an integration time of 100 ns (see Fig. 3.4). With a light yield of  $4.4 e^-/\text{MeV}$ , a gain of 30, and  $3 \times 3$  modules included in the energy sum, this corresponds to an electronics noise contribution to the resolution of  $c = 48 \text{ MeV}/E$  (Eq. 2.1). This contribution (dotted curve) is seen to be negligible compared to the intrinsic noise contribution (solid dark curve) except at photon energies much below 1 GeV. Note that the relative electronic noise contribution would be even smaller assuming  $4.4 e^-/\text{MeV}$ , as obtained from the test beam measurements (see Section 6), at an APD gain of  $M=50$ .

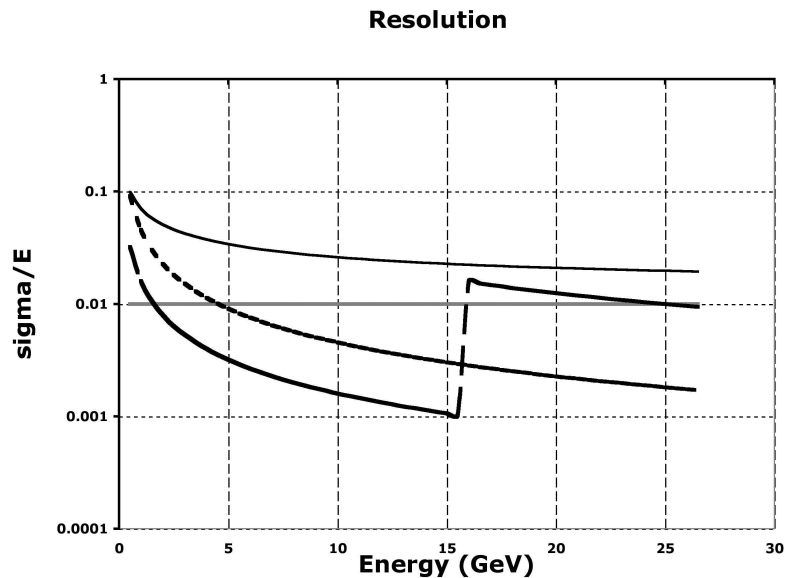


**Figure 3.6:** Contributions to the total EMCAL photon energy resolution.

### 3.3 The FEE Shaper

As discussed above, the only modification to the FEE used by PHOS for application to the EMCAL readout is to modify the shaper to use a shorter shaping time. The CERN-Wuhan (CW) shaper, developed jointly by CERN and Wuhan, implemented on the FEE card, is shown schematically in Fig. 3.7. The shaper gain for each gain range is chosen such that the maximum CSP voltage (for the chosen APD gain) gives the fullscale input voltage of the ALTRO ADC chip of 1 Volt maximum input (=1024 bit). Based on a nominal light yield of  $4.4e^-/\text{MeV}$  obtained with the PHOS crystals and an APD gain of 50 the following two gain ranges and gain values were implemented for PHOS:

High gain: 5 MeV– 5.12 GeV:  $V_{CSP} = 1.37 \text{ mV} - 0.141 \text{ V}$ : Shaper gain = 7.2

Low gain: 80 MeV – 81.92 GeV:  $V_{CSP} = 2.19 \text{ mV} - 2.245 \text{ V}$ : Shaper gain = 0.45

The CW shaper was developed for optimal noise performance with successive RC differentiator and dual Bessel integrator stages of common cutoff frequency and with gain ratio of 16 for low-energy and high-energy ranges. The RC differentiator is combined with a pole-zero cancellation, tuned for the CSP. The output stage to the ALTRO ADC is fully symmetrical and contains a high frequency RC noise filter.

Table 3.3 shows the results obtained with the Bessel calculation described in detail in Ref. [3] for the CW shaper RC components of  $1 \mu\text{s}$  (PHOS) and 100 ns (EMCAL) shaping times and gain ratio 1/16.  $R_Z$  has been determined empirically as the best non-overshoot value of the pole zero cancellation. For

**Table 3.2:** Summary of PHOS and EMCal readout parameters.

| Quantity   | PHOS  | EMCal   |
|--|---|---|
| Digitization Ranges<br>x16 and x1 ranges<br>10-bits      | High Gain: 5 MeV – 5 GeV<br>Low Gain: 80 MeV – 80 GeV<br>LSB=5 MeV                      | High Gain: 16 MeV – 16 GeV<br>Low Gain: 250 MeV – 250 GeV<br>LSB=16 MeV                 |
| Light Yield  | $4.4e^-/\text{MeV}$ at M=1<br>$220e^-/\text{MeV}$ at M=50                               | $4.4e^-/\text{MeV}$ at M=1<br>$125e^-/\text{MeV}$ at M=30                               |
| Channel rate at $E > 30$ MeV                             | $\sim 200$ Hz   | $\sim 2$ kHz  |
| APD  | Hamamatsu S8664-55<br>$5 \times 5$ mm <sup>2</sup> , $C_{APD} = 90$ pF                  | Hamamatsu S8664-55<br>$5 \times 5$ mm <sup>2</sup> , $C_{APD} = 90$ pF                  |
| Charge Sensitive Preamp                                  | JFET:2SK932<br>$C_{input} = 10$ pF<br>$0.78\text{mV/fC}$ or $0.128\mu\text{V}/e^-$      | JFET:2SK932<br>$C_{input} = 10$ pF<br>$0.78\text{mV/fC}$ or $0.128\mu\text{V}/e^-$      |
| CSP Output range   | $0.147\text{mV} - 2.348\text{V}$<br>(5 MeV – 80 GeV)                                    | $0.261\text{mV} - 4.169\text{V}$<br>(16 MeV – 250 GeV)                                  |
| ENC  | $730e^-$ (3.3 MeV)  | $\sim 1500e^-$ (12 MeV)   |
| Shaper   | CR-2RC type; Semi-Gauss<br>$\tau_{int} = 1 \mu\text{s}$ ; $\tau_{peak} = 2 \mu\text{s}$ | CR-2RC type; Semi-Gauss<br>$\tau_{int} = 100$ ns; $\tau_{peak} = 200$ ns                |
| Trigger signal shaping                                   | FWHM=100 ns   | FWHM=100 ns   |
| ADC  | ALTRO-16ST; 10-bit<br>LSB <sub>noise</sub> < 0.5 mV                                     | ALTRO-16ST; 10-bit<br>LSB <sub>noise</sub> < 0.5 mV                                     |
| Sampling Rate: $1/\Delta t$                              | 10MHz; 15 presamples  | 10MHz; 15 presamples  |
| Max.Nr. Samples/signal<br>$5 \cdot \tau_{peak}/\Delta t$ | 100+15  | 10+15   |
| Data rate/Channel  | 58 kB/s<br>(=200Hz*2*(115 samples)*10-bits)   | =125 kB/s<br>(=2kHz*2*(25 samples)*10-bits)   |
| Power consumption  | 112 FEE*10W = 1.12kW<br>8 TRU*30W =0.24kW<br>Total 1.36kW/Module<br>(380mW/channel)     | 36 FEE*10W = 0.36kW<br>3 TRU*30W =0.09kW<br>Total 0.45kW/SuperModule<br>(390mW/channel) |

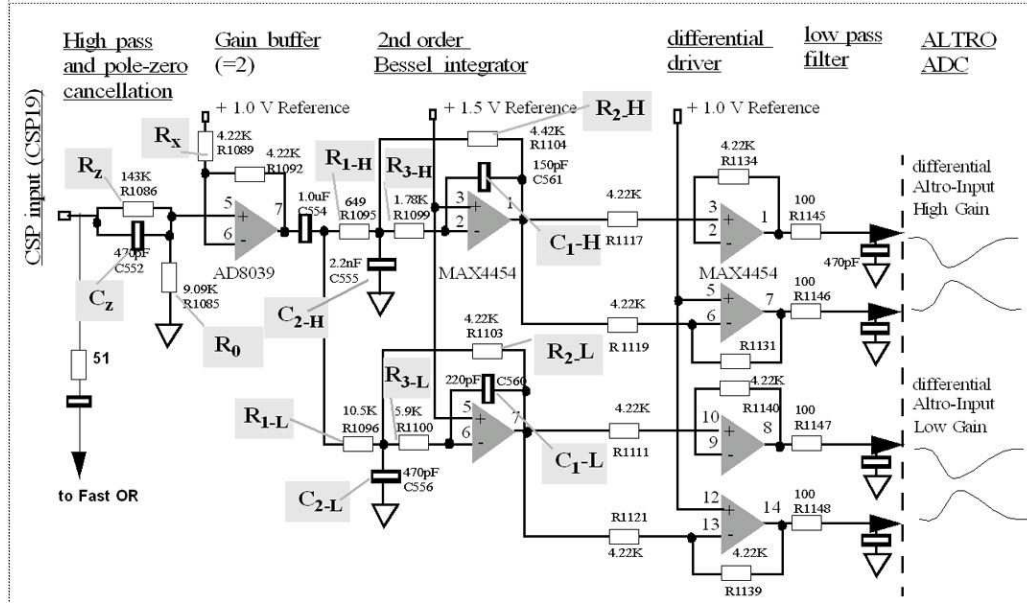


**Figure 3.7:** Schematic diagram of the shaper of the PHOS/EMCal FEE.

a change in the bandpass frequency (or shaping time) of the shaper,  $R_0$  must be adjusted to correspond with  $C_Z$  to the new bandpass value (i.e.  $\tau_{peak} = C_Z R$  where  $1/R = 1/R_Z + 1/R_0$ ). All other values  $R_1, R_2, R_3, C_1$ , and  $C_2$  can be calculated with the method described. The results for the  $1 \mu s$  shaping time were calculated for the desired PHOS maximum signal of 1 Volt to the ALTRO input for 2.348V maximum preamplifier signal output corresponding to a low range gain value of  $1/2.348=0.42$  ( $\times 16$  gain range gain = 6.81). The values for the 100 ns shaping time have been calculated for the 4V maximum preamplifier output for the EMCal (see Table 3.3) corresponding to gains of  $1V/4V = 0.25$  ( $\times 1$ ) and 4 ( $\times 16$ ) for the two gain ranges.

**Table 3.3:** RC values for the CERN-Wuhan shaper with  $2 \mu s$ , and 200 ns shaping times, peaking time  $\tau_{peak} = 2\tau_0$  (buffer gain = 2, gain ratio =16).

| $\tau_0$  | Gain             | $C_Z, R_Z$             | $R_0$           | $R_1$           | $R_2$           | $R_3$           | $C_1$  | $C_2$   |
|-----------|------------------|------------------------|-----------------|-----------------|-----------------|-----------------|--------|---------|
| $1 \mu s$ | $2 \times 3.35$  | 470 pF, 143 k $\Omega$ | 4.22 k $\Omega$ | 681 $\Omega$    | 4.87 k $\Omega$ | 1.96 k $\Omega$ | 68 pF  | 1000 pF |
| $1 \mu s$ | $2 \times 0.21$  | 470 pF, 143 k $\Omega$ | 4.22 k $\Omega$ | 4.02 k $\Omega$ | 1.69 k $\Omega$ | 5.36 k $\Omega$ | 150 pF | 470 pF  |
| 100 ns    | $2 \times 2.00$  | 470 pF, 143 k $\Omega$ | 213 $\Omega$    | 78.7 $\Omega$   | 316 $\Omega$    | 205 $\Omega$    | 100 pF | 1000 pF |
| 100 ns    | $2 \times 0.125$ | 470 pF, 143 k $\Omega$ | 213 $\Omega$    | 590 $\Omega$    | 147 $\Omega$    | 442 $\Omega$    | 220 pF | 470 pF  |

The test beam measurements with the EMCal prototypes in the meson test beam at FNAL, described below in Section 6, were performed with one FEE card with the  $1 \mu s$  shaping time intended for PHOS, and a second FEE card with 100 s shaping time as proposed for the EMCal.

### 3.4 Installation of EMCal Read Out

In the EMCal assembly four towers with APDs and preamplifiers are integrated into one mechanical-electronic EMCal unit, a so-called EMCal module. The ends of the fibre bundles, light guides, and APDs with preamplifiers are secured in a compact matrix unit on the back of the module. As part of the

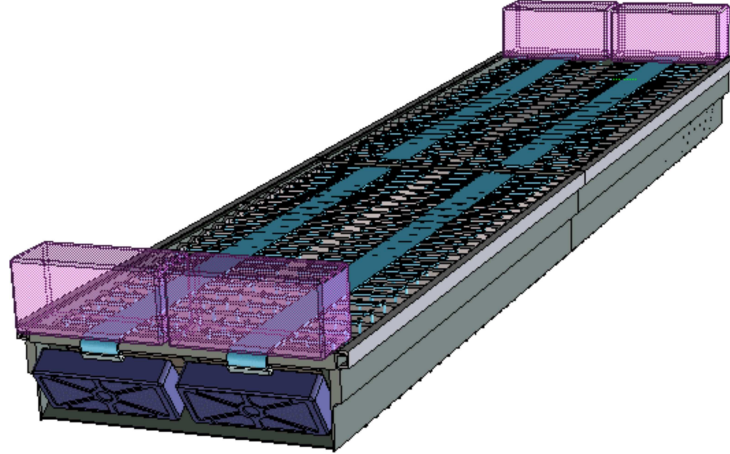


**Figure 3.8:** A pair of EMCAL super modules covering the full extent in Z. The readout cables (indicated by stripes) run across the back of the super module to the FEE crate volume indicated by the shaded boxes at the end of each super module.

construction of an EMCAL super module, 12 EMCAL modules will be assembled onto a support backbone to provide one strip module. Twenty-four strip modules are stacked together in Z to comprise a super module. An EMCAL transition card, located near to the tower APD+preamplifiers, will connect to a group of  $2 \times 4$  towers from a pair of modules adjacent in  $\phi$ . The T-card will be connected to the FEE via ribbon cable. The mapping of the EMCAL towers to FEE input channels will be accommodated on the IPCB to preserve the existing geometrical grouping of  $2 \times 2$  adjacent towers used to form the analogue trigger sum primitives in the FEE.

Owing to radial space restrictions for the EMCAL, it is not possible to locate the EMCAL FEE directly behind (radially) the EMCAL, as is the case for PHOS. Instead, the EMCAL FEE crates, with associated IPCB, GTL bus, and RCUs, will be located at the outer end (large Z) of each EMCAL super module, as shown in Fig. 3.7 for a pair of super modules. Each full super module will be read out by three FEE crates each containing 12 FEE cards and one TRU. Two RCUs will be used to readout the three FEE crates. Each FEE crate will read out a group of  $24 \times 16(\phi \times Z)$  EMCAL towers with each FEE card connected to  $2 \times 16(\phi \times Z)$  towers.

## 4 Data Acquisition and Online

---

### 4.1 Requirements

The ALICE experimental program incorporates a wide variety of running conditions: heavy-ion collisions, pp, pA, and lighter ion collisions. The heavy-ion run will last only a few weeks per year but this run will require the largest possible bandwidth to permanent storage. A large number of trigger classes will be used concurrently to select and characterize events relevant to studies of several physics topics. The rest of the running period will be used to acquire data produced by pp interactions which generate five times less data. The selection of events in the ALICE experiment is performed by two trigger systems. The Central Trigger Processor (CTP) [1] is hardware-based and is always present as it delivers the trigger levels 0, 1, and 2. The High-Level Trigger (HLT) [2] is software-based. Several running modes have been defined to permit its gradual activation. The ALICE Data Acquisition (DAQ) system is designed to be flexible enough to address this diversity of running conditions and of running modes.

The ALICE EMCAL readout uses the same components as the PHOS subsystem of ALICE and thus all needed parts of the readout chain have already been integrated into the ALICE data acquisition system.

### 4.2 DAQ Architecture Overview

The architecture of the ALICE Data Acquisition and its interface with the Trigger and the High-Level Trigger are illustrated in Fig. 4.1 and detailed in the ALICE Technical Design Report on Trigger, Data Acquisition, High-Level Trigger, and Control System [2].

The EMCAL detector receives the trigger signals and the associated information from the CTP, through a dedicated Local Trigger Unit (LTU) [3] interfaced to a Timing, Trigger and Control (TTC) system [4]. The Front End Read Out (FERO) electronics of the EMCAL is interfaced to the ALICE Detector Data Links (DDLs). The data produced by the EMCAL (event fragments) are injected into the DDLs using a common protocol.

At the receiving side of the DDLs there are PCI-based electronic modules, called DAQ Readout Receiver Cards (D-RORCs). The D-RORCs are hosted by the front-end machines (commodity PCs), called Local Data Concentrators (LDCs). Each LDC can handle one or more D-RORCs. The event fragments originated by the various D-RORCs are logically assembled into sub-events in the LDCs.

The CTP receives a busy signal from each detector. This signal can be generated either in the detector electronics or from all the D-RORCs of a detector. The CTP also receives a signal from the DAQ enabling or disabling the most common triggers. It is used to increase the acceptance of rare triggers by reducing the detector dead-time. This signal is function of the buffer occupancy in all the LDCs.

The role of the LDCs is to ship the sub-events to a farm of machines (also commodity PCs) called Global Data Collectors (GDCs), where the whole event is built (from all the sub-events pertaining to the same trigger). The GDCs also feed the Transient Data Storage (TDS) with the events that eventually end up in Permanent Data Storage (PDS). The PDS is managed by the CERN Advanced Storage Manager (CASTOR) [5].

All these hardware elements are driven and controlled by the Data Acquisition and Test Environment (DATE) software framework [6] developed by the ALICE DAQ project. The coherence of the whole system is ensured by this common software framework composed of different layers of modules. A bottom layer includes the memory handling, the process synchronization, and the communication modules. The

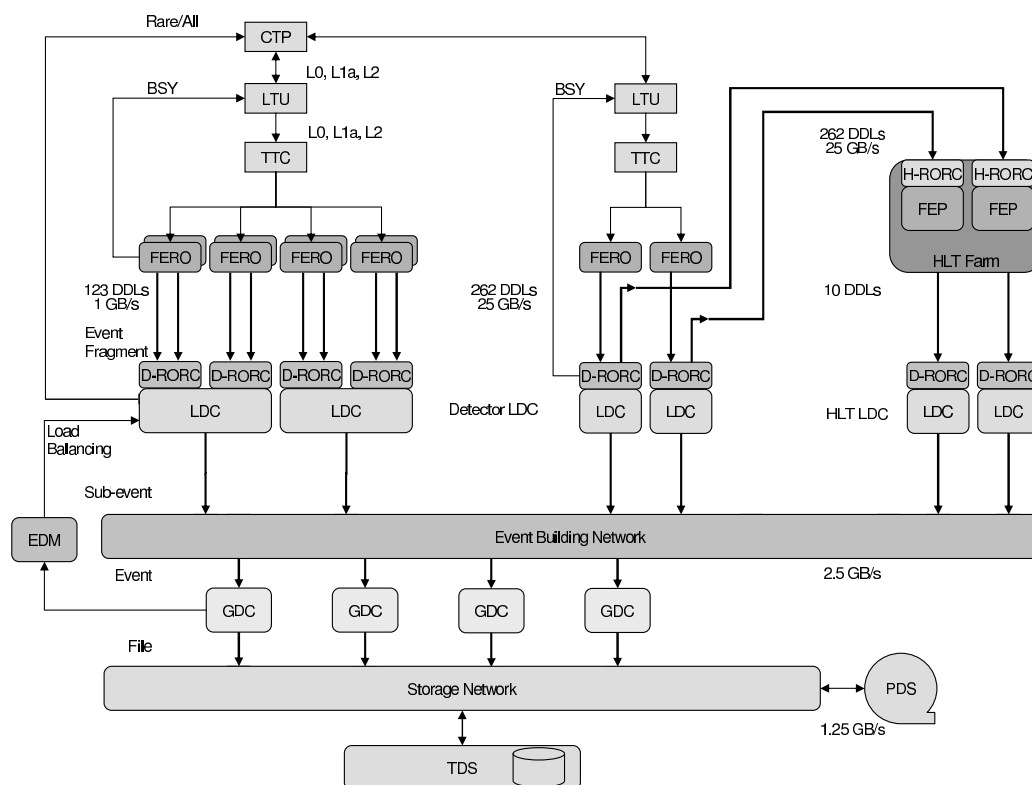


**Figure 4.1:** DAQ architecture overview.

application layer includes the data-flow applications (detector readout, event building, and data recording). DATE has been used for a number of years by many ALICE test beam users. The EMCal test beam measurements described below were realised using a completely integrated readout system with the DDL and the DATE software.

The HLT system receives a copy of all the raw data. The data and decisions generated by HLT are transferred to dedicated LDCs.

### 4.3 DAQ-HLT Interface

The overall architecture of the Trigger, DAQ and HLT systems is illustrated in Fig. 4.1. The DAQ system takes care of the data flow from the DDL up to the storage of data on the PDS system. The task of the HLT system is to select the most relevant data from the large input stream and to reduce the data volume by well over an order of magnitude in order to fit the available storage bandwidth, while preserving the physics information of interest. This is achieved by a combination of event selection (triggering), data compression, or selection of Regions of Interest with partial detector readout. While executing either of these tasks, the HLT may also generate data to be attached to or partially replacing the original event. Care has been taken not to impose any architectural constraints which could compromise the HLT filtering efficiency, knowing that event selection will become more and more elaborate during the experiment lifetime. This way, filtering may be introduced in progressively more sophisticated steps without affecting the performance and the stability of the Data-Acquisition system.

The DAQ-HLT interface is based on the DDL and its DIU/SIU cards, the same components used to transfer data from the detector electronics to the DAQ system. The choice of existing components as interface between the two systems minimized the need for new R&D and avoided the development of a new type of link. Past experience shows that at the experiment startup the DAQ and HLT problems are of different nature and essentially independent. There is no benefit from not keeping them so. Therefore,



the DAQ system is implemented within a coherent hardware and software framework, with the HLT system operating as an external system [7], as shown in Fig. 4.2

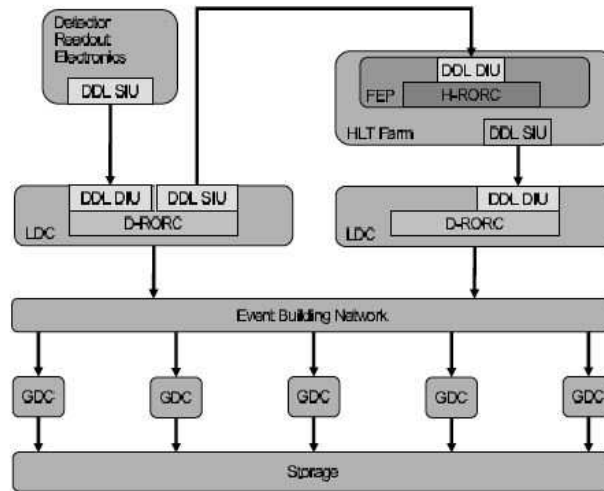


**Figure 4.2:** DAQ-HLT data flow overview.

Every D-RORC sitting in the LDC can host two DIUs. These on-board DIUs can be used in two ways: both can be connected to the front-end electronics and serve as two readout links, or one DIU can be connected to the front-end electronics while the other is able to transfer a copy of all the raw data to the HLT RORC (H-RORC) sitting in the HLT computers, through the standard DDL. The H-RORC receives all the raw data as they have been received from the front-end electronics. All the LDCs dedicated to the detectors which make use of the HLT system are equipped with D-RORCs working in the second mode. The interface between the DAQ and the HLT system is the DIU output on the H-RORC. The selected interface offers as much physics-selection flexibility as possible, since the H-RORC is granted full access to the sub-event and all the raw data are given to the HLT processors. Data will then be available in the HLT farm computers for pre-processing or co-processing in the H-RORC FPGA. The HLT computers will run the HLT algorithms and will transfer the result of the processing, the trigger decisions, and the compressed data to the DAQ system, using again standard DDLs. Using this scheme, the HLT system looks like any other sub-detector for the DAQ. The GDCs will receive the sub-events from the sub-detectors LDCs and any additional data generated by the HLT computers from the LDCs dedicated to the HLT. The DATE software is ready to accept as many data channels from the LDCs dedicated to the HLT as required, since it handles these channels as additional LDC data paths.

The HLT LDCs will also receive messages specifying whether to discard or accept a given event. Furthermore, for accepted events, the HLT decision can specify the pattern of sources for a given event, resulting in a partial readout of the raw data. A decision broker process, running in the HLT LDCs, will transfer the HLT information and decision to a decision agent process, running in the detector LDCs, as shown in Fig. 4.3.

## 4.4 Data Volume and Bandwidth

The ALICE EMCAL, as described in earlier chapters, consists of 1152 towers per super module (SM). Each tower has both a high and a low gain readout channel. The EMCAL is configured with three readout crates, GTL buses, for each SM. Two Readout Control Units, each with a DDL connection to a LDC will be used to readout the three GTL crates (one RCU can service two GTLs). Each GTL will transfer 12 Front-End Cards of  $32 \times 2 = 768$  channels of 10-bit data. There are 10 SM + 2 half SM planned for the full EMCAL for a combined total of 25344 readout channels (12672 towers).

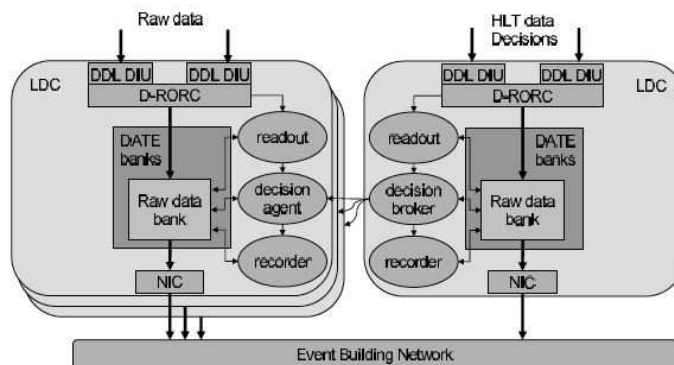


**Figure 4.3:** HLT decision into LDC to control data flow to DAQ.

The data volume per channel is a function of how many ADC time-samples are read out from the ALTRO chip. With the 100 ns shaping planned for the EMCal 3.3 shaper and a 10 MHz sampling frequency, about 10 samples would adequately sample the peak. Up to 15 additional pre-samples may be taken for event-by-event pedestal measurement. Therefore 25 samples would be taken for each of the two shaper gain channels (see Section 3.3). Each sample is a 10-bit ADC word, and the data is formatted into 40-bit words in the ALTRO chip.

The granularity of the EMCal is about 10 times coarser than the PHOS with the result that the EMCal occupancy and tower hit rates are about 10 times larger than PHOS. The tower hit rate for the full 8 kHz min bias Pb+Pb collision rate from HIJING simulations is estimated to be 2000 Hz. This would correspond to a maximum data transfer rate of  $2000 \times 2 \times 25 \times 10/8 = 125$  kBytes/s/tower, or 48 MBytes/s/GTL with zero suppression (see Table 3.2). This is below the DDL data transfer limit of 200 MBytes/s allowing the EMCal to operate without deadtime at the full Pb+Pb min bias trigger rate. The data volume for readout of the full EMCal would be  $(2 \text{ gain ranges}) \times (12672 \text{ towers}) \times (25 \text{ samples}) \times 10/8(\text{Bytes}) = 792$  kBytes per event. The 2 kHz tower hit rate corresponds to a 40 % average EMCal occupancy for Pb+Pb collisions at 8 kHz. The corresponding EMCal average total event size would be 317 kBytes per event. This is much smaller than the 75.9 MBytes size of the average TPC event (Table 7.1 of Ref. [2]).

## 4.5 EMCal Detector Control

The ALICE control system is responsible for configuring, monitoring and controlling the equipment of the experiment. This can be hardware devices such as power supplies, crates, but also more sub-detector specific equipment such as front-end chips, etc. It will also cover computing devices (such as PCs and PLCs) and the software processes running on them. This task is mainly accomplished by sending commands and settings to the equipment and reading information back from the equipment. The control system is designed to take pre-programmed decisions and automatic actions (without operator intervention) such as recovering from errors. The operator will be able to interact with the control system through user interfaces that will present the information from the system and allow issuing of commands. All information concerning any part of the equipment is stored in a configuration database. This information ranges from the physical location of the equipment, hardware addresses, to operational settings (that can be different for the various running modes). Also here the information is not only restricted to hardware but will also cover processes running on PCs, etc.

The ALICE online systems, namely, the Detector Control System (DCS), the Data Acquisition system, the Trigger system (TRG), and the High-Level Trigger system (HLT) interface to each other through a controls layer, the so-called Experiment Control System (ECS), shown in Fig. 4.4.

The core software of the control system [2] is a commercial SCADA(Supervisory Controls And Data

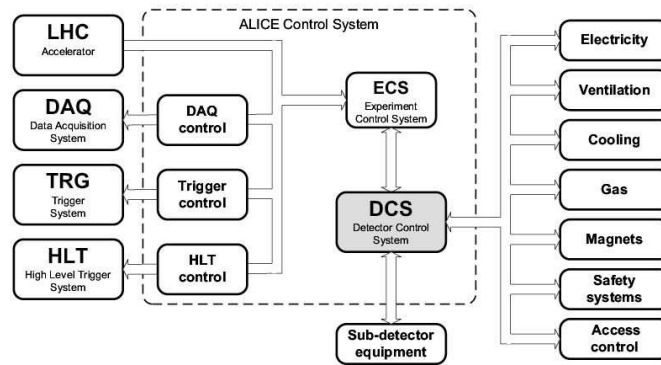


**Figure 4.4:** The ALICE online control systems.

Acquisition) system called PVSSII. It will be used to connect to hardware (or software) devices, acquire the data they produce and use it for their supervision, i.e. to monitor their behaviour and to initialize, configure and operate them. PVSSII has its own proprietary run-time database which is used to store the values that are read from the devices, information on the configuration of PVSSII itself and any information that is needed for the operation of the PVSSII system. This database is optimized for fast access, as it is an essential part in the operation of the PVSSII system. Data archiving is an integral part of PVSSII and is the mechanism to store the history of any data available in the system that the user decides to archive. The PVSSII archiving managers provide an efficient mechanism for storing, accessing and manipulating historical data acquired by the control system. Alarms can be generated by defining conditions applying to new data arriving in PVSSII. The alarms are stored in an alarm database and can be selectively displayed by an alarm display. Alarms can be filtered, summarized, etc.

The EMCAL detector control will be implemented within the ALICE PVSSII environment. The items to be controlled include:

- Low voltages for the front end electronics cards
- High voltage supply for APD bias
- Individual APD HV bias demand values
- Temperature and voltage readback values on FEE cards
- Temperature sensors throughout the EMCAL detector region
- EMCAL cooling water temperature and control
- ALTRO chip parameters: sampling frequency, number of samples, zero suppression thresholds, etc.
- L0 and L1 trigger thresholds and masks



## 5 Detector Calibration and Monitoring

---

### 5.1 Requirements

In order to minimize the EMCal energy resolution for high energy electromagnetic showers it is important to obtain and maintain a tower-by-tower relative energy calibration of better than 1% in the offline analysis. The uncertainty in the tower-by-tower energy calibration contributes to the constant term of the total energy resolution which becomes most significant at high energy. Also, since analog tower energy sums provide the basis of the L0 and L1 high energy shower trigger input to the ALICE trigger decision, the EMCal should operate with APD gains adjusted to match the relative tower energy calibrations online to better than about 5%. This is desired in order to obtain sharp trigger energy threshold turn-on curves.

Both of these goals will be attained through the use of a Light Emitting Diode (LED) calibration system in which all towers view a calibrated pulsed LED light source. Scans of the APD HV bias while taking LED pulser data will allow to determine the absolute APD gain for each channel. Once the LED light yield in each tower is calibrated, the LED itself can be used to track the tower gain in the case of APD bias adjustments, or in the case of APD gain drifts as might result from the known temperature dependence of the APD gain of about 2%/°C (see Section 6 and Table 3.1).

The ALICE offline software will include a calibration database for each detector. The contents of the calibration database will all be ROOT objects and the overall database will be available in the AliRoot file catalog. In principle this is something that is only accessible during the offline analysis, and is not generally available online for the High-Level Trigger (HLT) or the on-detector trigger logic. However, provision will be made for access to this general AliRoot resource, or to local copies of it that are accessible to the Experiment Control System (see Section 4.5) via PVSSII for the low level detector setup, such as for EMCal APD bias adjustments for gain matching, and as well to the HLT processors.

### 5.2 LED Calibration System

An LED calibration system will be incorporated into the EMCal detector to allow to track and adjust the APD gains. A preliminary version of an LED system was incorporated in the prototype modules used in the test beam measurements described in Section 6. In that system, a UV LED (part no. E7113UVC by eLED) was mounted in a small hole in the back enclosure of each module and irradiated a small piece of plastic scintillator that extended into the region of each tower where the WLS fibres were brought together to attach to the lightguide and APD. The scintillation light excited the WLS to provide the calibration signal. Although this system worked adequately for the purposes of the test beam measurements, the light yield was barely adequate, especially for the short shaping times intended to be used for the EMCal readout. Also, the close proximity of the LED to the APD and preamplifier resulted in electronic cross-talk from the large amplitude fast pulse necessary to pulse the LED. The electronic cross-talk was especially problematic for the short shaping time.

As a result of these observations, it is planned to locate the LEDs outside of the EMCal super module and bring the LED light to the EMCal modules via light fibres. An avalanche pulser system will be used to provide ultra-bright LED light pulses of a few ns duration [1]. Such fast ultra-bright LED sources have been used already for investigation of the timing characteristics of the PHOS/EMCal electronics [2]. The LED pulser system will be located in an enclosure to provide electronic isolation from the surroundings. The light from a single LED will be split via a light homogenizer connected to a fibre bundle with one fibre brought to each module, and the LED light itself monitored by a reference photodiode.

### 5.3 APD pre-Calibration

Prior to installation in EMCAL modules, each APD will be attached to its preamplifier and the APD+preamplifier assembly will be tested with an LED pulser system. The tests will be performed to measure the voltage-gain and noise performance of each APD. The information will be recorded in an online database and used to reject APDs with inadequate performance. The information will be used to adjust the bias voltage individually for each APD to match APD gains for initial pre-calibration of the EMCAL towers with cosmic ray muons.

### 5.4 Cosmic Ray Calibration

During the detector construction process, the individual modules will be tested prior to their assembly into the EMCAL super modules. This is required to verify the light-tightness and basic functioning of the module. After the modules are assembled into the super module structure, and the LED calibration system is fully installed, an initial pre-calibration will be performed using cosmic ray muons. Test beam measurements, described in Section 6, have demonstrated that the peak from Minimum Ionizing Particles (MIPs) will provide a measurement sufficient to match the relative calibration of the individual towers to better than 5%. An example of the MIP peak signal for muon triggers is shown in Fig. 5.1

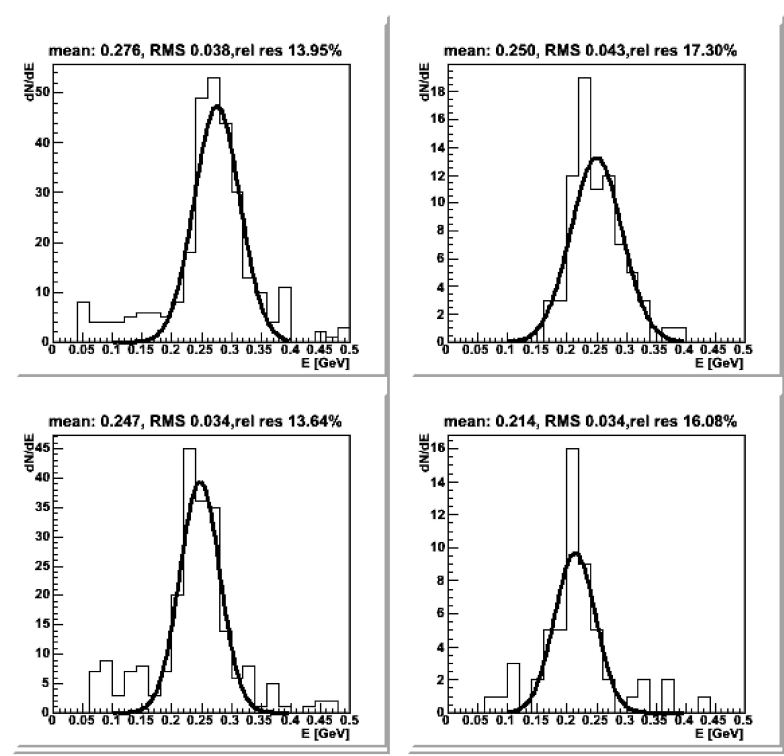


**Figure 5.1:** Pulse height distributions of muons in four EMCAL towers obtained from FNAL test beam measurements.

### 5.5 Gain Monitoring During Runs

As described in Chap. 4.5 of Ref. [3], it is foreseen to be able to take calibration triggers, such as the EMCAL LED calibration trigger, during stand-alone EMCAL operation, as during setup, as well as during physics data-taking. Calibration triggers would be taken during data-taking during the "long gap" of

about  $2.97 \mu\text{s}$  at the time when the orbit reset from the LHC machine is sent. A calibration "pre-pulse" is provided to trigger the LED pulser system followed by an L0 calibration event trigger. The pre-pulse is sent  $1.3 \mu\text{s}$  after the last bunch before the gap, i.e. after the L0 trigger latency of  $1.2 \mu\text{s}$ , to insure that no physics trigger has been issued from that bunch.

The LED calibration data will be analyzed online to monitor the status and track the gain of all EMCal towers. The LED calibration data stream will be split from the physics data stream in order that it can be processed directly to extract correction factors for any time-dependent gain drift. The time-dependent gain correction factors will be entered into the analysis database to allow immediate physics analyses with all time-dependent gain corrections applied.

## **5.6 In-beam MIP, Electron, and $\pi^0$ Calibrations**

The initial tower-by-tower gain matching based on cosmic muon data taken prior to the EMCal installation in ALICE, and the calibration of the absolute energy scale, will be improved using physics data. The high statistics data will allow to use the MIP peak in each tower to adjust the relative gain factors between towers. Identified electrons will be used to check the EMCal energy scale compared to the electron momentum measured by tracking in ALICE. Finally, the measured mass of the  $\pi^0$  peak will also be used to confirm the absolute EMCal energy calibration. With high statistics p-p or peripheral Pb-Pb collision data, two-photon invariant mass spectra can be accumulated for each tower that has either of the two photons centered on the tower and the position of the observed  $\pi^0$  peak can be used to improve the tower energy calibration [4].





## 6 Test Beam Activities and Results

---

### 6.1 Test Beam Measurements at FNAL

#### 6.1.1 Goals and Setup

During a period of four weeks in November 2005 the first ALICE EMCAL prototype modules were tested in the Meson Test Beam (MTEST) at Fermi National Accelerator Laboratory [2]. The test utilized a stacked  $4 \times 4$  array of prototype EMCAL modules ( $8 \times 8$  towers). All towers were instrumented with the same model APD and preamplifier as intended to be used in the ALICE experiment and all channels were read out with existing prototype front end electronics cards intended for use for the PHOS and EMCAL detector subsystems. The readout of the front end electronics used the full ALICE DAQ readout chain.

The goals of the test beam measurements were:

- To verify the expected performance of the EMCAL prototype modules.
- To determine the light yield (signal) per unit of deposited electromagnetic energy.
- To investigate the energy resolution, linearity, uniformity, and position resolution, using electron triggered events.
- To study the energy dependence of the response to electrons and hadrons to determine the particle identification capabilities of the EMCAL by shower shape.
- To investigate the timing characteristics of the energy signal for crude time-of-flight measurement ( $\sim 1$  ns) for possible use for anti-neutron rejection.

Measurements were made for comparison of the performance with two different signal shaping times in the front end electronics (see Section 3). Two front end electronics cards (32 towers each) were used for the readout of the modules; one had the nominal  $1 \mu\text{s}$  signal shaping time which PHOS plans to use, and the other had a modified 100 ns shaping time as planned to use for EMCAL [1].

The experiment took place in the MTEST secondary beam line, located in the area designated MT6 at Fermilab [2]. The proton beam was resonantly slow-extracted from the Main Injector and focused onto the MTEST target for test beam use. The tests were made with mixed beams with good particle identification ( $e/\pi/p$  discrimination) over the full range of available momenta ( $4 - 66 \text{ GeV}/c$ ). The beam momentum selection bite was about  $\delta p/p \sim 1\%$ . The beam intensity was in the range of 0.2–10 kHz dependent on the momentum selected, over an area of a few square cm. The beam spill length was typically about 4 seconds every 2 minutes.

The setup of the EMCAL prototype in the test beam is shown in Fig. 6.1 For handling and stacking purposes, the modules were assembled on a strong-back in strip units of four modules in the vertical direction. The top and bottom surfaces of the modules were the surfaces orthogonal to the front surface, while the side surfaces of the modules had the  $1.5^\circ$  taper (see Section 2). The moveable platform in the test beam consisted of a heavy duty horizontal motion table provided by FNAL. Vertical motion was provided by a commercial scissors table with 680 kg capacity provided by the EMCAL group, that sat upon the horizontal motion table. The total range of both horizontal and vertical adjustment was approximately 50 cm. The size of the stacked array was about  $51 \times 51 \times 50$  cm with a weight of about 400 kg ( $\sim 25$  kg/module).

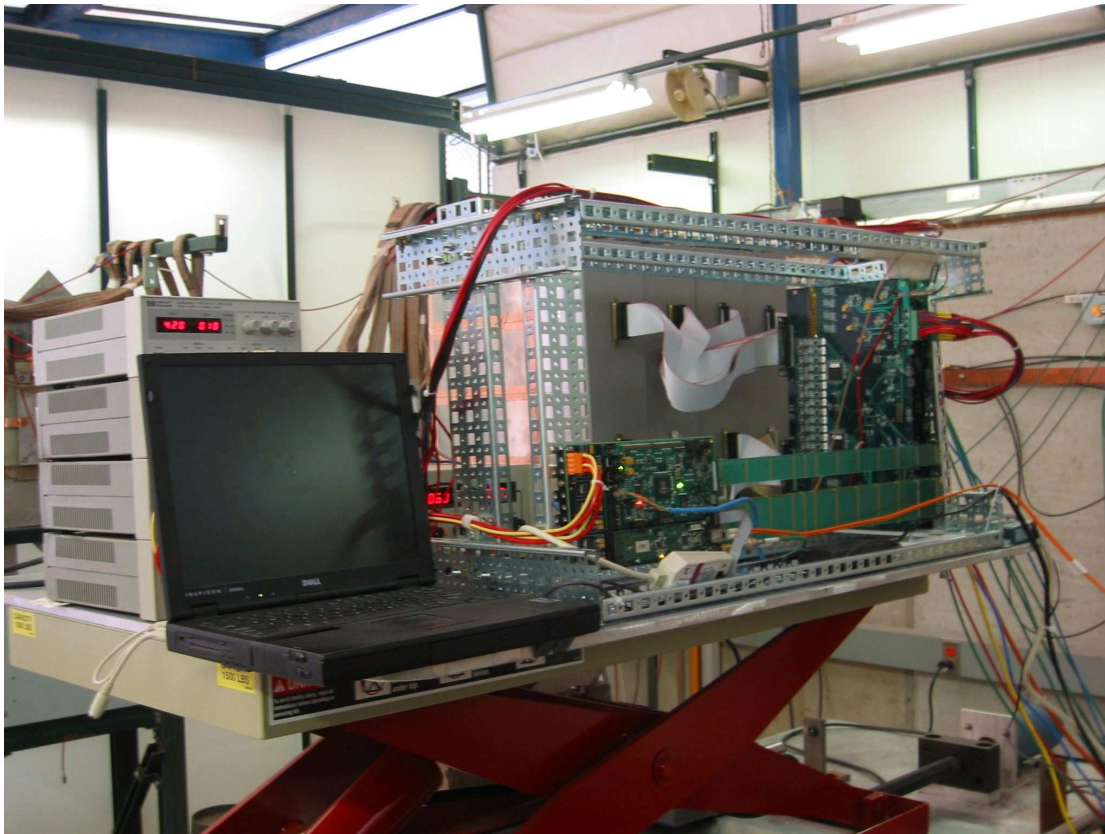


**Figure 6.1:** Rear view of the EMCAL prototype setup in the MT6 test beam at FNAL. Ribbon cables from each pair of modules (8 towers) are seen connecting to two FEE cards that sit on the GTL bus that connects to the small RCU card for readout via optical fibre to the LDC data acquisition that sits in the counting house.

The EMCAL readout electronics was attached to the back of the array of modules with the electronics cards and readout units (DCS/RCU) located on the same moveable table as the modules, together with the LV supplies.

A pair of gas threshold Cerenkov counters were used for electron/pion discrimination. A pair of scintillator paddles, one immediately in front of the EMCAL and one far upstream were used for the beam definition trigger and timing. A set of MWPCs provided x-y position measurement with better than 1 mm position resolution at three stations upstream of the EMCAL (the closest and last station was approximately 2 m in front of the EMCAL). The MWPCs were used to define the beam particle track which could then be projected to the front face of the EMCAL modules. The width of the distribution was approximately 0.9 cm in the horizontal direction and 0.5 cm in vertical direction, as shown in Fig. 6.2.

The official ALICE DAQ (DATE v5) [3] was used for taking the EMCAL data. The MWPC data was taken with the MT6 test beam DAQ system, and the data from the Cerenkov counters and a muon veto paddle located behind the beam stop were taken with a third DAQ system provided by the EMCAL group. The EMCAL data was combined with the data from the trigger detectors and MWPCs offline, aligning the data from the different data streams spill-by-spill.

### 6.1.2 Measurements and Analysis

The test beam period progressed as follows: the first week was spent on physical setup in the test beam, followed by debugging of the readout of EMCAL and associated beam trigger counters. This was done

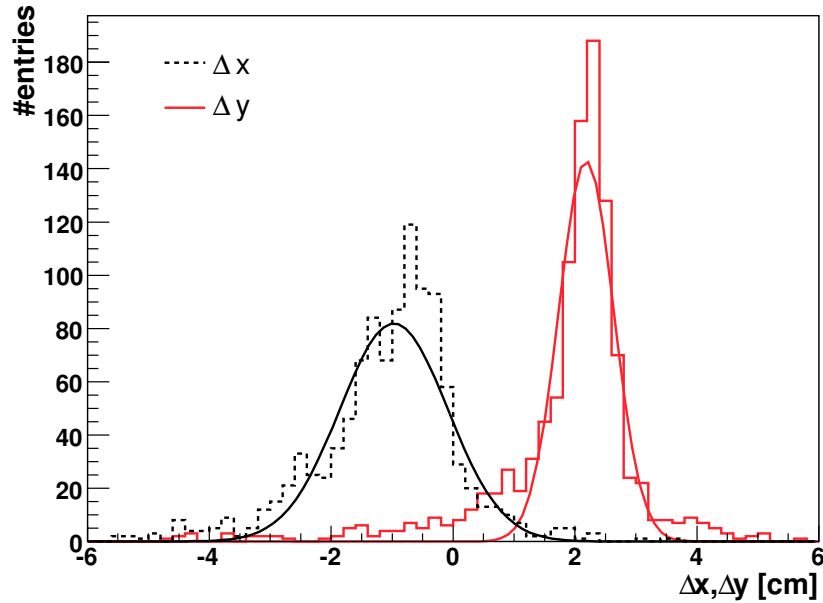


**Figure 6.2:** Beam profile at the front face of the EMCAL modules.

while parasitic users of the test beam. The next week of somewhat intermittent beam was used for gain-matching with a scan with 16 GeV/ $c$  electrons through all towers ( $\sim 1000 e^-/\text{tower}$ ). Subsequently, data was taken for 3 days of 8 GeV/ $c$ , 2 days of 4 GeV/ $c$ , and approximately one day each for 66 and 33 GeV/ $c$ . The goal of this momentum scan with electrons was to investigate linearity and energy and position resolution at several tower locations. For the last portion of the test period detailed position and angle of incidence scans were performed with 4, 8, 16 GeV/ $c$  electrons with modified geometries (tilted and with tower offsets) to investigate the uniformity of the response for different incidence locations corresponding to the super module as installed in ALICE.

The analysis of the data collected is still ongoing. However, even with preliminary calibrations the early analysis results demonstrate that a satisfactory performance has been confirmed, as described in the following sections. The main analysis was performed at the PDSF cluster at LBNL by a team of analyzers from the institutions that participated in the beam test. In total, 18 participants from 8 institutions participated in the beam test <sup>1</sup>.

### 6.1.3 LED Calibration Results

In addition to beam particle data-taking, many runs were taken with pedestal triggers or LED triggers with the goal to track time and temperature dependent effects. The LED system was installed about midway through the test beam period. As a consequence, the test beam measurements were performed with the APDs operated at fixed voltage, rather than at fixed gain. Fig. 6.3 shows an event display for the full  $8 \times 8$  tower array for the high gain channels.

The difference between the two Front End Cards is apparent; the left half [column  $< 4$ ] with the 100 ns shaping time, and the right half with the standard 1  $\mu\text{s}$  PHOS shaper. The histograms show ADC value versus time sample. The x-axis shows 115 sample bins and each time bin corresponds to a sample at 100 ns interval. The LED signal is seen in nearly all towers, but there are significant channel-by-channel variations due to gain variations between individual APDs. The amplitude of the LED signal in the short shaping time cards (on left) is reduced due to the fact that the LED pulse width of 100 ns was

<sup>1</sup>We would also like to acknowledge the assistance from the ALICE DAQ/DATE group for the initial setup of the DAQ software; the PHOS group, and for providing the APDs, FEE cards, and particularly Hans Müller, for help with the readout system overall. The PHOS group also provided the software used in the analysis of the previous PHOS beam test.

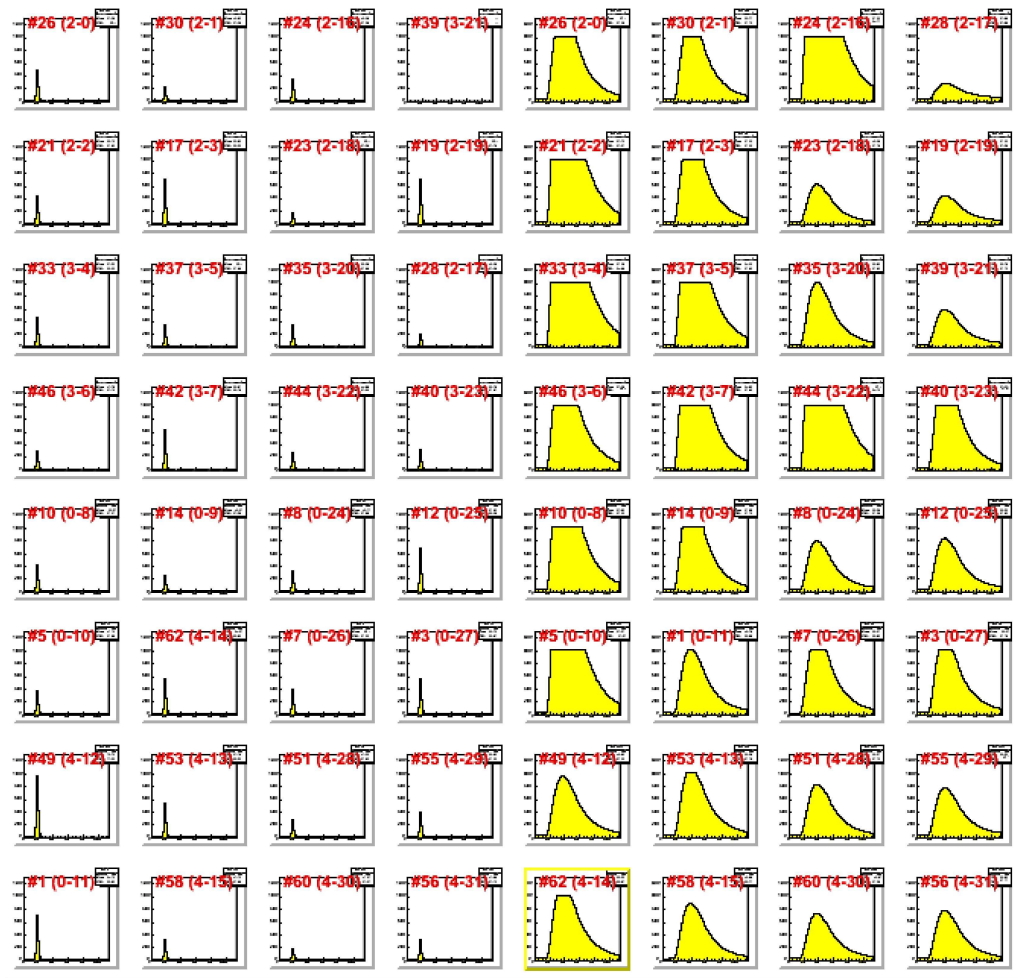


**Figure 6.3:** LED event in  $8 \times 8$  array of EMCAL towers. Left  $4 \times 8$  towers are with short shaping time. Right  $4 \times 8$  towers are with long shaping time. The scale on all plots is the same.

comparable to the shaping time of that FEE card. Furthermore, by design (see Section 3) the gain for the short shaping time FEE card was about 60% of the gain for the card with the PHOS shaper.

Among the things studied were the dependence of the signal amplitude with time and temperature. A dedicated study of the temperature dependence of the APD gain was made on a day without beam by changing the temperature by approximately  $6^\circ\text{C}$  in the experiment hall over the course of a few hours. During this time, the LED system was triggered with the same signal strength at a low rate ( $\sim 0.1$  Hz) and temperature readings were taken every minute. The temperature monitors were mounted at the top and bottom of each strip unit, for a total of eight temperature sensors. An example of the amplitude dependence on temperature for a typical tower is shown in Fig. 6.4. The average reduction of APD gain is seen to be about 2% per degree C. This illustrates the need for temperature stability and continuous temperature monitoring for the super modules when installed in ALICE, as one can expect fluctuations of the temperature in the ALICE experimental area to be of order  $1^\circ\text{C}$ .

#### 6.1.4 Light Yield

As mentioned above, an important goal of the test beam measurement was to extract the average light yield, or number of photo-electrons at the APD per MeV of electromagnetic energy deposit in the EMCAL. This quantity determines the APD+shaper gain necessary to match the desired dynamic range of the

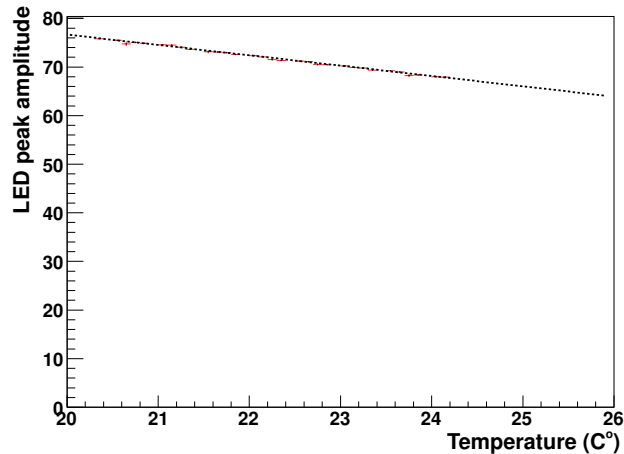


**Figure 6.4:** Measured LED peak amplitude versus temperature.

measurement to that of the input signal to the ALTRO chip for digitization.

The light yield is extracted for each EMCal tower from the calibration coefficient of that tower - in channels/MeV, extracted from the matching of the measured EMCal response to the known electron beam energy. Using the fact that the ALTRO ADC response is 1 Volt input for full scale at channel 1000, and the known amplifier and preamplifier gains (see Section 3, Table 3.2), as well as the measured APD gains, the response in channels can be related to the input charge to the APD. The APD gain is extracted by comparing the signal amplitude as a function of the applied APD bias voltage and extrapolating to zero applied bias voltage where the gain is presumed equal to unity. The APD gains were extracted using short LED runs during which the APD bias voltages were varied. The LED peak amplitude versus the applied bias voltage for a typical tower is shown in Fig. 6.5. From similar measurements for each tower the APD gain at the operating bias voltage can be extracted. During the test beam measurements the APDs were operated at a nominal bias voltage of 380 V with an average APD gain of about 30.

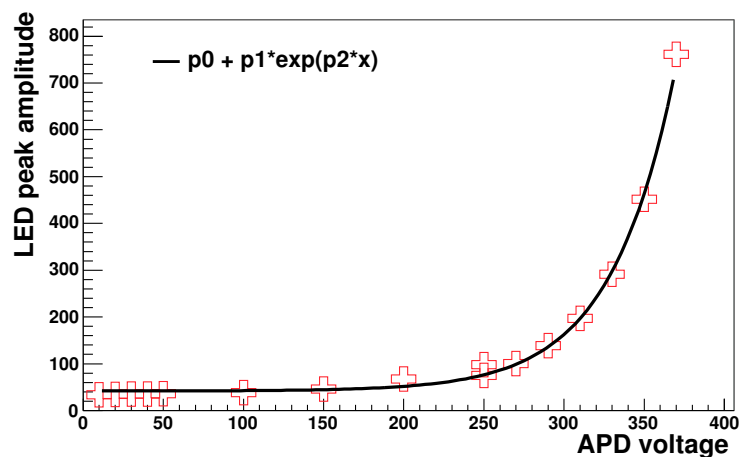


**Figure 6.5:** LED peak amplitude versus APD bias voltage.

After dividing the measured light yields by the APD gain, the light yield at unit gain was extracted and shown for many towers in Fig. 6.6. The average light yield was found to be  $4.4 \pm 0.6$  photo-electrons/MeV, essentially the same as the light yield value of PHOS.

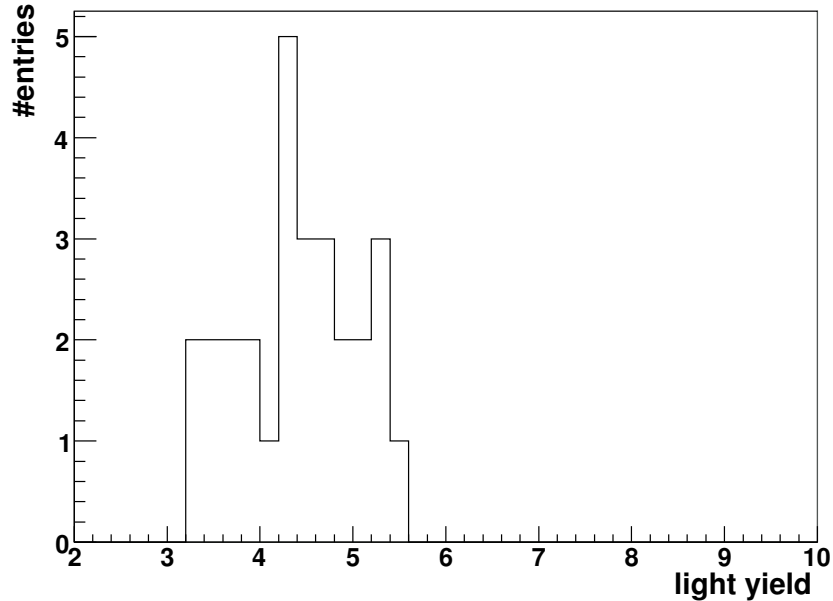


**Figure 6.6:** Distribution of extracted light yields in photo-electrons/MeV (for APD gain  $M=1$ ).

### 6.1.5 Beam Results

As mentioned above, a major goal of the test beam measurement was to investigate the energy resolution ( $\delta E/E$ ) of the EMCal, and how it varied as a function of energy. Since the energy of an electromagnetic shower spreads over several EMCal towers, the energy deposited in the cluster of towers in which energy has been deposited must be summed, with proper relative calibration, in order to extract the total energy deposit in the EMCal. However, since the initial relative calibrations of the towers are unknown, the extraction of the calibration coefficients must be done iteratively. Furthermore, energy may be missing from the sum energy peak as towers on the edge of the cluster may have signals which fall below the pedestal threshold of the towers. Also, the tower calibrations must be determined over a long period of time as the array of modules is scanned through the beam, with the result that the relative calibrations may be determined at different ambient temperatures with corresponding APD gain shifts. All of the results presented here are preliminary in that these various effects are still under investigation.

As described in Section 3 and seen in Fig. 6.3 the digitized time samples have an amplitude as a function of time  $t$  that can be described with the form of a  $\Gamma$ -function as  $ADC(t)$ , where

$$ADC(t) = \text{Pedestal} + A \cdot x^\gamma \cdot \exp^{\gamma(1-x)}, \quad (6.1)$$

$$x = (t_{max} - t)/\tau,$$

where  $t_{max}$  is the time value where the function peaks,  $\tau$  is the decay constant and  $\gamma$  is the power parameter of the fit. The charge collected from the APD, and hence the energy deposited in the tower, is proportional to the value of the parameter  $A$ .

An initial relative calibration of the towers can be obtained by adjusting the gain factors to match the MIP peak in each tower. Fig 6.7 shows results from a preliminary analysis with relative calibrations based on the electron peaks and summing energies of the  $3 \times 3$  group of towers around the central tower where the electron impinged on the EMCal. The left figure shows the energy distribution for all beam triggers, while the right side plot shows the sum energy peak for the same run but selected on events that also fired the electron (Cherenkov) trigger. This cleans up the spectra significantly (note the log-scale) below the full energy electron peak, but does not significantly affect the resolution of the electron peak.



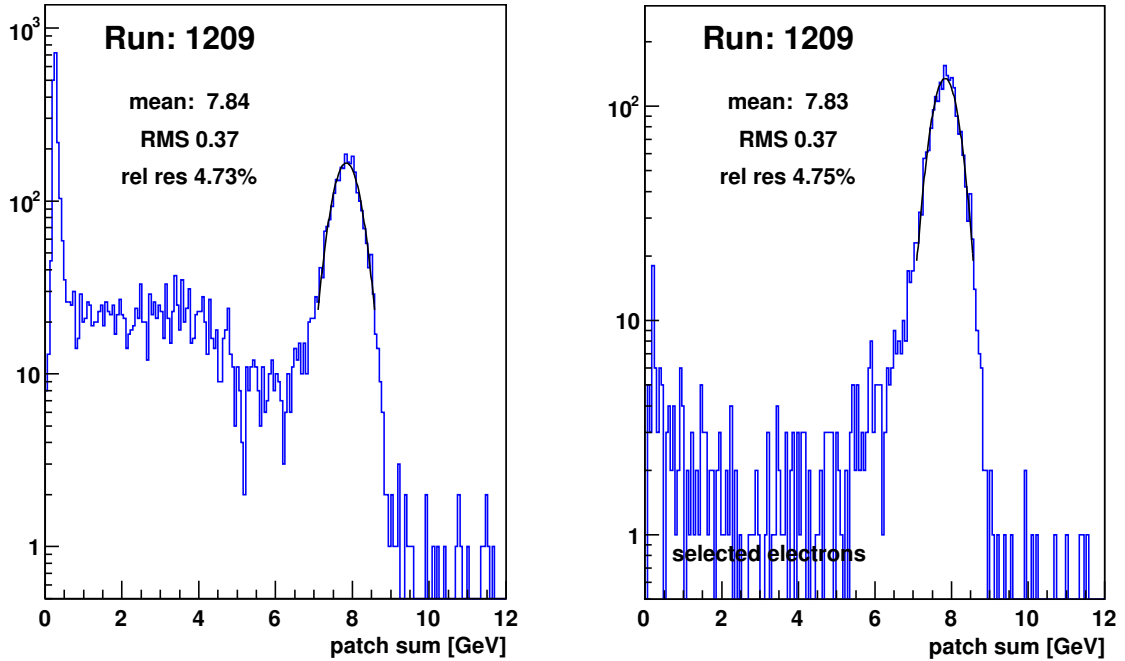


**Figure 6.7:** Sum energy peak for  $3 \times 3$  towers for  $8 \text{ GeV}/c$  beam. Left: All beam triggers. Right: Beam triggers with Cerenkov coincidence.

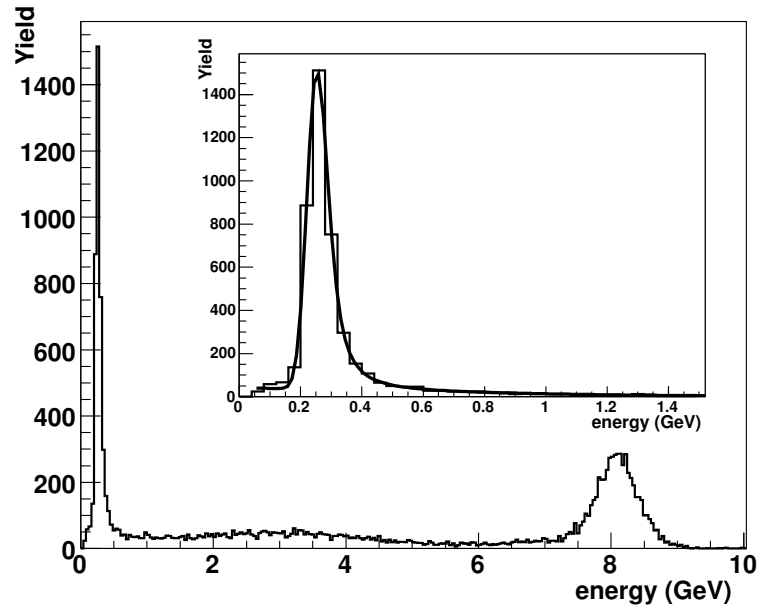


**Figure 6.8:** Sum energy peak for  $8 \text{ GeV}/c$  beam setting. The insert shows the energy spectrum in the region of the MIP peak.

The sum energy spectrum summing all towers in a cluster for an  $8 \text{ GeV}/c$  run is shown in Fig. 6.8. After first tuning the MeV/channel scale for each tower with the MIP pre-calibration and then further calibrating iteratively with the electron peak, an improved energy resolution was obtained. A fit to the energy resolution versus incident energy is shown in Fig. 6.9, where the fit is made to the conventional

constant and  $\sqrt{E}$  term, added in quadrature. The performance is quite similar to the PHENIX EMCAL [4] with similar physical characteristics and better than the stated requirements (see Section 2). One should note that the calibration and analysis was done using the same dataset and concentrated on a particular detector area, so it is a somewhat optimized result. A global analysis using all towers is in progress.

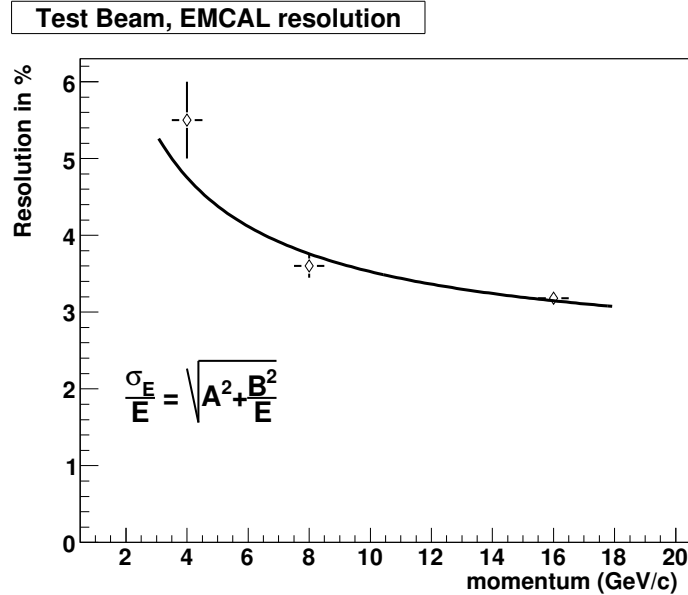


**Figure 6.9:** Energy resolution of electron peak versus beam momentum. The fit result with the two terms added in quadrature gives  $b = 8.4 \pm 0.97$ ,  $a = 2.4 \pm 0.28$ . The GEANT3 simulation for the prototype Module geometry (without light transport included in the simulation) gave  $b = 7.91 \pm 0.05$ ,  $a = 1.05 \pm 0.02$ .

Other analysis topics in progress include shower shape studies and determination of the position and time resolution. A first result demonstrating how well the position of incidence can be extracted from the spatial distribution of energy deposit in the towers of a cluster is shown in Fig. 6.10 where the correlation between hits in the EMCal and track projection from the MWPCs is plotted for a given run.

In addition, the data will be analyzed to investigate the uniformity of response across tower and module boundaries, and how the response differs for modules tilted or recessed as the modules will be positioned when mounted in a super module in the experimental hall.

A second test beam measurement is planned for late 2006, with EMCal modules of the final design from the first module production, and with the full electronics chain with shapers and APD gains operated as planned in ALICE. Another goal will be to exercise the EMCal slow control system for APD bias control.



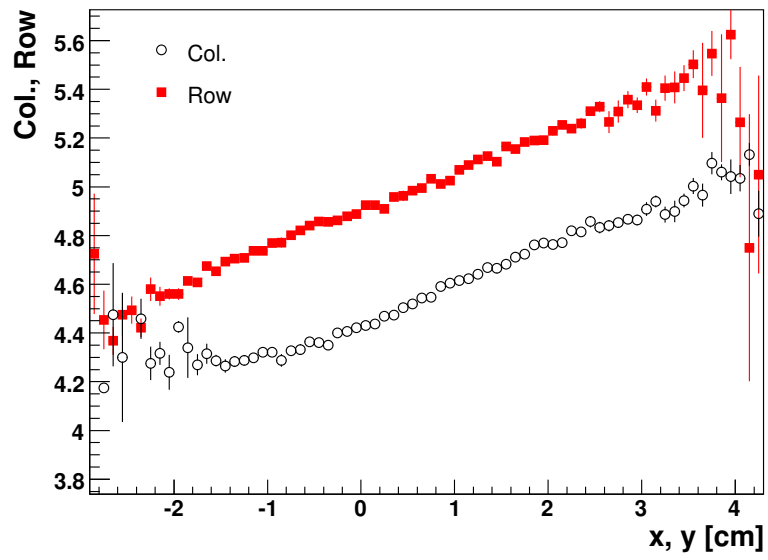


**Figure 6.10:** Correlation between hits in the EMCAL and track projection from the MWPCs.



## 7 Physics Performance

The capabilities of the EMCAL were outlined in Section 1.1. Addition of the EMCAL to ALICE enables triggering on high  $E_T$  jets, improves jet energy resolution, and significantly reduces bias for jet quenching measurements. The EMCAL also triggers and measures rare electromagnetic probes such as direct photons and high  $p_t$  electrons from heavy flavour decays. This section discusses these capabilities in more detail.

### 7.1 EMCAL Trigger

The EMCAL will provide a fast trigger to extend the ALICE  $p_t$  reach for jets, direct photons and electrons from heavy flavour decays (see Fig 1.4). The baseline trigger functionality for the EMCAL is provided by the PHOS front end electronics which provides fast analogue  $2 \times 2$  tower sums at L0, suitable for (trigger Level-0 and 1) photon, neutral hadron ( $\pi^0$  and  $\eta$ ), and electron triggers. High  $p_t$   $\pi^0$  and  $\eta$  also provide a jet trigger, but with a strong bias towards low  $E_T$  jets fragmenting into a hard leading particle and a geometric bias due to partonic energy loss. Comprehensive study of jet quenching requires an unbiased sample of high  $E_T$  jets, obtained by means of a ‘‘jet patch’’ trigger on total energy summed over finite phase space area.

The nominal acceptance of the EMCAL is about 25% of the TPC acceptance. The expected enhancement of EMCAL L1 triggered observables over a minimum bias trigger and TPC analysis is shown in Table 7.1. The estimates in this table are based on simple geometric and event rate considerations. The table shows expected maximum luminosity for various collision systems, the corresponding minimum bias interaction rate, and the maximum rate to tape, which is limited by taping bandwidth and TPC gating frequency (100–500 Hz). The rightmost columns show the enhanced recording rate for the EMCAL trigger relative to equivalent measurements using the TPC only, for observables having negligible phase space area (e.g.  $\pi^0$  in EMCAL vs. charged pions in TPC) and for a jet trigger with area  $\Delta\eta \times \Delta\phi = 0.4 \times 0.4$ .

**Table 7.1:** EMCAL trigger enhancement factor for various collision systems, for small area triggers ( $e,\gamma$ ) and jet triggers of size  $\Delta\eta \times \Delta\phi = 0.4 \times 0.4$ .

|       | $L^{\max}$<br>( $\text{cm}^{-2}\text{s}^{-1}$ ) | interaction<br>rate | max rate<br>to tape | EMCAL enhancement |     |
|-------|---|---------------------|---------------------|-------------------|-----|
|       |   |                     |                     | $e,\gamma,\pi^0$  | jet |
| Pb–Pb | $1.0 \times 10^{27}$                            | 8 kHz               | 100 Hz              | 14                | 10  |
| Ar–Ar | $0.6 \times 10^{29}$                            | 130 kHz             | 500 Hz              | 44                | 31  |
| O–O   | $2.0 \times 10^{29}$                            | 220 kHz             | 500 Hz              | 75                | 53  |
| p–p   | $5.0 \times 10^{30}$                            | 200 kHz             | 500 Hz              | 68                | 48  |

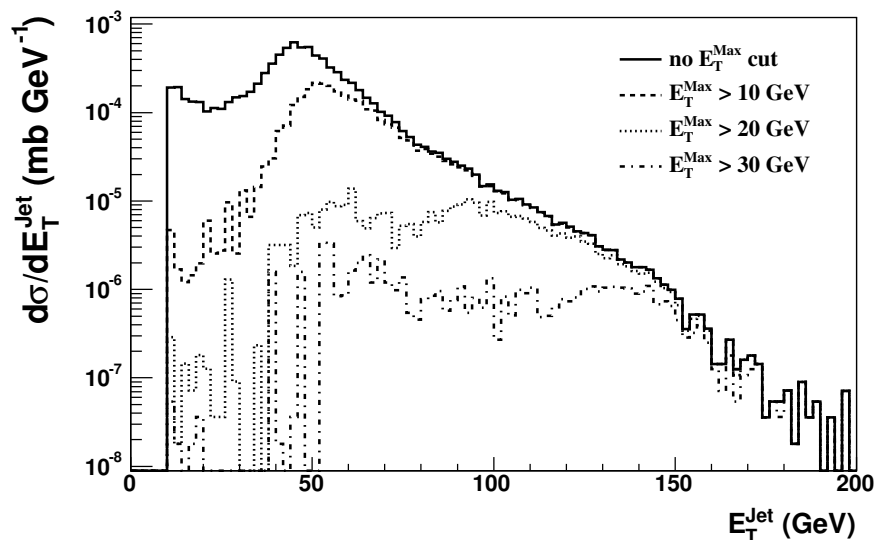
The EMCAL trigger significantly increases the statistics, by an order of magnitude for Pb–Pb collisions, and more for lighter systems, and extends the kinematically accessible range for jet studies by about 70 GeV. The trigger enhancement is greatest for small collision systems with high interaction rate. The enhancement for finite-area jets is somewhat reduced relative to electrons and  $\gamma$ s due to the smaller effective EMCAL acceptance. However, jet measurements incorporating both the EMCAL and tracking have significantly better resolution and less bias than jet measurements based solely on charged particles. Thus the EMCAL-triggered jets provide more robust measurements even for modest trigger enhancements.

### 7.1.1 Heavy-Ion Jet Trigger Requirements

A rare event class such as a jet trigger should typically be recorded at less than  $\sim 10$  Hz. In order to achieve this rate, the total rejection of all trigger levels should be 400-800 in Pb-Pb with correspondingly larger rejection needed for lighter systems with larger interaction rates. The EMCal is sensitive to the full electromagnetic component and about 25% of the hadronic component of the jet energy. The optimal jet trigger will therefore utilize both EMCal and charged track measurements in the High-Level Trigger (HLT), which can provide rejection based on full jet reconstruction. Such a scheme is applicable for heavy collision systems such as Pb-Pb where the recorded event rate is limited by DAQ bandwidth. In lighter systems the recorded event rate is limited by TPC gating frequency to about 500 Hz, and the full jet trigger rejection must be provided by Level-1 in the EMCal.

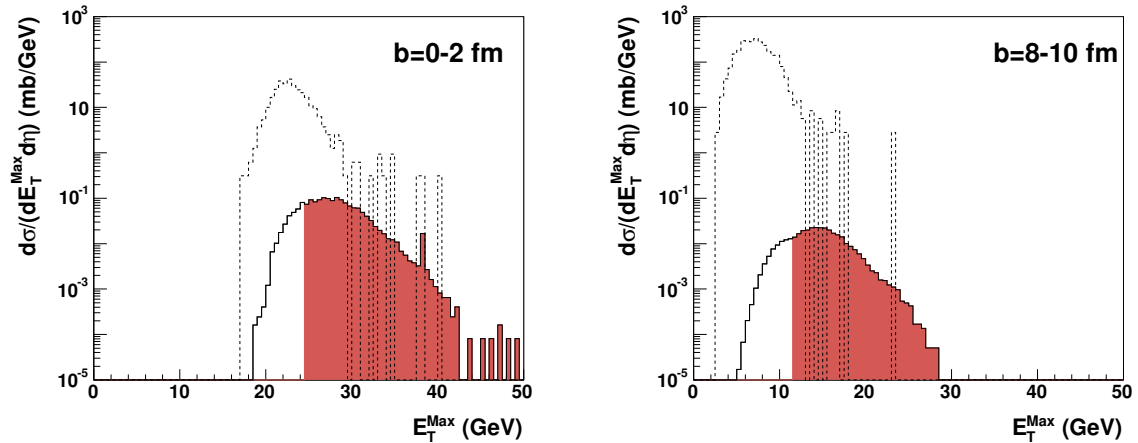
For heavy systems, the role of the Level-1 EMCal trigger is to reduce the event rate sufficiently to match the input bandwidth of the HLT, meaning a rejection factor of 10 for minimum bias Pb-Pb. This section discusses EMCal capabilities for this factor 10 reduction at L1. We have not yet investigated the HLT performance to accomplish the full rejection required in Pb-Pb or the EMCal L1 performance for the full rejection needed in lighter systems.

The EMCal L1 trigger response was studied using PYTHIA-generated jet events and HIJING-generated heavy ion background. A simple parameterization was used for the detector response. The L1 jet trigger algorithm sweeps a square patch of dimensions  $\Delta\eta \times \Delta\phi$  over the EMCal to find the patch with highest integrated energy ( $E_T^{\text{Max}}$ ). Fig. 7.1 shows the jet energy bias in p-p collisions for various  $E_T^{\text{Max}}$  thresholds.



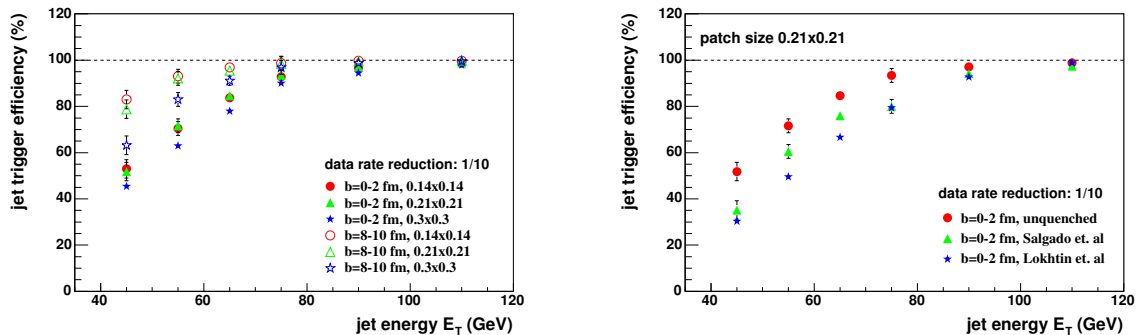
**Figure 7.1:** Trigger bias in p-p collisions for various  $E_T^{\text{Max}}$  thresholds. Features at  $E_T < 50$  GeV are artifacts due to event generation.

Fig. 7.2 shows the  $E_T^{\text{Max}}$  differential cross section distribution for central ( $b=0-2$  fm) and peripheral ( $b=8-10$  fm) Pb-Pb collisions and for the same events with 50-60 GeV jets superimposed. Jet cross sections in Pb-Pb are calculated using the p-p jet cross section scaled by the number of binary nucleon collisions. The filled area in each figure shows 80% of the jet yield, i.e. its lower limit indicates the  $E_T^{\text{Max}}$  cut for 80% jet trigger efficiency. Background fluctuations are significant relative to the intrinsic fluctuations of the jet, both for central and for peripheral collisions. The overall level of background is strongly centrality-dependent, meaning that the  $E_T^{\text{Max}}$  threshold must vary with centrality (by a factor 2 in this calculation) for a centrality-independent jet trigger efficiency. This choice of thresholds reduces the L1 output data rate by a factor 10, roughly the factor needed to match the HLT input bandwidth.



**Figure 7.2:** PYTHIA+HIJING for central and peripheral collisions, jet patch  $0.21 \times 0.21$ :  $E_T^{\text{Max}}$  differential cross section for background (dash-dot) and for background plus 50–60 GeV jets (solid). Filled area shows 80% of embedded jet yield.

Fig. 7.3, left panel, shows the jet energy dependence of trigger efficiency for L1 data rate reduction of 1/10, for central and peripheral collisions and various patch sizes. The trigger efficiency is significantly better for peripheral than for central collisions. The  $0.3 \times 0.3$  patch has poorer efficiency for moderate energy  $E_T < 70$  GeV jets, indicating the faster growth in background relative to signal for increasing patch size. The  $0.21 \times 0.21$  patch is closer to optimal for this model calculation.



**Figure 7.3:** Left: Jet trigger efficiency vs. energy in central and peripheral Pb–Pb collisions, for 1/10 reduction in data rate, for various trigger patch sizes. Right: Effect of jet quenching models on trigger efficiency for central collisions.

Fig. 7.3, right panel, illustrates the effect of jet quenching on the trigger efficiency using two models incorporating partonic energy loss: the Parton Quenching Model (PQM) [1–3] and the event generator PYQUEN [4]. Strong and model-dependent reductions in efficiency are apparent up to  $E_T \sim 100$  GeV, suggesting that jet quenching can have significant influence on the trigger efficiencies.

### 7.1.2 Trigger Summary

Some qualitative conclusions about the EMCAL L1 jet trigger performance and hardware design can be drawn from the above discussion:

- The L1 rejection needed to match the HLT input bandwidth is achievable while maintaining rea-

sonable jet trigger efficiency over a broad energy range.

- Uniform jet trigger efficiency as a function of centrality in nuclear collisions requires a centrality-dependent trigger threshold. The centrality measurement should be supplied by an independent, azimuthally uniform device to avoid autocorrelations and biases due to orientation of the reaction plane. The V0 detector is the appropriate detector for this in ALICE, providing a signal proportional to multiplicity [5] on the required L1 timescale.
- Flexibility in jet trigger patch size: optimization of the jet trigger patch size must balance the reduction in bias provided by larger patches against increasing background rate above threshold. Jet quenching may modify the shape of the jet significantly. The hardware design should be flexible, accommodating a range of trigger patch sizes.

The baseline functionality for L0/L1 triggers provided by the PHOS front end electronics is sufficient for  $\gamma$ ,  $\pi^0$ , and electron triggers. A more flexible trigger system is needed for optimised jet triggers. EMCAL-specific trigger hardware is being developed for this purpose.

The EMCAL achieves trigger enhancements of a factor 10–50, depending on collision system and luminosity, which increases the ALICE kinematic and statistical reach significantly for jet quenching measurements. The increased reach is crucial for mapping the energy evolution of jet quenching, a central goal of the ALICE physics program.

## 7.2 Material Distribution

As a reference for the following sections discussing the physics performance of specific observables, Fig. 7.4 shows the radial distribution of detector material between the vertex and the front face of the EMCAL. The integrated material thickness at mid-rapidity is about 10% of a radiation length at a radius of 280 cm, with more material present at larger radius due to the TRD and especially the TOF. Localized support structures in front of the EMCAL are aligned with the gaps between supermodules and do not contribute to the material shown in the figure. The acceptance for photon and electron measurements does not overlap the support structures. Jets occupy larger phase space, however, and a small fraction of jet fragments will shower in the support material. This has been found to have negligible influence on jet reconstruction performance.

## 7.3 Jet Reconstruction

As discussed in Section 1.1, full jet reconstruction in heavy ion collisions will provide a qualitative advance over leading particle measurements for the study of jet quenching. Leading particle measurements are subject to a strong geometric bias, towards jets which have undergone relative little interaction in the medium. Full jet reconstruction that is insensitive to the detailed pattern of fragmentation will be free of such biases, enabling a much more complete study of jet quenching.

High- $E_T$  jets that are clearly identifiable over the heavy ion background are produced copiously at the LHC [6, 7]. It is nevertheless challenging to achieve good jet energy resolution in the heavy ion environment. This section presents an overview of the main experimental considerations for jet reconstruction in heavy ion collisions, and discusses our current understanding of jet reconstruction performance in p–p and heavy ion events using the EMCAL and ALICE tracking.

Jet reconstruction in elementary collisions is most commonly based on energy measurements using electromagnetic and hadronic calorimeters. ALICE takes an alternative approach, with hadronic energy measured using high resolution charged particle tracking and electromagnetic energy measured using the EMCAL. Hadronic calorimetry is preferred in elementary collisions because of systematic uncertainties due to unmeasured neutral hadrons in the tracking approach (primarily  $K_L^0$  and neutrons). As detailed

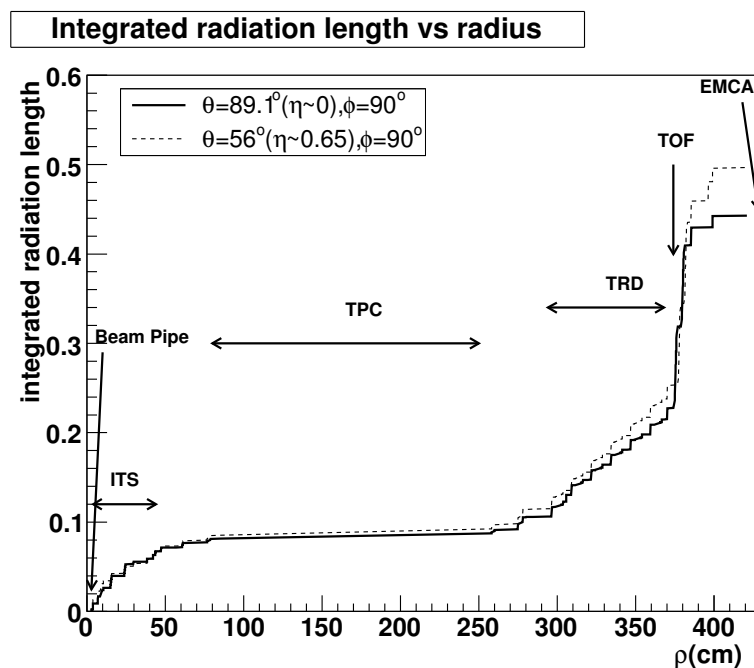


**Figure 7.4:** Integrated radiation lengths of detector material in front of the EMCAL as a function of radial coordinate  $\rho$ , for pseudo-rapidity  $\eta \sim 0$  (full line) and  $\eta \sim 0.65$  (dashed line). The front face of the EMCAL is at  $\rho = 440$  cm.

below, this effect is secondary in heavy ion collisions, where background fluctuations are large and a tracking approach allows a more targeted rejection of low-energy hadrons from soft backgrounds. Jet reconstruction incorporating charged particle tracking in place of hadronic calorimetry is the preferred method for heavy ion collisions.

Hadronic energy deposition in the EMCAL is removed on average using the projection of charged particle trajectories to the EMCAL front face together with a parameterized response to charged particle energy deposition [8]. This approach has been used successfully for jet reconstruction in elementary collisions by STAR [9] and ALEPH [10], with jet energy resolution comparable to traditional hadronic calorimetry methods. The charged particle momentum resolution of ALICE is about 10% at  $p_t = 100$  GeV/ $c$ , which is sufficiently good resolution for hard fragments of the most energetic jets generated in heavy ion collisions (Fig. 1.4). The ALICE two-track resolution is sufficient to maintain this performance in the dense central core of high energy jets.

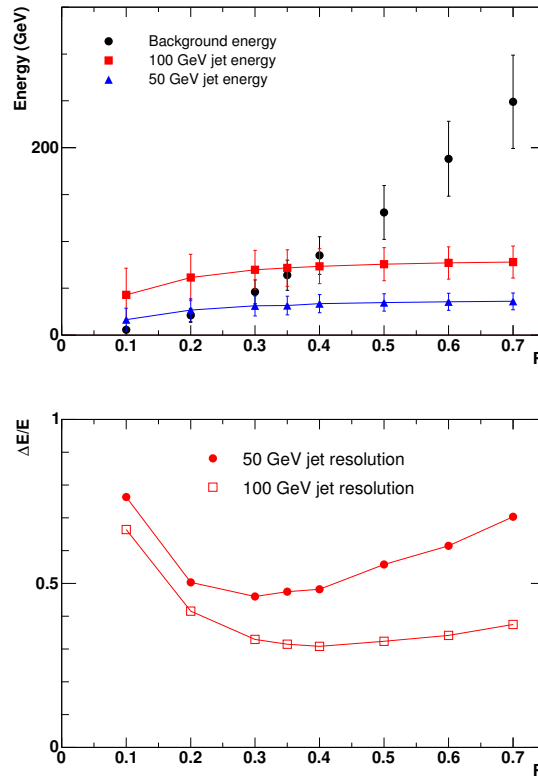
A UA1-type cone algorithm [11] is used for initial studies of jet finding in Pb–Pb collisions since such algorithms allow relatively simple correction of uncorrelated backgrounds.

### 7.3.1 Jet Background Reduction

The main consideration for offline reconstruction of jets in the heavy ion environment is the large background of uncorrelated particles. A recent estimate for central Pb–Pb collisions gives  $dE_T/d\eta \sim 3700$  GeV [12], or about 75 GeV of background energy in a small cone area of  $R = \sqrt{\delta\eta^2 + \delta\phi^2} \lesssim 0.2$ . The essential difficulty in correcting for this large background arises from impact parameter fluctuations, statistical fluctuations due to the finite number of tracks, and dynamical fluctuations due to low  $E_T$  jet production. The impact parameter fluctuations can largely be removed by an event-wise subtraction of background.

Jets measured in  $p$ – $\bar{p}$  collisions have a large fraction of their energy lying within a small forward cone:

for jet  $E_T \sim 50\text{--}100$  GeV, about 80% of the charged track energy is contained in a cone of phase space radius  $R = \sqrt{\delta\eta^2 + \delta\phi^2} \lesssim 0.2$  [13]. This suggests that a reduction in cone size below the commonly used value  $R \sim 0.7$  will improve the signal/background in heavy ion events. A further reduction of the background can be achieved by imposing a lower  $p_t$  bound on the charged tracks used in the jet reconstruction. A study with the HIJING model shows that applying track cut  $p_t > 2$  GeV/ $c$  excludes 98% of the background tracks. The radius and  $p_t$  cuts are correlated, however, due to the well-known angle ordering in jet fragmentation (see Fig. 7.6).



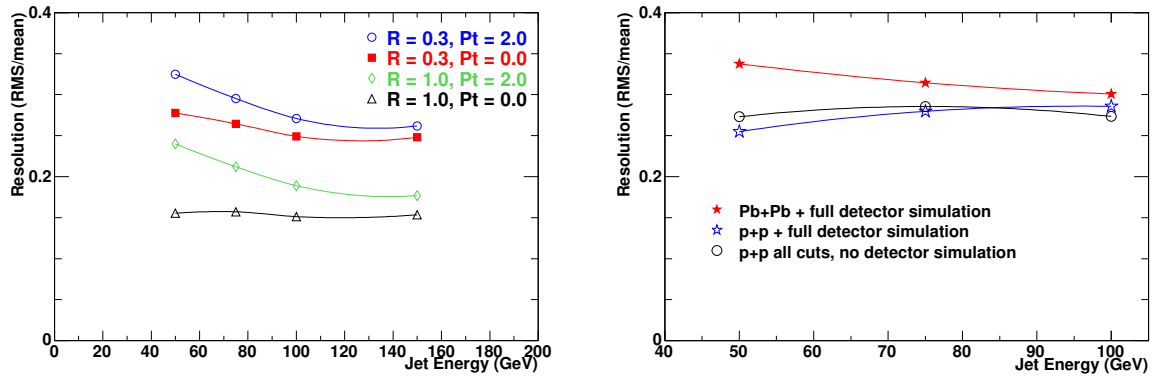
**Figure 7.5:** Left: Background energy (HIJING Pb–Pb central) and jet cone energy (PYTHIA) versus cone radius  $R$  [6, 7]. The vertical bars indicate the RMS of the distributions. Right: jet energy resolution as a function of  $R$ . Only charged tracks with  $p_t > 2$  GeV/ $c$  are used for both panels.

Fig. 7.5, left panel, shows the transverse energy measured with the track cut  $p_t > 2$  GeV/ $c$  as a function of cone radius  $R$ , for 50 and 100 GeV PYTHIA jets and background due to central Pb–Pb events from HIJING. For a 100 GeV jet, the background  $E_T$  exceeds the measured jet  $E_T$  for  $R > 0.4$ . Fig. 7.5, right panel, shows the resulting energy resolution from the cone algorithm for 50 and 100 GeV PYTHIA jets embedded into the HIJING background. A larger radius integrates more jet signal, improving the resolution, while also incorporating a larger background fluctuations which causes deterioration in the resolution. For 50 GeV jets these competing effects lead to an optimum cone radius of  $R = 0.3$ . For higher energy jets the background contributions become relatively less important, leading to a roughly constant resolution of about 30% for  $E_T \sim 100$  GeV jets with  $R > 0.3$ .

### 7.3.2 Jet Energy Resolution

Fig. 7.6, left panel, shows the jet resolution for various sets of cuts. The resolution is calculated with respect to jet reconstruction that uses all generated particles and a cone radius  $R = 1$ . The triangular

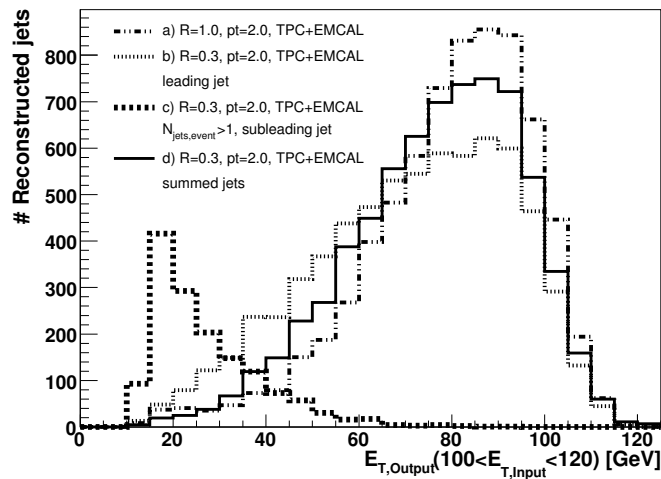




**Figure 7.6:** Energy resolution vs jet energy for different reconstruction schemes [6, 7]. Left: Variation of cone size  $R$  and charged track  $p_t$ -cut for p-p collisions. Right: Effect of detector resolution and background fluctuations.

markers show the best achievable resolution using a cone radius of  $R = 1$  and no track  $p_t$ -cut. The loss of neutral particles, including neutrinos, leads to an energy resolution of 15%. Successive application of the smaller cone radius cut  $R = 0.3$  and the  $p_t$ -cut for charged tracks leads to additional contribution to the resolution of 10% at high  $p_t \sim 100$  GeV and 15% at  $p_t \sim 50$  GeV.

Small jet cone radius and a track  $p_t$ -cut are required to limit background in heavy ion events, but with the present algorithm they are the dominant factors in determining the jet energy resolution. As seen in Fig. 7.6, right panel, the additional contribution to the resolution due to background is modest. Charged tracking momentum resolution (about 10% at 100 GeV) (see Fig. 5.4.3 of Ref. [15]) and EMCAL energy resolution ( $< 10\%/\sqrt{E}$ ) contribute negligibly to the jet energy resolution.



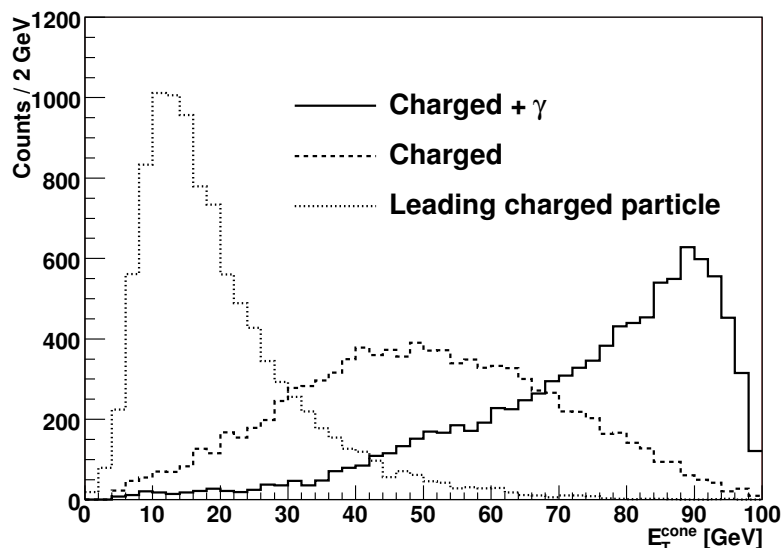
**Figure 7.7:** Effect of jet splitting due to small cone radius.

Fig. 7.6 shows a significant deterioration in resolution as  $R$  is reduced. This effect is explored further in Fig. 7.7 for 100–120 GeV PYTHIA-generated jets. The generated jet is within the EMCAL acceptance, excluding a boundary region to account for its finite size. For reference, curve (a) shows the optimum reconstructed energy distribution for large cone  $R = 1.0$ , with the shift in the peak relative to the simulation energy demonstrating the jet energy lost due to unmeasured particles and the track cut  $p_t > 2$  GeV/c. Curve (b) shows the energy distribution for  $R = 0.3$  jets, taking only the highest energy (leading) jet found in the event. Curve (c) shows the complement of (b), the energy distribution excluding the leading

jet. The multiple jet rate is high for small cone radius, arising from splitting of a jet whose profile is relatively broad due to hard radiation. This results in a pronounced low-energy tail of the leading jet energy distribution which contributes to the resolution due to small cone size shown in Fig. 7.6. A simple way to reduce the effect of jet splitting is to sum the energy of all small- $R$  jets found in the EMCAL acceptance. The resulting distribution curve (d), which shows a marked improvement in jet energy resolution.

Fig. 7.7 suggests that improvements in the reconstructed energy resolution shown in Fig. 7.5 are possible. Measurement of hard radiation may itself be an interesting probe of the medium, though this is as yet an unexplored issue. Development of jet reconstruction algorithms for heavy ion collisions is in its beginning stages, and optimization of biases and resolutions will require a continuous interplay of experiment and theory.

### 7.3.3 Jet Measurement Biases



**Figure 7.8:** Distribution of reconstructed energy for monochromatic  $E_T = 100$  GeV jets reconstructed using leading charged particles, charged particle jets, and charged+EM jets. Jet reconstruction uses  $R = 0.4$ ,  $p_t > 2$  GeV/ $c$ .

Fig. 7.8 shows distributions of reconstructed energy for a monochromatic input sample of  $E_T = 100$  GeV jets for three different jet reconstruction schemes: leading charged particle (LCP), all charged particles, and charged+EM jets (labelled “Charged+ $\gamma$ ”) in which, in addition, the EMCAL response is included. The jet cone is  $R = 0.4$  and the track cut is  $p_t > 2$  GeV/ $c$ . For the LCP the most probable measured fraction of jet energy is below 20%, though with a long tail to much larger fraction. Charged-only jets contain on average about 50% of the jet energy, though likewise with large fluctuations. Addition of the EMCAL increases the most probable measured fraction of jet energy to 90%, though with a tail to lower fraction whose origin is in part due to jet splitting, as discussed in the previous section.

When convoluted with the steeply falling jet spectrum, this response results in a bias in the jet energy distribution. For the physical jet spectrum the long tail to the right for leading particles results in an average measured fraction of the jet energy of about 60%, compared to less than 20% for a monochromatic jet sample. Fig. 7.9 shows this bias for LCP, charged-only jets, charged+EMCAL, and ideal calorimetry (including neutron and  $K_L^0$  energy). The lower sets of points in each panel are the ratio of reconstructed to generated energy as a function of *generated* energy (i.e. response to a monochromatic source), with the vertical bars showing the rms of the distribution. The upper sets of points show the same ratio plotted

as a function of *reconstructed* energy, demonstrating the bias due to the physical jet spectrum. There is markedly less bias for Charged+EMCal when compared to Charged alone.

The key jet quenching measurement is the fragmentation function, which requires accurate knowledge of the underlying jet energy. This measurement therefore requires correction for the bias shown in Fig. 7.9. However, jet quenching itself changes the fragmentation function and will alter the bias, adding additional uncertainty to the correction factor. It is therefore crucial to *minimize* the jet energy bias in order to control the systematic uncertainty of the fragmentation function measurement. This can only be done by measuring as large a fraction of the jet energy as possible.

Partial jet reconstruction combined with partonic energy loss also results in a *geometric* bias. In the extreme case of inclusive hadrons, the measured spectrum is dominated by jets which have had relatively little interaction in the medium, in other words those jets generated at the periphery of the collision zone and headed outwards. The bias is *against* much of the interesting physics, for instance those jets that have undergone catastrophic energy loss and whose energy and momentum are carried dominantly by soft hadrons. Fig. 1.1, right panel, shows that leading hadron measurements indeed have little sensitivity to the properties of the medium. This bias can be minimized only by measuring as large a fraction of the jet energy as possible.

The EMCal enables ALICE to measure a significantly larger fraction of the jet energy than is possible with charged particle tracking alone. The resulting minimization of jet energy bias and geometric bias (together with the fast jet trigger) provide essential improvements to ALICE for the study of jet quenching. It reduces sensitivity to the details of the fragmentation, which are unknown for quenched jets and indeed the object under study, allowing measurement of a less biased jet sample and a correspondingly more sensitive and complete study of jet quenching at the LHC.

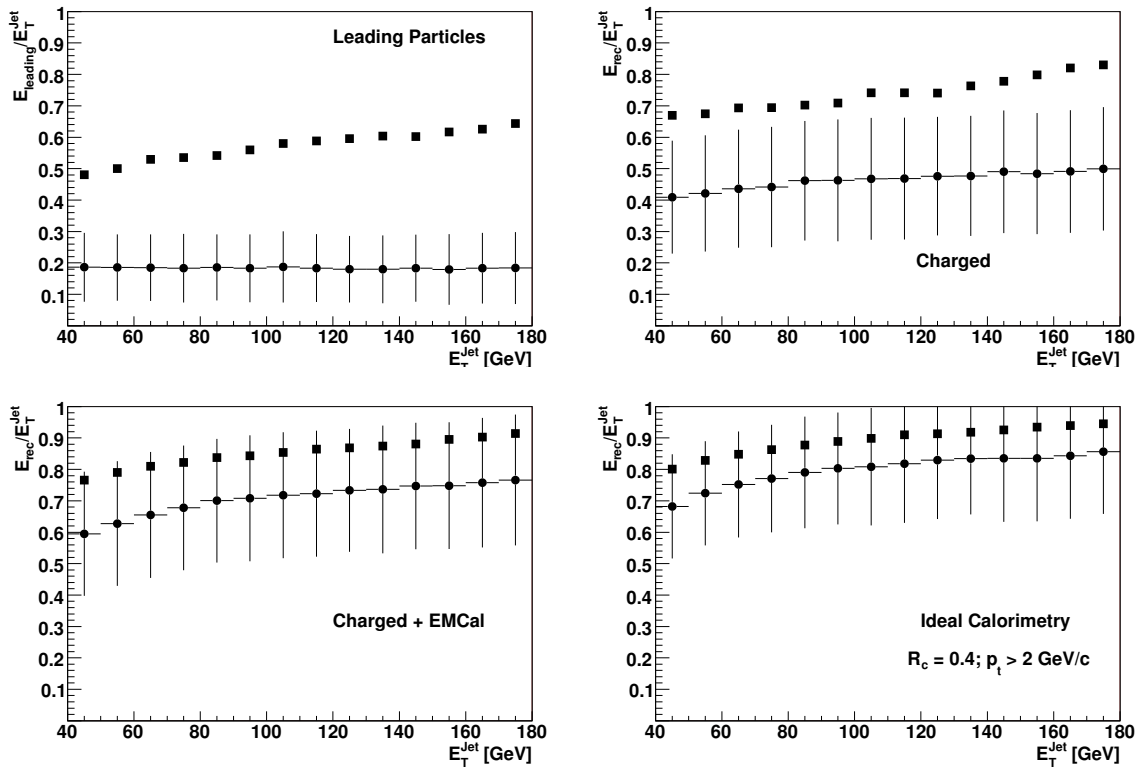


**Figure 7.9:** Dependence of jet energy measurement bias on measured particles. The vertical axis shows the ratio of reconstructed to generated energy. For the circles the horizontal axis is the generated energy, whereas for the square points the horizontal axis is the reconstructed energy.

## 7.4 $\gamma/\pi^0$ Discrimination and Direct Photons

Photons do not interact with the medium and therefore provide an important calibration for jet quenching. At RHIC, the inclusive direct photon yield is a convincing cross-check for high  $p_t$  hadron suppression measurements of partonic energy loss (Fig. 1.1). Even more significant would be the coincidence measurement of a direct photon with fragments of the recoiling jet. To leading order the photon energy gives the energy of the jet, allowing a precise determination of the modified fragmentation function. Direct photon rates in the ALICE acceptance are significant up to  $p_t \sim 50$  GeV/ $c$  (Fig. 1.4). These measurements are challenging, however, due to the small  $\gamma/\pi^0$  ratio and large fragmentation photon backgrounds.

The ALICE PHOS is a finely segmented Lead-Tungstate calorimeter, targeted at precision measurement of direct photons and correlations. The EMCal has a factor eight larger phase space coverage than the PHOS, with somewhat coarser granularity (a factor 3 larger in both  $\Delta\eta$  and  $\Delta\phi$ ). The EMCal may be able to extend ALICE photon measurements to higher  $p_t$  due to its larger coverage. However, some aspects of this measurement have not been explored and definitive conclusions about the photon measurement capabilities of the EMCal cannot be drawn at this time. We present here some preliminary considerations and identify open questions.

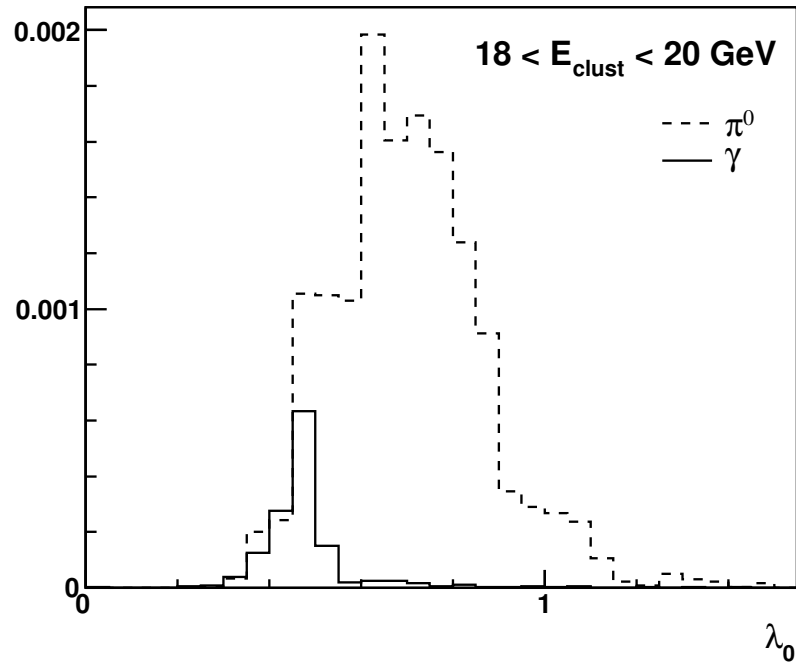
Direct photon measurements are subject to large backgrounds from neutral meson decay ( $\pi^0$ ,  $\eta$ ). At low  $p_t$  the decay photons generate separate calorimeter showers and mesons can be reconstructed based on the two-photon invariant mass spectrum. At higher  $p_t$  the decay photon showers merge, and shower shape observables are needed to separate  $\pi^0$  from direct photon signals. Highly asymmetric decays will mimic the direct photon signal, thus the physical  $\gamma/\pi^0$  yield ratio (a few times  $10^{-2}$  in p-p collisions at the LHC) plays a crucial role in determining the practical  $p_t$  reach of a given measurement.

An additional background to direct photon production is hard bremsstrahlung from a quark jet (“fragmentation photons”), which at the LHC may dominate the real photon yield up to  $p_t \sim 50$  GeV/ $c$  [14]. Such photons are accompanied by hadrons from the jet and can be suppressed by means of an isolation cut. Studies for the PHOS find hadron suppression due to isolation cuts of a factor about 20 in heavy ion collisions [15]. The effectiveness of isolation cuts for the EMCal is under study and we do not discuss it further here. In this section we restrict our discussion to EMCal capabilities for discriminating direct photons and  $\pi^0$  at high  $p_t$  using the shower shape.

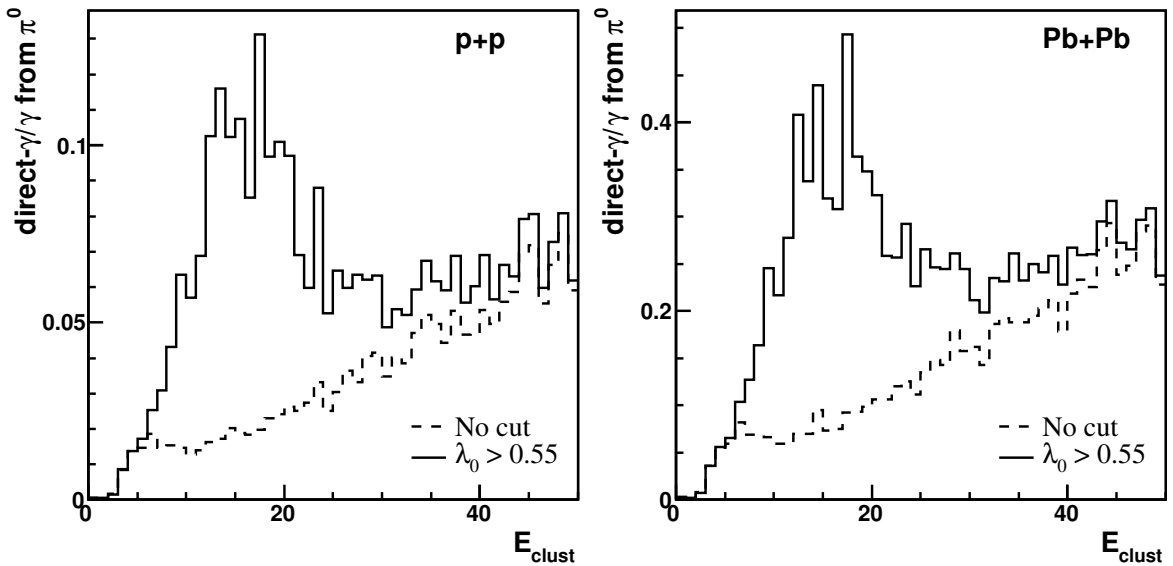
At high  $p_t$ , the showers of the decay photons will merge and be reconstructed as a single cluster. Merged showers can be distinguished from single photon showers by a shower shape analysis. The best separation is obtained based on the width  $\lambda_0$  of the cluster along the major axis of the shower shape ellipsoid. This width is calculated using logarithmic energy weighting to take into account the finite tower size [16].

Fig. 7.10 shows the EMCal  $\lambda_0$  distribution for  $\pi^0$  and  $\gamma$  clusters with  $18 < E_{clust} < 20$  GeV, from a GEANT3 simulation of single photons and  $\pi^0$ . In this momentum range a suppression of  $\pi^0$  background by a factor of 4 can be achieved by selecting clusters with  $\lambda_0 < 0.55$ . The resulting  $\gamma/\pi^0$  ratio as a function of cluster energy  $E_{clust}$  for p-p and Pb-Pb events is shown in Fig. 7.11. A parameterization of the spectra from a NLO pQCD calculation [14] was used to scale the yields. The NLO  $\gamma/\pi^0$  ratio is shown by the dashed lines. For Pb-Pb collisions, a suppression of  $\pi^0$  production by a factor 5, in accordance with RHIC results, was assumed. While the background from other particles in the event was not taken into account in this simulation, a single EMCal tower energy cut of 300 MeV is applied for the Pb-Pb case, which is known to reject most of the background. The cut was lowered to 100 MeV for the p-p case, leading to a slight improvement in the shower shape determination. Note that the ratios are shown as a function of reconstructed cluster energy  $E_{clust}$ , which corresponds to the photon energy for direct photons and isolated decay photons but is closer to the  $\pi^0$  energy for merged clusters of decay photons.

The EMCal granularity provides  $\gamma - \pi^0$  discrimination via shower shape in the range  $p_t \sim 10$ – $30$  GeV/ $c$ . Due to the low  $\gamma/\pi^0$  ratio, however, a robust  $\gamma$ +jet measurement requires additional hadron rejection from isolation cuts, which have not yet been investigated in detail. At lower  $p_t$ , invariant mass



**Figure 7.10:** Distributions of the shower shape parameter  $\lambda_0$  for the EMCal (see text) for clusters from photons and  $\pi^0$  from GEANT3 simulations of single particles, reweighted to the expected spectra from NLO pQCD calculations. Cluster energies in the range  $18 < E_{\text{clust}} < 20$  GeV were selected.



**Figure 7.11:** Expected ratios of calorimeter clusters from direct photons and  $\pi^0$  as a function of cluster energy for p–p (left) and Pb–Pb (right). The dashed lines shows the ratio without shower shape cut and the solid line is with shower shape cut. Input spectra are a parameterization based on a NLO pQCD calculation [14], assuming a factor 5 suppression for  $\pi^0$  in Pb–Pb (note the different vertical scales). See text for details.

analysis can be used for  $\pi^0$  rejection. The  $p_t$  reach up to  $p_t \sim 30$  GeV/ $c$  matches well the statistical reach for  $\gamma$ +jet production (Fig. 1.4).

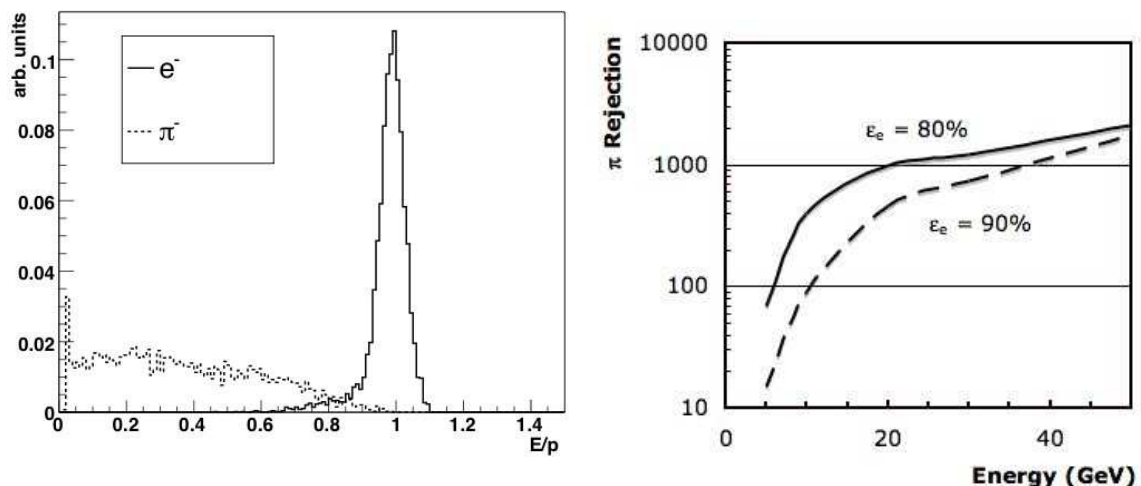


**Figure 7.12:** GEANT3 calculations of electron/hadron discrimination utilizing the EMCAL and TPC. Left panel:  $E/p$  for  $p = 20$  GeV electrons (black) and pions (red). Right panel: Pion rejection ( $=1/\text{efficiency}$ ) vs electron momentum for 80% (upper) and 90% (lower) electron efficiency.

## 7.5 Heavy Quark Jets

Gluon radiation induced by the passage of a massive quark through coloured matter is suppressed in a forward cone with opening  $\theta_C < m_Q/E$ , where  $m_Q$  is the quark mass and  $E$  its energy. The magnitude of this “dead-cone effect” results in significantly smaller radiative energy loss for heavy quarks than for light quarks at moderate momentum ( $p \lesssim 20$  GeV for b-quarks) [17]. At higher momentum the dead-cone effect is negligible but a difference in energy loss between jets led by B- or D-mesons (quark jets) and light hadrons (dominantly gluon jets) is still expected due to the difference in colour charge of gluons and quarks (factor 9/4) [18]. The study of heavy quark jet production over a broad energy range therefore provides key tests of the mechanisms underlying partonic energy loss.

Fig. 1.4 shows significant inclusive electron yield from the semi-leptonic decay of charm and bottom quarks, up to  $p_t \sim 25$  GeV/ $c$  in the ALICE acceptance. Several detectors provide identification of electrons (TRD and TPC) and the measurement of displaced vertices (ITS), giving ALICE good capabilities for the measurement of heavy quark jets [19]. The EMCAL may provide a high  $p_t$  electron trigger with good discrimination, augmenting ALICE’s capabilities for measurement of the highest energy heavy quark jets. Studies of EMCAL performance in this area have only begun, however. We present here some preliminary considerations, without drawing conclusions about the overall capabilities of the EMCAL to trigger on and measure heavy quark jets.

Misidentified hadrons are a large source of background for electron measurements. Figure 7.12, left panel, shows the ratio  $E/p$  of EMCAL energy to track momentum measured in the TPC for 20 GeV electrons and pions, while the right panel shows pion rejection as a function of electron momentum. At 20 GeV, pion rejection of about 1000 is obtained for 80% electron efficiency.

Additional electron backgrounds come from photonic sources (conversions and Dalitz decays). Fig. 7.4 shows a total radiation length of material interior to the TPC of less than 10%. The STAR collaboration, with a configuration similar to ALICE, has demonstrated that a large fraction of conversion and Dalitz pairs can be reconstructed and rejected based on invariant mass [20]. Conversions in the outer material (TRD and TOF) should be rejected efficiently offline by the  $E/p$  cut, though they will contaminate the electron trigger. Rejection of these conversions by the High-Level Trigger may be possible in Pb–Pb collisions. These and other background sources require further study.



## 8 Integration and Implementation

---

### 8.1 EMCal Support Structure - General

The EMCal detector itself weighs approximately 85 metric tons, or 7.7 metric tons per super module. It is supported on a support structure (CalFrame) that in itself weighs about 20 metric tons. The full weight of the EMCal and its support structure is transferred to the ALICE magnet iron via two pre-existing I-beams that span the length of the magnet as seen in Fig. 8.1.

The CalFrame is scheduled for installation inside ALICE in August 2006, at least one year before the fabrication of the first super module is complete. Therefore the CalFrame was designed to incorporate rails for the insertion and removal of super modules during later installation windows. This is discussed below.

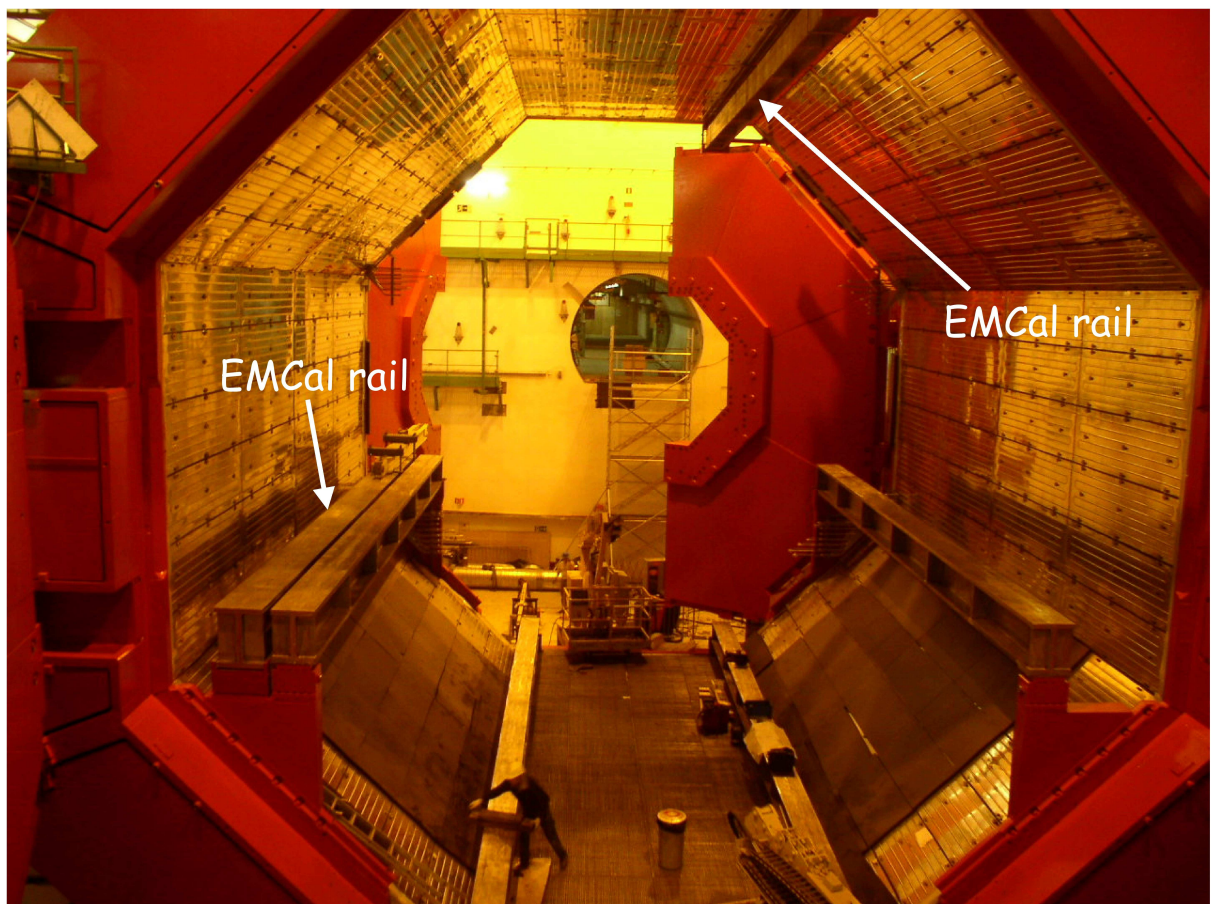


**Figure 8.1:** Photograph of the ALICE magnet showing the EMCal support structure I-beams. The lower and upper I-beams which support and position the CalFrame are visible at approximately 8 o'clock and 1 o'clock respectively.

## 8.2 CalFrame Design Constraints

The allowable integration volume of the EMCal and its support structure is bounded from the IP between 4320 mm and 5400 mm radially and  $\pm 3500$  mm axially. The azimuthal envelop is set by the two pre-existing support I-beams. This integration envelope includes the stack up of all fabrication tolerances and deflection of the CalFrame when fully loaded with 11 super modules. The CalFrame was designed to occupy minimum radial space so as to maximize the radial space available for the super modules and yet to keep the radial deflection to a minimum. Since the CalFrame is radially thin, there was never any question of excessive material stresses provided a frame design does not exceed the maximum allowable deflection. The CalFrame is similar in concept to the fuselage of an airplane or the hull of a ship. Fig. 8.2 shows a CAD isometric representation of the CalFrame. The outer skin of the structure is attached to flanged ribs which are in turn separated by stringers which keep the skin from having large deflections between flanges.

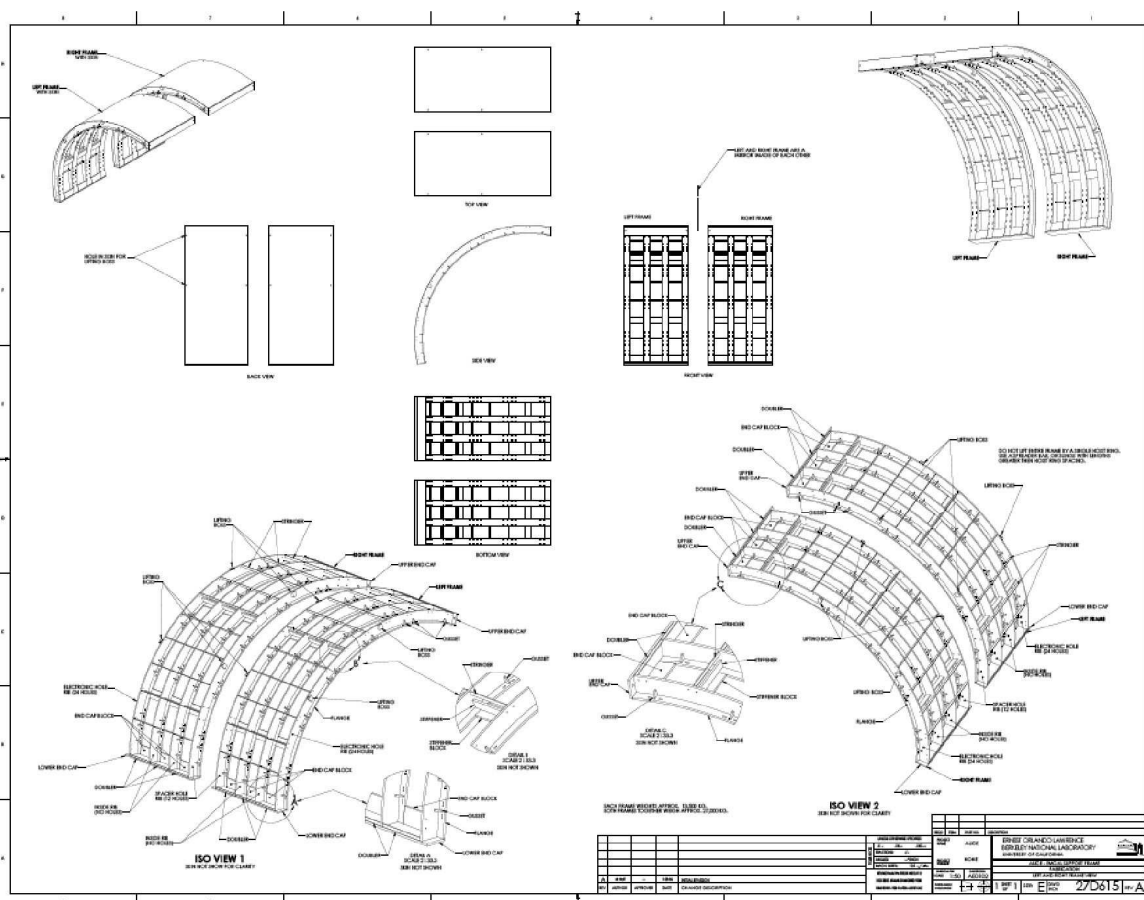
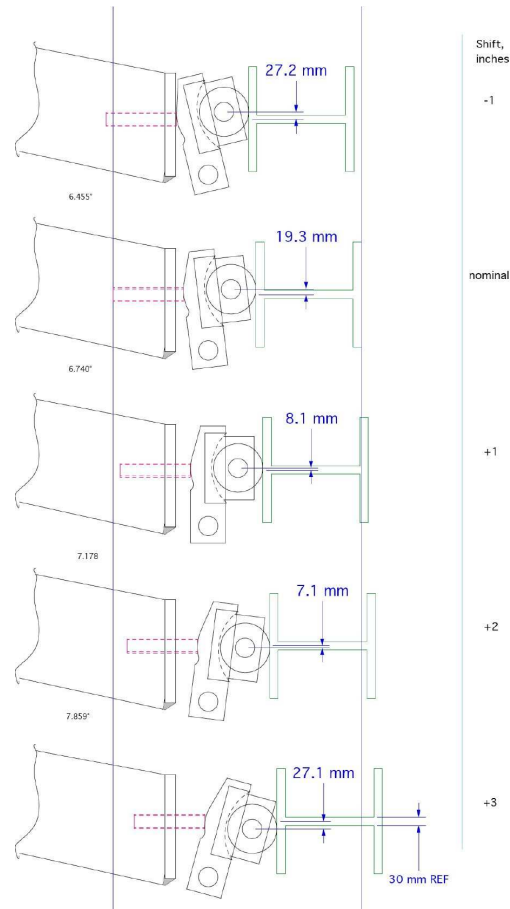


Figure 8.2: CAD model of the CalFrame.

The upper I-beam installed in the ALICE magnet is designed only to provide horizontal reaction to the CalFrame. To prevent it from also providing a vertical reaction, the upper support contact between the CalFrame and the upper I-beam is via wheels mounted along the upper edge of the CalFrame with axes oriented horizontally and parallel to the beam axis. This allows the extreme upper end of the support structure to move in the vertical direction as the total load increases during super module installation. Fig. 8.3 shows the concept for various load conditions on the support structure. The axes of the wheels may also be oriented vertically so that the wheels roll along the length of the upper beam when the CalFrame is installed into ALICE.





**Figure 8.3:** Cam mounted wheels between the CalFrame and the upper support I-beam shown for various load and deflection conditions.

### 8.3 CalFrame Structural Analysis

A finite element model of the CalFrame was developed in ANSYS WorkBench to study the structural performance of the CalFrame. The model was used to optimize the strength of the design and to reduce material weight and fabrication cost. The FEA models were verified independently by a team of engineers at LBNL and CERN. The boundary conditions applied to the support structure and the two support beams are:

1. The upper end of the CalFrame has only a horizontal reaction applied to it by a horizontally-oriented upper I-beam.
2. The lower end of the CalFrame has both vertical and horizontal reactions applied by a vertically-oriented lower I-beam.

Deflections and stresses were then first calculated for the CalFrame alone. When the EMCAL is fully loaded, the calculated maximum vertical deflection in the baseline design CalFrame alone is less than 25 mm and is located at the 12 o'clock location. Fig. 8.4 shows the final FEA deflection result for a total detector load of 110 metric tons. The maximum deflection is 22.7 mm. This load exceeds the actual weight of the detector by a factor of about 1.3. We conclude that the deflections under full load of the support structure itself are rather modest. In addition to this, the combined deflection and rotation of the lower I-beam contributes an additional 40 mm to the support structure vertical deflection with a similar amount contributed by the upper I-beam. Thus when deflections in both the upper and lower support

beams are considered, the maximum total deflection sums up to about 100 mm. This net deflection is large but acceptable.

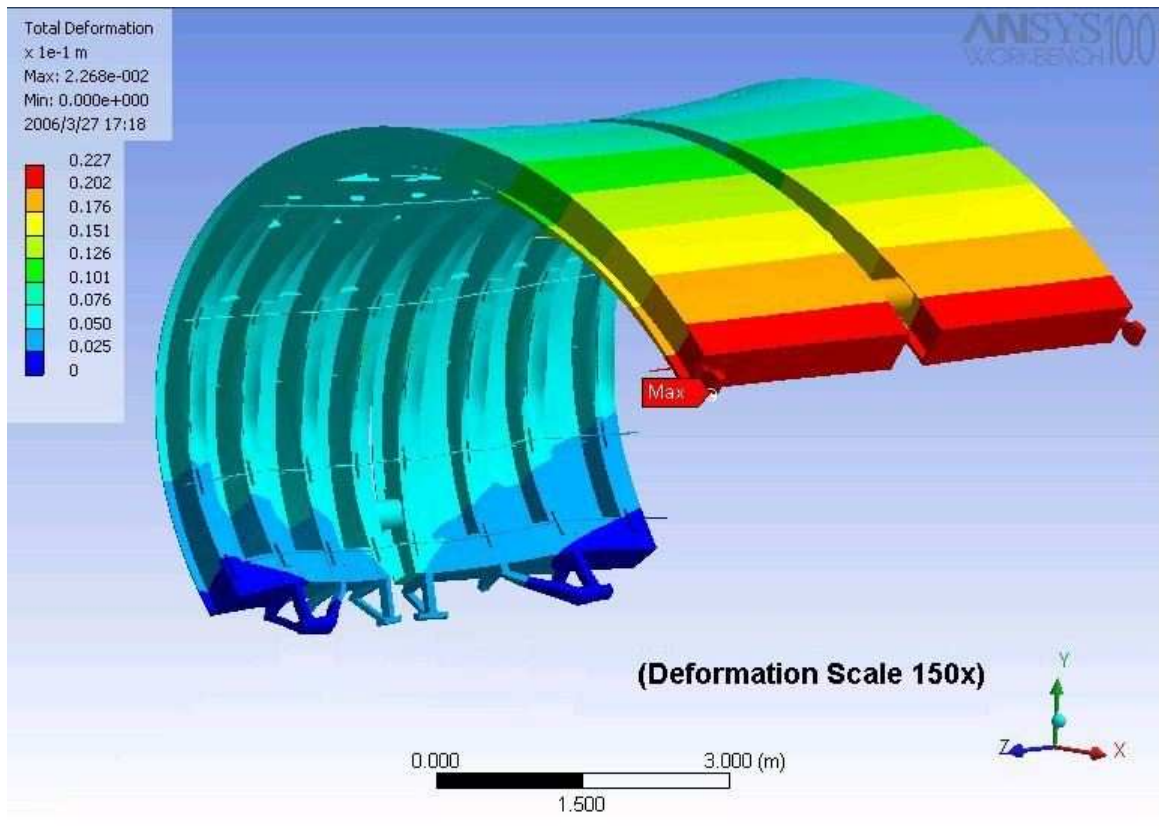


**Figure 8.4:** FEA deflections of the CalFrame under a total detector load of 110 metric tons.

The FEA results further show that the maximum stress in the upper support I-beam is modest while in the lower support I-beam is significant compared to the allowable stress for the 304LN material. In order to accommodate this high deflection and stress, several design features will be employed:

1. Providing means for adjusting the position of the CaFrame after we complete the installation of each super module. This option requires access to the CalFrame-support beams connection points.
2. Limiting the total weight of the EMCaI plus CalFrame as the final design proceeds to a level compatible with an acceptable maximum stress in the lower I-beam. The I-beam is constructed of austenitic stainless steel plates which have a guaranteed allowable yield strength equal to 270 MPa according to the Euro Norm EN10088-2 (Stainless steels -Part 2 : Technical delivery conditions for sheet/plate and strip for general purposes). Using the safety coefficients for material properties and load conditions as defined in the norm ENV 1993-1-1 (Eurocode 3: Design of steel structures) the admissible stress level for the plates is equal to the yield strength divided by 1.485. This gives 182 MPa. A further reduction has to be considered for the welds in the I-beam. The reduction factor for welds, under various different standards, can vary from 0.6 to 1 according to: the risk of the application; to the value of the items supported; and to the level of control and qualification of the welders. For this project, given the nature and level of inspection of the welds, we considered a value equal to 0.8 reasonable. Therefore the overall admissible stress is taken to be  $182 \times 0.8 = 146$  MPa. In the present FEA calculations, this stress corresponds to a total weight for the detector plus CalFrame of 110 metric tons.

At the present design stage of the CalFrame this figure implies a total maximum weight for the

EMCal of 86 metric tons. This weight limit is compatible with the detector described in Section 2 with a total active thickness of 20 radiation lengths.

3. Explore moving the CalFrame - I-beams interface points closer to the I-beams anchor locations and away from the center of the I-beams to reduce overall deflection and stress.

## 8.4 CalFrame Integration and Installation

The CalFrame is scheduled to be installed inside ALICE within a two week period in August 2006 after the TPC space frame is installed. Before the CalFrame is lowered in the ALICE cavern for installation a number of assembly and test activities are planned to take place in the surface halls at Point 2.

### 8.4.1 CalFrame Assembly

Due to road and transport limitation, between the CalFrame fabrication site in northern Italy and CERN, the CalFrame will be shipped in two half sections corresponding to the positive and negative pseudorapidity segments of the complete CalFrame. These two half sections of the CalFrame will be assembled, aligned and inspected on the surface at point 2.

### 8.4.2 Super Module Rails

Super modules, at installation time, slide onto a set of rails mounted to the under surface of the CalFrame. A set of rollers mounted to sides of the super module crates are used for this purpose. The rails themselves will be installed and aligned on the surface before the Cal Frame is lowered. Fig. 8.5 illustrates the rail mounting on the undersurface of the CalFrame. A total of four super module crates are shown in the installed position each with six strip modules in position. The remainder of the strip modules have been omitted for clarity. Four sets of rollers attached to each side of the super module crates are visible. In the fully installed position, the locations of the rollers correspond to the locations of the major ribs on the CalFrame.

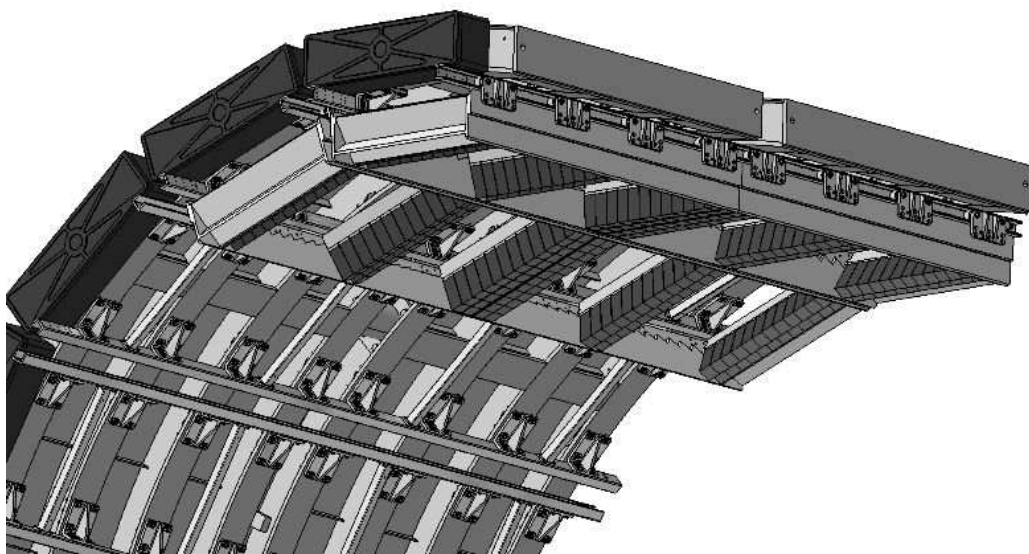


**Figure 8.5:** Under surface of the CalFrame illustrating the locations of the super module rail system and its interface to the rollers on the super module crates.

### 8.4.3 Super Module Installation Test

A super module installation test will be performed using a prototype super module crate loaded with dummy weight to the correct super module weight and utilizing the actual installation tooling designed for installation in the ALICE cavern at Point 2. This test will be undertaken to verify the functionality of the installation fixtures and to establish procedures to optimize the subsequent super module installation time in IP2.

### 8.4.4 CalFrame Load Test

A load test of the CalFrame will be performed to confirm the deflection results of the FEA model. These measurements will be performed on the surface using both static weights and hydraulic tools. Deflections at selected points will be measured and compared with the corresponding FEA analysis.

## 8.5 CalFrame Installation into ALICE

The CalFrame, after assembly and testing on the surface, will be lowered into the Point 2 cavern through the existing shaft. The CalFrame will be moved by the overhead crane and positioned in front of the ALICE magnet on an A-frame as shown in Fig. 8.6. The A-frame provides extension beams that are connected to the existing upper and lower support I-beams. The lower end of the CalFrame moves on bronze slider blocks which slide along the top of the lower I-beam as the CalFrame is installed by pulling into the ALICE magnet. The upper end of the CalFrame slides along the upper support extension rail and upper I-beam on wheels with the axles of the wheels oriented vertically. As discussed above and illustrated in Fig. 8.3 the wheel axles are oriented horizontally after installation to allow the CalFrame to slide on the top support beam in response to deflections as it is loaded.

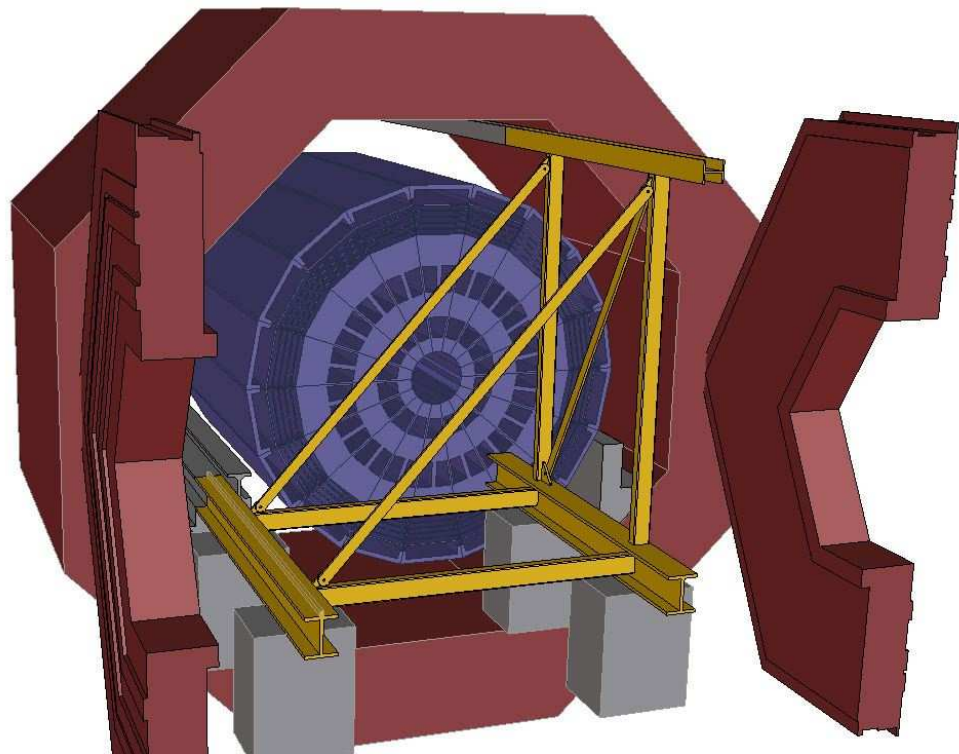


**Figure 8.6:** The CalFrame installation A-Frame which provides extensions of the upper and lower I-beam supports out away from the ALICE magnet where the CalFrame can be positioned with the overhead crane.

## 8.6 CalFrame and Super Module Alignment

The combined deflections of the upper and lower I-beams and the CalFrame itself vary substantially as a function of loading. Since the full complement of super modules may be installed in the CalFrame over a series of installation opportunities that may span up to three years and the corresponding number of LHC runs, a method of adjustment of the CalFrame is required to adjust the super modules to a best fit to their ideal radial and angular positions. In this way, the subset of installed super modules can be optimally positioned prior to each run.

At the upper end of the CalFrame, the alignment system consists of the cam-mounted wheels described in connection with Fig. 8.3. The wheels are mounted on pivoted levers which are adjusted by large screws. The lower end of the CalFrame is connected to the bronze slider blocks with adjustable-length struts. In each of the two strut groups, two are used to adjust in/out and up/down motion of the lower end of the CalFrame while a third strut provides longitudinal (parallel to the axis of the detector) stabilization.

## 8.7 Services, Access, and Maintenance

### 8.7.1 Services

In Routine operation, the EMCal requires services consisting of LV DC power, HV (400V) DC power and cooling water. At the present time, the integration plan for these services is nearing completion.

Cooling water is routed from the chiller to the two ends of the CalFrame where it branches to a manifold that runs along the end surfaces of the CalFrame. Leakless outlets along the length of this manifold provide cooling water to the electronics crates located at the end of each super module. The electronics crates are the only locations where cooling water is used on the EMCal. In particular, no water is brought out onto the back surfaces of the super modules. The cooling water flow is sized to remove all power dissipation in the electronics crates.

LVDC power is routed from allocated rack space to both ends of the ALICE magnet and from there to locations adjacent to the two ends of the CalFrame. At that point the transmission cables terminate in LV patch panels. From there, cables are run along the end surfaces of the CalFrame to power blocks mounted adjacent to the electronics crates.

HVDC is controlled and regulated on the front end digitizer boards located in the electronics crates. A single feed of 400 VDC to each electronics crate is all that is required.

### 8.7.2 Access and Maintenance

Access to the EMCal is limited but sufficient for safe and reliable operation of the detector. Electronics crates, located at the ends of the super modules are accessible for service even during relatively short access to the ALICE cavern. Front end electronics cards are easily removed for service. During short access, the ALICE doors will remain closed, and the ALICE volume will be a confined space (cf Safety Code A4). Generally any access to the EMCal will require the use of a safety harness and the relevant safety training.

The back surfaces of the super modules, however, which contain the APDs, charge sensitive preamps, and calibration LED drivers are not accessible once a super module is installed. Maintenance of components on the back surfaces of the super modules can only be performed during shut downs when sufficient time is available to withdraw a super module using its installation tool. Fortunately, all the components that are mounted on the rear surfaces of the super modules are robust and unlikely to need any significant service.

## 8.8 Safety Considerations.

The EMCal project team is fully committed to the safe construction, installation and operation of the EMCal as a component of the ALICE suite of detectors. Our primary goal is to ensure the safety of all personnel involved in the project but also to control risks, to the greatest extent possible, that might result in damage to the EMCal, other ALICE detector systems or the environment.

The EMCal itself poses no safety hazards beyond those typical of other ALICE detector systems. Indeed, it presents far fewer hazards than most typical detector systems. No gasses of any kind are required for EMCal operation and both HV and LVDC requirements are modest.

Temperatures on the critical components of the front end electronics the only location of any significant power dissipation are continuously monitored. In addition, located as they are within the ALICE magnet volume, the EMCal electronics crates are covered by ALICEs common smoke detection system (SNIFFER).

No flammable materials are used in the EMCal construction with the exception of polystyrene plastic scintillator. This material is, however enclosed in stainless steel containers within the detector in a manner that removes it from any source of oxygen for combustion.

## 9 Planning and Organisation

---

### 9.1 Schedule

The schedule for the construction and the installation of the EMCal is driven by the start of LHC and by the physics which will be addressed in the first years of LHC operation. The main critical path step in the near term will be delivery to point 2 and the installation of the EMCal support structure inside the ALICE magnet in August 2006. This structure has been already been fully funded and the design and construction is proceeding on schedule. I-beam support rails to anchor this structure have already been installed inside the ALICE magnet since 2004.

An extensive detector and electronics R&D program conducted during 2005 and 2006 described in this document has already fixed the main detector parameters and an integrated system test including final electronics has been conducted with hadron, muon and electron beams. A final, production ready design will be completed by the end of 2006.

The Technical Design Report for the EMCal should be finished by this time at the end of 2006 or at beginning of 2007 when money for the construction should be available assuming the final approval from USDoE, INFN, and INFN is granted. Given approval on this timescale, the first super module could be completed and installed in November 2007 to have it within ALICE during the first run in 2008. This will allow not only the first physics results for  $\gamma$ ,  $\pi^0$  and electron/positron pair production at high  $p_t$  but also the commissioning of the hardware and the online and offline reconstruction software. Following on this, physics opportunities suggest that about half of the full EMCal should be completed and installed in November 2008 to have a good acceptance to start the study of jet physics in the 2009 run. Finally, the complete EMCal should be ready for the 2010 run. This construction and installation schedule is technically feasible within the present EMCal Collaboration but it depends critically on the funding profile to the project which, of course, is not yet defined.

### 9.2 Cost Estimate

The cost estimate for the full EMCal project scope (11 super modules) is summarized in Table 9.1. The cost estimate is based on preliminary quotations obtained whenever possible from industrial vendors or from component production estimates in laboratories within the Collaboration. A large fraction of the cost will be in the electronics whose cost evaluation is mainly based on the cost of the PHOS electronics, and includes spares and contingency. Only items which are exclusive to the EMCal are included in the table while items common to all ALICE sub-detector (DAQ, offline, etc.) are not included. Labour costs are not included. The cost of the support structure and the R&D money already allocated by DoE (about 2 MCHF) is also not included.

### 9.3 Responsibilities

The EMCal is a common project shared and jointly managed by several US and EU institutes. A preliminary breakdown by institution of the responsibilities for the different subsystems of the ALICE EMCal is shown in Table `reftable:responsibilities` below. The responsibilities will include all technical and financial aspects of the project, from R&D and design, to construction, assembly and operation of the equipment. Final responsibilities will be defined after the complete funding and approval of the project.

**Table 9.1:** Project CORE cost estimate for the EMCal detector itself, electronics, conventional systems, infrastructure and installation, and calibration and test facilities.

| Detector system                     | Cost (kCHF) |
|-------------------------------------|-------------|
| Mechanics                           | 975         |
| Working Tools                       | 164         |
| Detector                            | 3750        |
| Electronics ( $\sim 13$ K channels) | 3207        |
| Conventional Systems                | 85          |
| Infrastructure and Installation     | 45          |
| Cosmic and Beam Test Facility       | 325         |
| Total Detector Cost                 | 8551        |

**Table 9.2:** Primary institutional responsibilities within the EMCal project.

|                                    |   |
|------------------------------------|---|
| Technical Coordination             | LBNL  |
| Mechanics                          | Catania, Grenoble, LBNL, MSU, Nantes, UCLA, Wayne State                     |
| Detector Construction and Assembly | Catania, Frascati, Grenoble, Houston, Nantes, Protvino, UCLA, Wayne State   |
| Electronics                        | ORNL, OSU, Purdue, UCLA, UT   |
| Trigger                            | Grenoble, LBNL, ORNL, UT  |
| Offline                            | UCD, Catania, Frascati, Kent State, LLNL, LBNL, Nantes, OSU, Strasbourg, UW |
| Online                             | Creighton, ORNL, Strasbourg, UT   |
| Infrastructure and Integration     | CERN, LBNL, Nantes  |



# References

---

## Chapter 1

- [1] F. Carminati *et al.* (ALICE Collaboration), *J. Phys.* **G30**, 1517 (2004).
- [2] ALICE Collaboration, *Physics Performance Report, Vol 2*, *J. Phys.* **G** (2006).
- [3] R. Baier, D. Schiff and B. Zakharov, *Ann. Rev. Nucl. Part. Sci.* **50**, 37 (2000).
- [4] M. Gyulassy, I. Vitev, X. N. Wang and B. W. Zhang, *Quark Gluon Plasma 3*, 123 (ed. R. Hwa and X. N. Wang, World Scientific, Singapore); nucl-th/0302077.
- [5] A. Kovner and U. Wiedemann, *Quark Gluon Plasma 3*, 192 (ed. R. Hwa and X. N. Wang, World Scientific, Singapore); hep-ph/0304151.
- [6] P. Jacobs and X. N. Wang, *Prog. Part. Nucl. Phys.* **54**, 443 (2005).
- [7] I. Arsene *et al.* (BRAHMS), *Nucl. Phys.* **A757**, 1 (2005).
- [8] K. Adcox *et al.* (PHENIX), *Nucl. Phys.* **A757**, 184 (2005).
- [9] B. B. Back *et al.* (PHOBOS), *Nucl. Phys.* **A757**, 28 (2005).
- [10] J. Adams *et al.* (STAR), *Nucl. Phys.* **A757**, 102 (2005).
- [11] J. D. Bjorken, FERMILAB-PUB-82-059-THY.
- [12] M. G. Mustafa, *Phys. Rev.* **C72**, 014905 (2005).
- [13] S. Wicks, W. Horowitz, M. Djordjevic and M. Gyulassy, nucl-th/0512076.
- [14] S. S. Adler *et al.* (PHENIX), *Phys. Rev. Lett.* **91**, 232301 (2005).
- [15] I. Arsene *et al.* (BRAHMS), *Phys. Rev. Lett.* **91**, 072305 (2003).
- [16] S. S. Adler *et al.* (PHENIX), *Phys. Rev. Lett.* **91**, 072303 (2003).
- [17] B. B. Back *et al.* (PHOBOS), *Phys. Rev. Lett.* **91**, 072302 (2003).
- [18] J. Adams *et al.* (STAR), *Phys. Rev. Lett.* **91**, 072304 (2003).
- [19] I. Vitev and M. Gyulassy, *Phys. Rev. Lett.* **89**, 252301 (2002).
- [20] S. S. Adler *et al.* (PHENIX), *Phys. Rev.* **C69**, 034909 (2004).
- [21] J. Adams *et al.* (STAR), nucl-ex/0601042.
- [22] R. J. Fries *et al.*, *Phys. Rev.* **C68**, 044902 (2003).
- [23] V. Greco, C. M. Ko and P. Levai, *Phys. Rev.* **C68**, 034904 (2003).
- [24] R. C. Hwa and C. B. Yang, *Phys. Rev.* **C67**, 034902 (2003).
- [25] D.d'Enterria, *Eur. Phys. J* **C43** (2005) 295.
- [26] C. Loizides, hep-ph/0507018.
- [27] C.A. Salgado and U. Wiedemann, *Phys. Rev.* **D68**, 014008 (2003).
- [28] K. Eskola *et al.*, *Nucl. Phys.* **A747**, 511 (2005).
- [29] A. Drees, H. Feng and J. Jia, *Phys. Rev.* **C71**, 034909.
- [30] A. Dainese, C. Loizides and G. Paic, *Eur. Phys. J.* **C38**, 461 (2005).
- [31] J. Adams *et al.* (STAR), *Phys. Rev. Lett.* **95** (2005) 152301.
- [32] N. Borghini and U. Wiedemann, hep-ph/0506218.
- [33] C.A. Salgado and U. Wiedemann, *Phys. Rev. Lett.* **93** (2004) 042301.
- [34] X.-N. Wang and Z. Huang, *Phys. Rev.* **C55**, 3047 (1997).
- [35] D. Buskulic *et al.* (ALEPH), *Nucl. Instr. Meth.* **A360**, 481 (1995).
- [36] M. Miller *et al.* (STAR), proceedings of PANIC05, hep-ex/0604001.

## Chapter 2

- [1] ALICE Collaboration, *A Large Ion Collider Experiment*, CERN/LHCC 95-71, 15 December 1995.
- [2] L. Aphecetche *et al.*, (PHENIX), *Nucl. Instrum. Methods* **A499** (2003) 521.

- [3] LHCb Collaboration, *LHCb TDR2*, CERN/LHCC 2000-36, 6 September 2000.
- [4] M. Beddo et al, *The STAR barrel electromagnetic calorimeter*, Nucl. Instrum. Methods **A499** (2003) 725.

## Chapter 3

- [1] Photon Spectrometer PHOS, ALICE Technical Design Report, CERN /LHCC 99-4, 5 1999.
- [2] D.V.Aleksandrov *et. al.*, *A high resolution electromagnetic calorimeter based on lead-tungstate crystals*, Nucl. Instrum. Methods **A550** (2005) 169.
- [3] H. Muller *et. al.*, *Configurable Electronics with Low Noise and 14-bit Dynamic Range for Photodiode-based Photon Detectors*, Submitted to Nucl. Instrum. Methods **A**, (2006).
- [4] K. Deiters *et. al.*, *Properties of the Avalanche Photodiodes for the CMS Electromagnetic Calorimeter.*, Nucl. Instrum. Methods **A453**, (2000) 223.
- [5] K. Deiters *et. al.*, *Investigation of the Avalanche Photodiodes for the CMS Electromagnetic Calorimeter Operated at High Gain*, Nucl. Instrum. Methods **A461**, (2001) 574.
- [6] J. Grahl *et. al.*, *Radiation Hard Avalanche Photodiodes for CMS ECAL.*, Nucl. Instrum. Methods **A504**, (2003) 44.
- [7] I.Sibiriak, A.Tsvetkov, and A.Vinogradov, *APD power control for the ALICE PHOS prototype*, Alice Internal Note, ALICE-INT-2005-013.
- [8] *The ALTRO chip: A 16-channel A/D converter and digital processor for gas detectors*, Proc. IEEE NSS/MIC, November 2002, Norfolk.
- [9] Lien, J.A., *The Readout Control Unit of the ALICE TPC*, Thesis, CERN-THESIS-2005-013.
- [10] *Trigger Region Unit for ALICE PHOS Calorimeter*, Proceedings LECC05, 11th Workshop on Electronics for LHC and future Experiments, Heidelberg, September 2005.
- [11] ALICE DAQ, ALICE DDL Interface Control Document, Internal Note ALICE-INT-1996-43 V9.1.
- [12] Heather Gray, *The Reconstruction of High- $p_T$  Photons with the Electromagnetic Calorimeter of the ALICE Experiment at the LHC*, PhD Thesis, University of Capetown, May 2005.
- [13] R. Brun *et. al.*, *Computing in ALICE*, Nucl. Instr. Meth. **A502** (2003) 339-346. <http://aliweb.cern.ch/offline/>

## Chapter 4

- [1] The ALICE Trigger Project, ALICE Central Trigger Processor, User Requirement Document, Draft 1.0, 24 October 2001.
- [2] ALICE Collaboration, *Technical Design Report of Trigger, Data Acquisition, High-Level Trigger and Control System*, CERN/LHCC/2003-062.
- [3] The ALICE Trigger Project, ALICE Local Trigger Unit, Preliminary Design Review Document, Revision 0.1, 1 September 2002.
- [4] B. G. Taylor, LHC machine timing distribution for the experiments, in *Proc. of the 6th Workshop on Electronics for LHC Experiments*, Cracow, Poland, 2000 (CERN 2000-010, Geneva, 2003).
- [5] J. Baud *et. al.*, CASTOR status and evolution, in *Proc. Conf. on Computing in High-Energy Physics*, La Jolla, CA, USA, March 2003 (SLAC, Stanford).
- [6] ALICE DAQ, DATE V4 User's Guide, Internal Note ALICE-2002-036.
- [7] P.G.Innocenti *et. al.*, Report of the ALICE HLT and HLT-DAQ Interface Review Panel, Internal Note ALICE-EN-2003-009 v.1.

## Chapter 5

- [1] B.K. Lubsandozhiev and Y.E. Vyatchin, *Stability Studies of Nanosecond Light Sources Based on Blue Ultra Bright LEDs*, physics/0403018.
- [2] H. Muller *et al.*, *Configurable Electronics with Low Noise and 14-bit Dynamic Range for Photodiode-based Photon Detectors*, Submitted to Nucl. Instrum. Methods **A**, (2006).
- [3] ALICE Collaboration, *Technical Design Report of Trigger, Data Acquisition, High-Level Trigger and Control System*, CERN/LHCC/2003–062.
- [4] S.S. Adler *et al.*, (PHENIX Coll.), Phys. Rev. Lett. **91** (2003) 241803.

## Chapter 6

- [1] H. Muller *et al.*, *Configurable Electronics with Low Noise and 14-bit Dynamic Range for Photodiode-based Photon Detectors*, Submitted to Nucl. Instrum. Methods **A**, (2006).
- [2] ALICE Collaboration, *Meson Test beam experiment T951: ALICE EMCAL Prototype Test*, <http://www-ppd.fnal.gov/MTBF-w/mtbf-mou.htm>.
- [3] ALICE DAQ, DATE V4 User's Guide, Internal Note ALICE-2002-036.
- [4] L. Aphecetche *et al.*, (PHENIX), Nucl. Instrum. Methods **A499** (2003) 521.

## Chapter 7

- [1] A. Dainese *et al.*, Eur. Phys. J. **C38**, 461 (2005).
- [2] C. A. Salgado and U. A. Wiedemann, Phys. Rev. **D68**, 014008 (2003).
- [3] A. Morsch, private communication.
- [4] I. P. Lokhtin and A. M. Snigirev, Eur. Phys. J. **C16**, 527 (2000).
- [5] ALICE Forward Detector TDR; CERN/LHCC 2004-025.
- [6] S. Blyth *et al.*, J. Phys. **G30**, S1155 (2004).
- [7] S. Blyth, nucl-ex/0510065.
- [8] J. Adams *et al.* (STAR), Phys. Rev. **C70**, 054907 (2004).
- [9] M. Miller *et al.* (STAR), hep-ex/0604001.
- [10] D. Buskulic *et al.* (ALEPH), Nucl. Instr. Meth. **A360**, 481 (1995).
- [11] G. Arnison *et al.*, Phys. Lett. **B132**, 214 (1983).
- [12] K. Eskola *et al.*, Phys. Rev. **C72**, 044904 (2005).
- [13] D. Acosta *et al.*, Phys. Rev. **D72**, 051104 (2005).
- [14] F. Arleo *et al.*, JHEP **0411**, 009 (2004).
- [15] ALICE Collaboration, *Physics Performance Report, Vol 2*, J. Phys. **G** (2006).
- [16] T.C. Awes *et al.*, Nucl. Instrum. Methods **A311**, (1992).
- [17] Y.L. Dokshitzer and D.E. Kharzeev, Phys. Rev. Lett. **B519**, 199 (2001).
- [18] N. Armesto *et al.*, Phys. Rev. **D71**, 054027 (2005).
- [19] ALICE Physics Performance Report Vol II, Chapt. 6.6.
- [20] J. Adams *et al.* (STAR Collaboration), Phys. Rev. Lett. **94**, 062301 (2005).

